Ver : 1.11

AstroSat

INDIA'S FIRST MULTIWAVELENGTH ASTRONOMY SATELLITE

A simultaneous view of the Universe in UV and X-rays

AstroSat HANDBOOK

Space Science Programme Office (SSPO)
INDIAN SPACE RESEARCH ORGANISATION (ISRO), HQ

Version summary

Ver 0.1 - Collation of all individual payload inputs into separate chapters -	Jan 11 2013
Ver 0.2 - Updated with comments from individual payload teams	July 31 2013
Ver 0.3 - Updated with comments from UVIT payload team	Aug 24 2013
Ver 0.4 -Updated with comments from LAXPC payload team	Oct 01 2013
Ver 1.0 - Revisions from SXT and inclusion of outline of Ch10 & 11	Oct 18 2013
Ver 1.1 - Revision from LAXPC payload team	Oct 23 2013
Ver 1.2 – Corrected table 1 and replaced ASTROSAT figure	Nov 03 2013
Ver 1.3 – Revision of LAXPC chapter	Jul 25 2014
Ver 1.3a – minor corrections in text and tables	Nov 10 2014
Ver 1.6 – The current version is numbered as Ver 1.6 so as to avoid confusion since Ver 1.5 was circulated sometime back. Changes are in the payload characteristics table in Introduction, minor corrections and addendum on brightness limits in UVIT, hardware section in CZT and last paragraph of CPM. LAXPC remains the same as version 1.3. SSM is yet to be updated.	Dec 18 2014
Ver 1.7 - Updated after the completion of ground calibration of payloads. LAXPC chapter remains the same as previous version. APPS guidelines included.	Jun 08, 2015
Ver 1.8 – Updated after on-orbit calibrations and performance verification	June 14, 2016
Ver 1.9 - Updated UVIT and LAXPC chapters	November 10, 2016
Ver 1.10 - Updated UVIT, SXT, LAXPC, SSM chapters	May 03, 2017
Ver 1.11 – Updated all the payload chapters	**Jan 08, 2018**

Contributors:

Dipankar Bhattacharya, IUCAA, Pune
Gulab C Dewangan, IUCAA, Pune
H.M. Antia, LAXPC team, TIFR, Mumbai
M.C. Ramadevi, Payload manager, SSM, ISAC, Bengaluru
A.R. Rao, Payload manager, CZTI, TIFR, Mumbai
S.N.Tandon, Programme manager, UVIT, IUCAA, Pune
Sudip Bhattacharya, Payload manager, SXT, TIFR, Mumbai
J.S. Yadav, Payload manager, LAXPC, TIFR, Mumbai

Compiled by:

Space Science Programme Office, ISRO HQ

CONTENTS

Chapter-1

Chapter-2

Chapter-3

Chapter-4

Chapter-5

Chapter-6

Chapter-7

Chapter-8

Chapter 1

AstroSat mission

AstroSat – India's first dedicated astronomy satellite

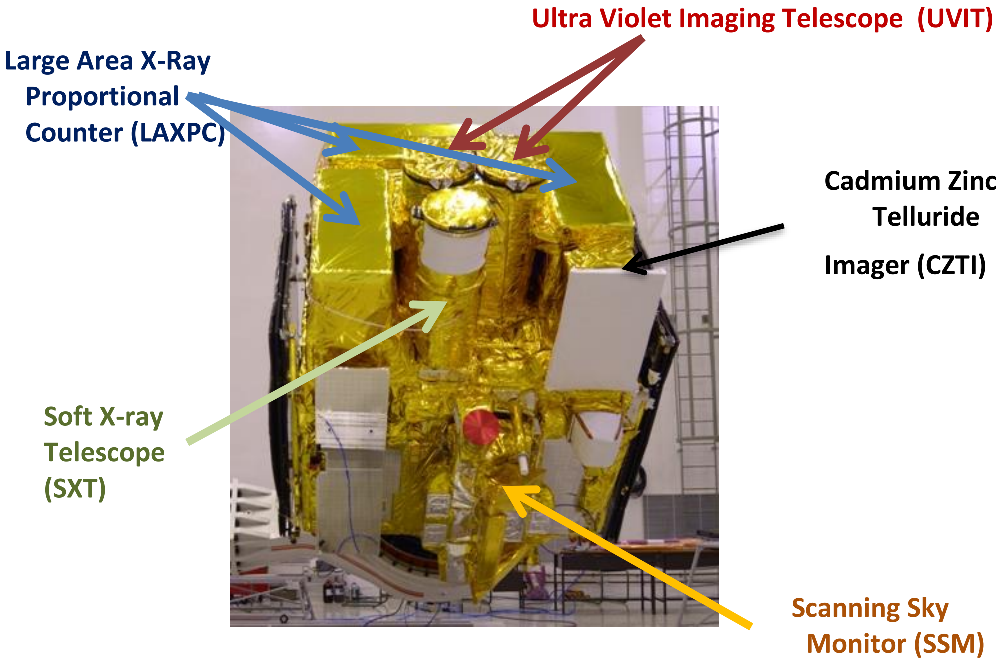

AstroSat spacecraft – actual view

To understand the nature of cosmic sources, their radiation processes and environment, it is necessary to measure their emission over the entire electromagnetic spectrum. Since intensity of most cosmic sources varies with time, the variability being wavelength-dependent, it is necessary to make simultaneous observations in different wavebands. Most of the current space astronomy observatories are dedicated to a particular waveband e.g. X-ray, UV etc and therefore, usually multi-wavelength studies have to be made from coordinated observations with different satellites. There are logistical problems in making simultaneous and coordinated studies of a specific object from different satellites and ground-based telescopes. As a result, despite a large number of such multiwavelength observation campaigns, very few sources have so far been studied over wide spectral band leading to poor understanding of the underlying physical processes. The most efficient and effective approach is to have a dedicated satellite such as AstroSat with several co-aligned instruments covering the desired spectral bands so that simultaneous observations in all the desired wavebands is possible.

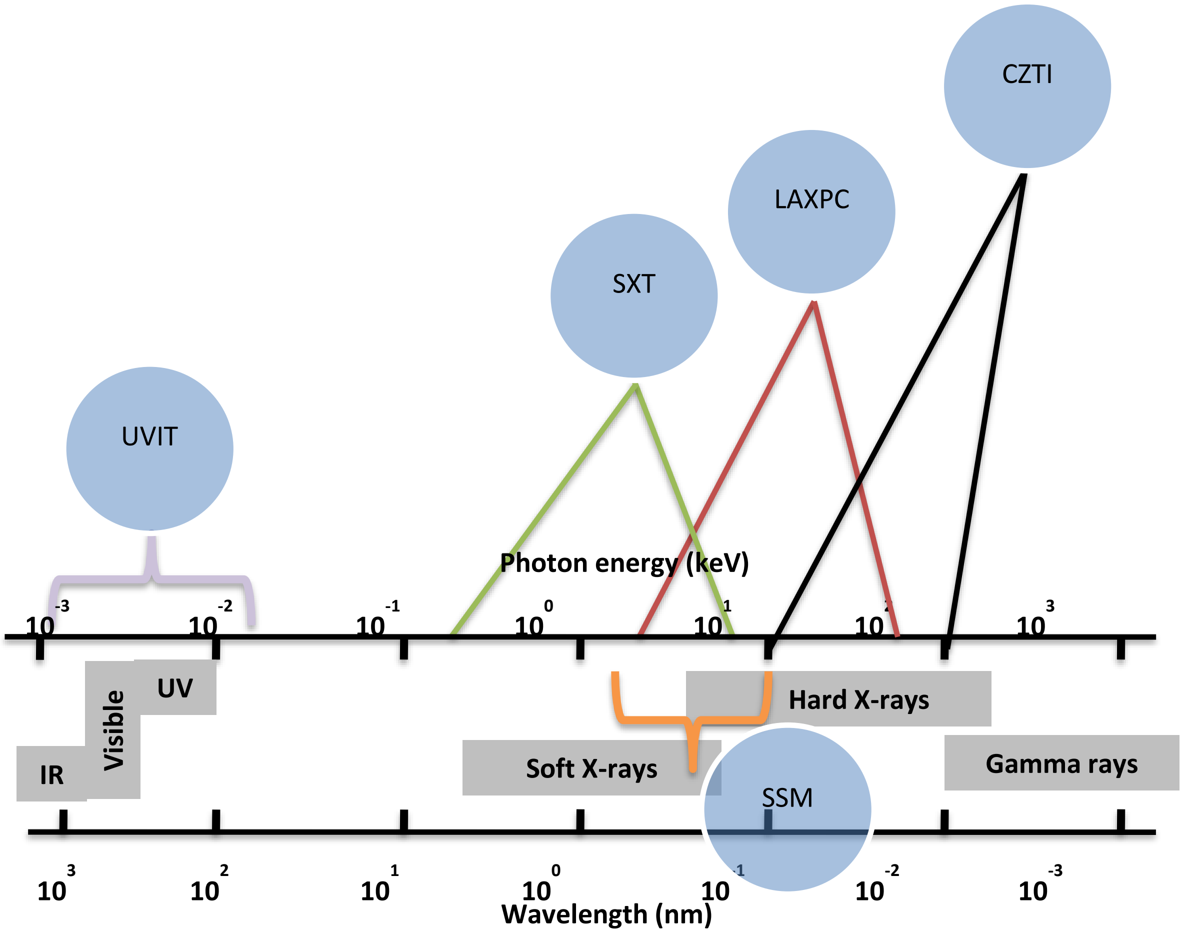

Typical Electromagnetic Spectrum

Wavelength coverage of AstroSat payloads

AstroSat spacecraft and five astronomy payloads covering optical, UV and X-rays were designed, developed, realized and launched on 28th September 2015 by PSLV-C30 (XL) from Sriharikota. The spacecraft was put in 650km near-equatorial orbit with inclination of 6 degree. The payloads were switched ON in a sequence and are operationalised.

PSLV C-30 lift off from Sriharikota

The performance verification phase began in October 2015 and ended on 31 March 2016. Assessment of instrument performance, completion of initial calibration, announcing the payload capabilities and release of first set of calibration files were the aims of this phase.

First light observations were obtained with the Charged Particle Monitor (CPM) on October 1, the Cadmium-Zinc Telluride Imager (CZTI) on October 6, Scanning Sky Monitor (SSM) on October 12, three Large Area X-ray Proportional Counters (LAXPCs) on October 19, Soft X-ray Telescope (SXT) on October 26, and the visible and UV telescopes on December 1, 2015.

Science observations by the payload teams were carried out from April to September 2016.

AstroSat is being operated as an observatory, in which observatory time is allotted based on proposals received from interested researchers and scientists through ISRO's Announcement of Opportunity (AO). From October 2016 to September 2017, Indian AO proposals were executed. From October 2017 onwards, the observatory is open to Indian as well as International proposers.

Primary Science Objectives of AstroSat

Understand high energy processes in binary systems
Search for black hole sources in the Galaxy
Measure magnetic fields of neutron stars
Study high energy processes in extragalactic systems
Detect new transient X-ray sources
Limited high-angular resolution deep field survey in UV

These primary science objectives are being met with 5 science payloads.

Large Area X-ray Proportional Counters (LAXPC)
Cadmium-Zinc-Telluride Imager (CZTI)
Soft X-ray Telescope (SXT)
Scanning Sky Monitor (SSM)
Ultra Violet Imaging Telescope (UVIT)

The important parameters of the instruments are listed in the AstroSat payload characteristics table (end of this chapter).

A complementary Charged Particle Monitor (CPM) is also onboard to provide data on particle flux. The high voltage will be lowered or put off using data from CPM when the satellite enters the South Atlantic Anomaly (SAA) region to prevent damage to the detectors as well as to minimize ageing effect in the Proportional Counters.

AstroSat Payloads

- Three identical Large Area X-ray Proportional Counters (LAXPC) covering 3-100 keV region for variability studies of X-ray Binaries and other cosmic sources. It has four to five times more effective area above 30 keV compared to the Proportional Counter Array (PCA) on the Rossi X-ray timing Explorer (RXTE). (Primary goal – fast time variability and wide band spectral coverage)

- Cadmium-Zinc-Telluride Imager (CZTI) array with coded mask aperture extends the high energy limit (25-150 keV band) for spectral studies. (extend high energy range, good spectral energy if no source confusion; solid state detectors)

- Soft X-ray Telescope (SXT) using X-ray reflecting mirrors and X-ray CCD for timing and variability studies in 0.3 – 8.0 keV band (Soft X-ray energies; imaging in X-rays)

- Scanning Sky Monitor (SSM) for detection and monitoring of new and known X-ray sources in 2.5 – 10 keV region.

- Ultra Violet Imaging Telescope (UVIT) to image the sky simultaneously in three wavelengths, one covering the FUV band (130 – 180 nm) and the second sensitive in NUV (200 – 300nm) and Visible (320 – 550 nm) bands. (NUV, FUV and Optical imaging; intensity variation).

UVIT payload has collaboration with Canadian Space Agency (CSA) and SXT is in collaboration with University of Leicester, UK.

Uniqueness of AstroSat

- ✓ Simultaneous multi-wavelength observations using single satellite.
- ✓ Broad band coverage using Optical, UV, low and high energy X-ray payloads.
- ✓ It is expected that the effective area of LAXPC is ≥ four to five times that of Rossi X-ray timing Explorer (RXTE) above 30 keV.
- ✓ Image resolution of UVIT ~ 1.5” the best so far in NUV compared to ~ 6” of GALEX.

AstroSat - Payload Characteristics

PARAMETER	**UVIT**	**SXT**	**LAXPC**	**CZTI**	**SSM**
Detector	Photon-counting (Intensified) CMOS imagers	X-Ray CCD at the focal plane	Proportional counter	CdZnTe Detector Array	Position sensitive Proportional Counter
Optics	Twin Ritchie Chretian 2 mirror system	Conical foil (Wolter-I) Mirrors	Collimator	2-D coded Mask	1-D coded Mask
Bandwidth	130-180 nm 200-300 nm & 320-550 nm	0.3 - 8 keV	3 - 100 keV	25 - 150 keV (overall)	2.5 - 10 keV
Geometric Area (cm^2)	1250	250	10800*	976	57.6 per SSM
Effective Area (cm^2)	~ 10 @150 nm, ~ 40 in 200-300 & 320-550 nm	90@1.5 keV	6000@5-20 keV*	415 (photometric) 335 (spectroscopic)	~5.9 @ 2.5 keV ~27.24 @ 5keV (SSM1+SSM3)
Field of View	~ 28' dia	~40' (Dia)	0.9^0 x 0.9^0	4.6^0 x 4.6^0 (25 – 150 keV) Open detector at ~ 150 keV with eff. area 100 cm^2	SSM1 26.8 x 100 deg; SSM3 - 22.1 x 100 deg, FWZM
Energy Resolution	<100- 500 A (depends on choice of filters)	90 eV @1.5 keV; 136 eV @5.9 keV	12 - 15% in 22-60 keV	6% at 100 keV	25% @ 6keV
Angular Resolution	1.2 to 1.5 arc sec in 130-180 nm and 200-300 nm	2 arc min FWHM; 10 arc min HPD	~(1-5) arc min (in scan mode only)	8 arc min	~10-13 arc min in coding direction and 2.5° across

PARAMETER	**UVIT**	**SXT**	**LAXPC**	**CZTI**	**SSM**
Time resolution	2 ms	~2.4 s (full frame), ~0.278 s (150x150 centered pixel frame)	10microsec	20microsec	0.1 ms
Typical observation time per target.	5 min to 100 min	0.5 - 1 day	0.25- 1 day	2 days	10 min per FOV
Sensitivity (Obs. Time) (Unit)	20 mag. (5σ) In 160 s for 130-180nm	~10^{-13} ergs cm^{-2} s^{-1} (5 σ) (20000 s)	1 milliCrab (3σ) (1000 s)	20 milliCrab (5σ) (10000s)	~40 milliCrab for SSM1 ~28 milliCrab for SSM3 (3σ, 600s)
Total Mass (kg)	230	70	419	56	65.5
Total Power (Watts)	87	53 (with HOP ON)	65	73.5	41(excl .motor + drive e-nics)
Total Memory per orbit (MBytes)	2850	280	700	50	200
Sun-avoidance angle	45 deg	45 deg	30 deg	NA	5 deg from edge of FOV
Moon-avoidance angle	15 deg	NA	NA	NA	NA
Bright Earth limb avoidance angle	12 deg Ram avoidance angle 12 deg	>12 deg	NA	NA	NA

* If LAXPC30 is not usable, the area will reduce to 2/3 of the stated value.

The changes compared to the previous version of the handbook is marked in blue. The technical details on the payloads are provided in the forthcoming chapters.

Chapter 2

Ultra-Violet Imaging Telescope

Imaging in the ultra-violet regime with a spatial resolution of 1.8" (~ X 3 better than Galex) in a field of ~ 28' provides many opportunities for Galactic and extra-galactic studies. Some of the objectives are listed below:

a) Time variations in UV of X-ray sources in coordination with the X-ray payloads
b) Star formation in nearby galaxies
c) Star formation in interacting galaxies
d) Star formation history of universe
e) Hot stars in Globular clusters
f) Planetary nebulae

Instrument Overview

UVIT is primarily an imaging instrument. Images are made simultaneously in three channels: FUV (130-180 nm), NUV (200-300 nm), and VIS (320-550 nm), in a field ~ 28' circle. The spatial resolution (FWHM) is < 1.8" for the FUV and NUV channels, and it is ~ 2.2" for the VIS channel. In each channel, a set of filters are available, in the filter-wheels, for selecting a band. In the two ultraviolet channels, gratings are provided for low resolution (~ 100) slitless spectroscopy. The focussing optics is configured as twin R-C telescopes, each with a primary mirror with with effective diameter of ~ 375 mm.

The overall structure is shown in Fig. 2.1. Those parts of the telescopes which define locations of the optical elements are mostly made of Invar36, and the other parts are made of Aluminium alloy. The two telescopes are mounted on a cone-like structure of Titanium, which is attached to central cylinder of the spacecraft.

A cylindrical baffle extends over each of the telescopes for attenuating the radiation from off-axis sources. With these baffles the light reaching the detector from sources at 45 deg. from the axis is attenuated by a factor 10^9; with such attenuation the light reaching the detector from full Moon at 45 deg from the axis is less than the average sky background. In addition to these baffles, the doors act as sun shades as long as Sun is at > 45 deg from the axis and the plane containing the optical axis and normal to the doors.

In order to avoid contamination of the optics due to ultraviolet assisted reactions, bright-earth is kept away from the axis by >12 deg., and the sun is kept behind the sun-shield at all times even if UVIT is not observing.

The geo-coronal lines are very strong in day time, and a significant amount of solar radiation could be scattered by the other instruments on the spacecraft into the baffles. Therefore, the nominal observation period is restricted to the night time (In special cases, observations in day time could be considered).

The intensified CMOS detectors can either be used in a high gain photon counting mode, or in a low gain integration mode (in which signal in a pixel of the CMOS detector could be contributed by multiple photons). Pointing accuracy of the spacecarft is ~ 3’, and for any pointing the aspect could drift by several tens of arcsec, at rates < 0.2”/s. In order to eliminate effect of this drift on the PSF, multiple short exposures (< 1 s each) are taken and are combined using shift and add. As the VIS field has adequate number of bright sources, images (taken in integration mode) from this channel are used to estimate the drift as a function of time.

There are three main contributors to the PSF: optics, detector, and drift of the aspect. Of these three the largest contribution is made by the detector and it is ~ 1” FWHM. The estimated overall FWHM, including the contributions of the optics and the drift, is 1.5”.

The peak effective area, excluding the losses in the filters, is: ~ 15 cm^2 for the FUV, and ~ 50 cm^2 for NUV & VIS. An exposure calculator is available to estimate the expected signal levels for point sources observed through the various filters. In addition, a simulator is available which can generate the output image expected from an observation with UVIT, for an extended source with known distribution of the intensity.

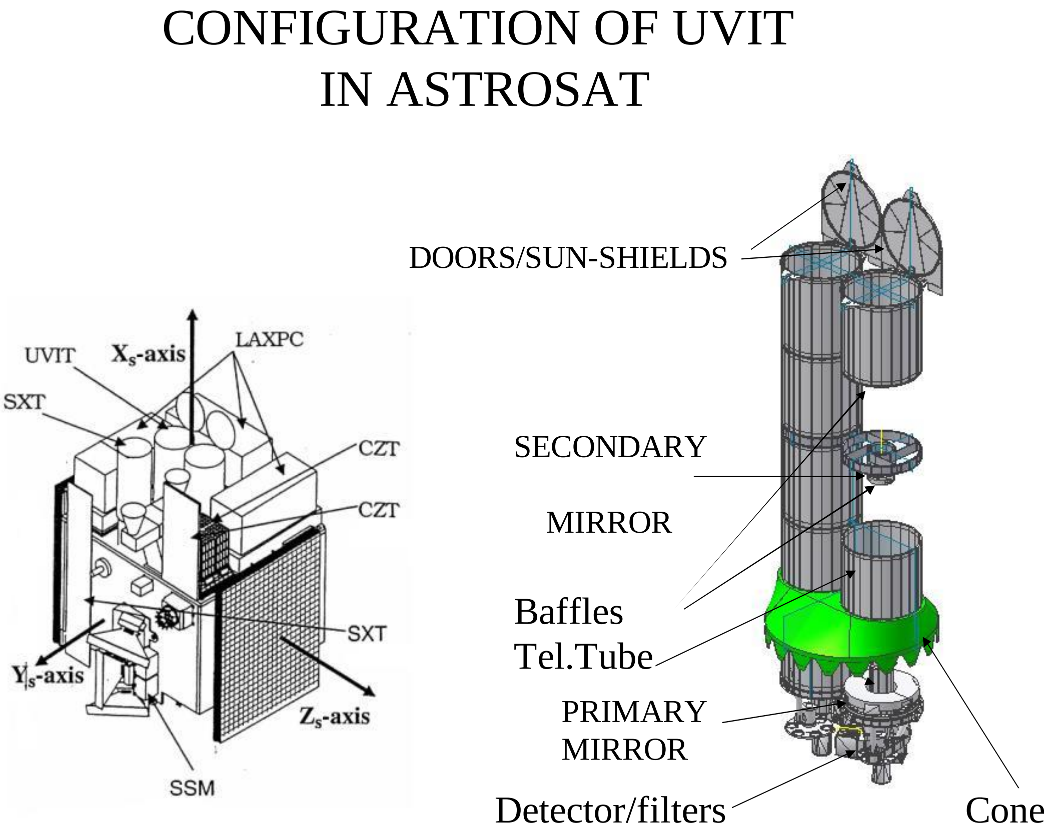

Fig. 2.1 Configuration of the instruments in ASTROSAT is shown on the left. UVIT is shown on the right. The two telescopes are mounted on “Cone” which is fixed on the S/C.

Optics

Optical layouts of the two telescopes are are shown in Fig. 2.2 & Fig. 2.3. Both telescopes have hyperbolic f/4.5 primary mirrors of diameter ~ 380 mm (optical diameter ~ 375 mm), and hyperbolic secondary mirrors of optical diameter 140 mm. The overall focal length of the telescopes is ~ 4750 mm. The reflective coatings are Al with MgF_2 layer. The expected reflectivity is: ~ 70% per surface in FUV, and > 80% per surface in NUV & VIS. Roughness of the coated surfaces is < 1.5 nm rms, to keep the scattering < 1% per surface.

OPTICAL LAYOUT -- FUV CHANNEL
f/12 Cassegrain, ~ 380 mm aperture

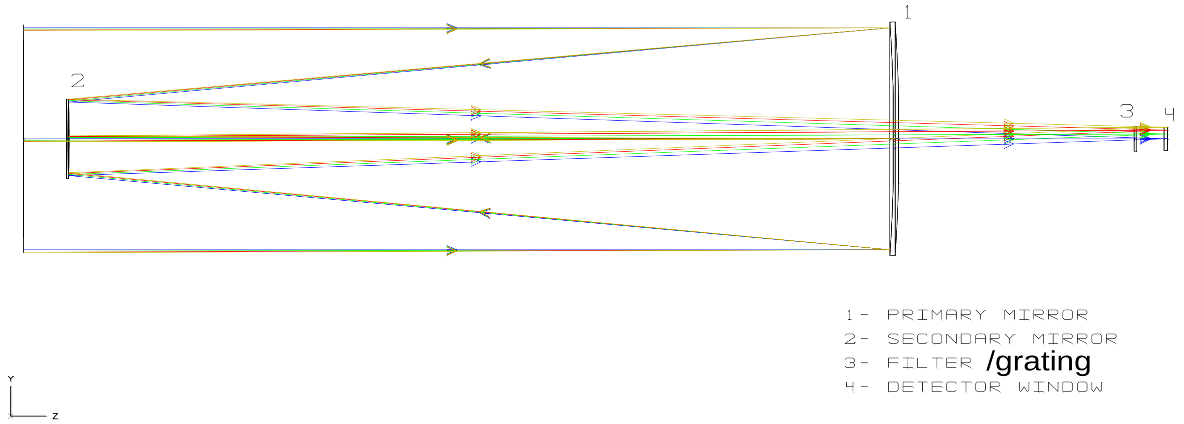

Fig. 2.2 Optical layout of the FUV telescope is shown. The primary mirror has a working diameter of 375 mm. The detector has a diameter of ~ 40 mm. The filters, each of diameter 50 mm, and the grating are mounted in a wheel at a distance of ~40 mm from the detector.

The plate scale is ~ 43"/mm. With a surface figure better than 1/50 waves rms (at 632 nm) for each of the mirrors, the PSF includes > 60% energy in diameter 1" at all wavelengths. In the NUV/VIS telescope, a beam splitter is used to reflect NUV and transmit VIS. Transmission leads to aberration in the VIS beam, and a cylindrical lens in used to reduce the aberration below 2" FWHM.

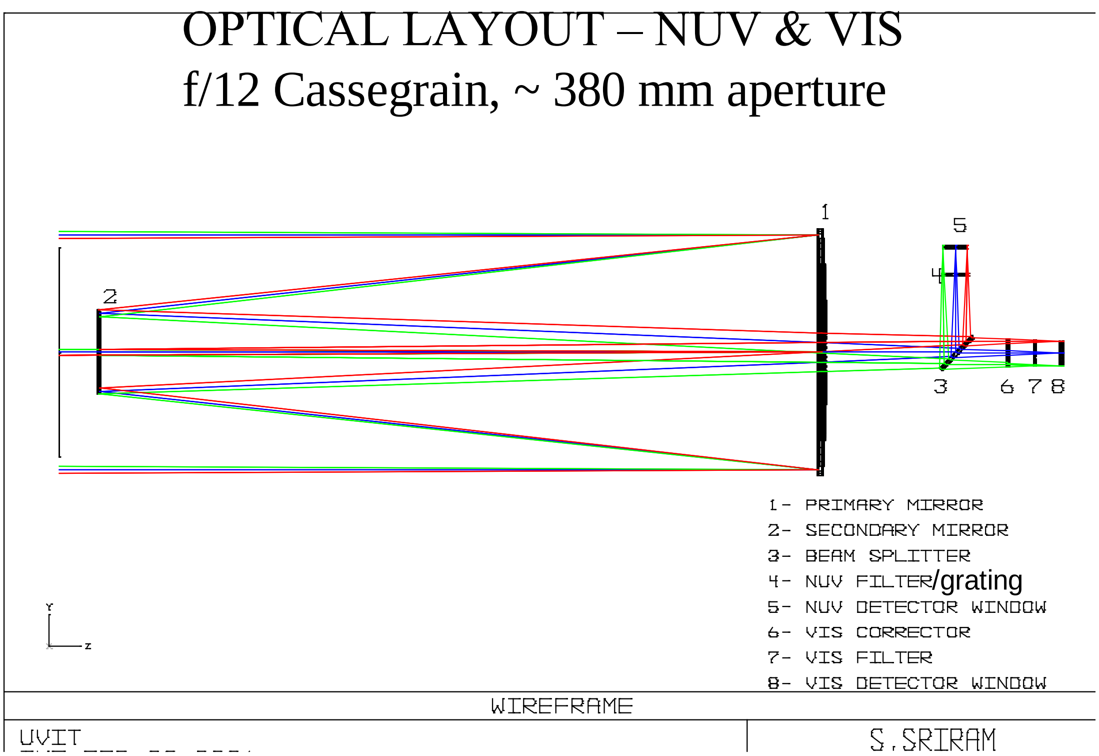

Fig. *2.3 Optical layout of the NUV /VIS telescope is shown. The primary mirror has a working diameter of 375 mm. A dichroic beam splitter is used for spectral division of the beam in NUV (reflection) and VIS (transmission). The detector has a diameter of ~ 40 mm. The filters, each of diameter 50 mm, and the grating (only for the NUV channel) are mounted in a wheel at a distance of ~ 40 mm from the detector.*

Filters

Filters for the three channels are listed in Tables 2.1 to 2.3**.** The transmission curves for the filters and the beam splitter are shown in Fig. 2.4 to 2.15. Thickness of each filter/grating is chosen such that the best focus is obtained at the same location for all the filters/grating of a channel. In OBS_ID, filters are identified as "F0, F1, ..." . Filters "F0, F1, ..." correspond to Slot No. "0, 1, ..." in the tables 2.1 to 2.3.

Table 2.1 FUV filter specification

Slot. No.	Filter Type	Filter Thickness mm	Pass Band nm	Name	Remark
0	Block				
1	CaF2-1	2.50	> 125	F148W	
2	Barium Fluoride	2.40	> 135	F154W	
3	Sapphire	2.00	> 142	F161M	
4	Grating – 1	4.52	> 125		
5.	Silica	2.70	> 160	F172M	
6.	Grating – 2	4.52	> 125		
7.	CaF2-2	2.50	> 125	F148Wa	Not Preferred

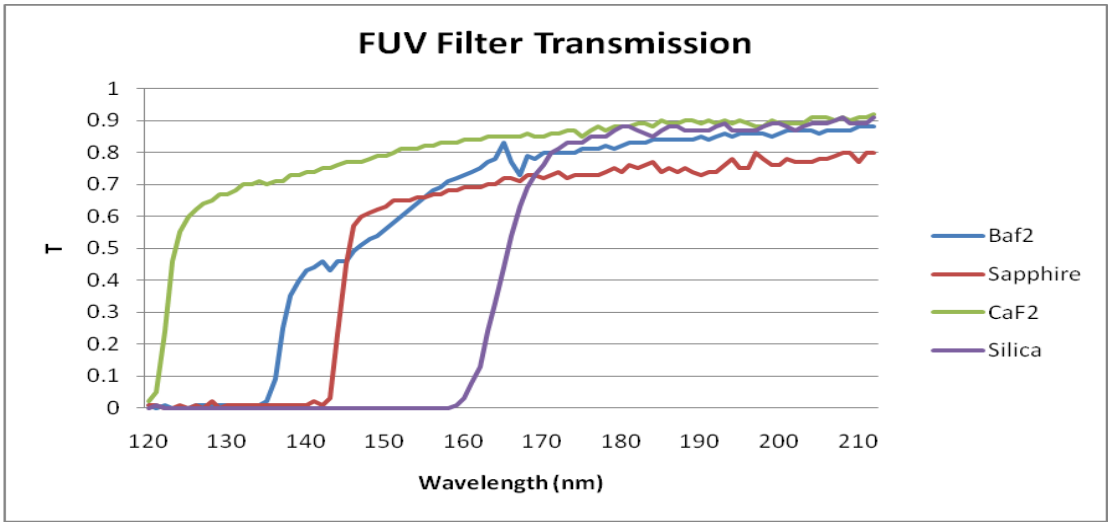

Fig.2.4: Spectral transmission of FUV filters measured in MGKML.transmission is shown for CaF2-1

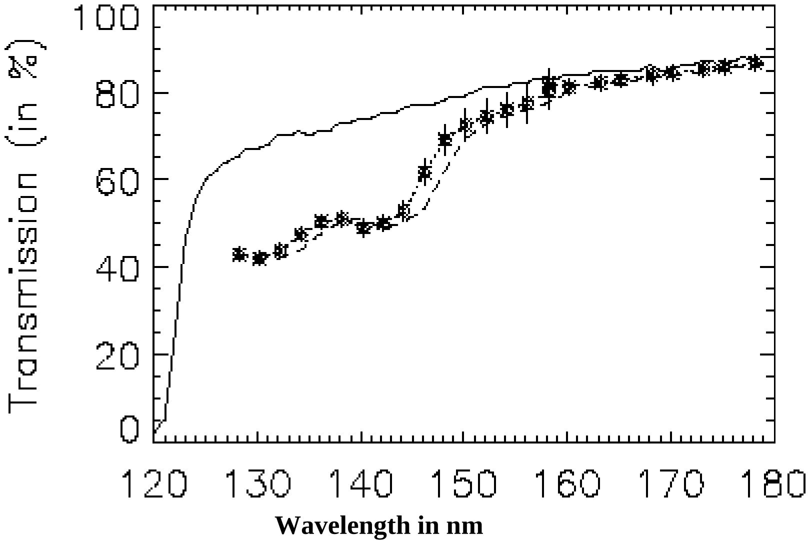

Fig. 2.5: Measured CaF2-2 transmission in MGKM Lab. of IIA. Exposure to water vapour, in the air, leads to reduction in the transmission from 125 nm to 150 nm. A recovery of the transmission is affected by long exposures to high vacuum

Table.2.2 NUV filter specification

Slot. No.	Filter Type	Filter Thickness mm	Pass Band nm	Name	Remark
0	Block				
1	Silica-1	3.00	> 200	N242W	
2	NUV15	2.97	200 – 230	N219M	
3	NUV13	3.15	230 – 260	N245M	
4	Grating	4.52	> 200		
5.	NUVB4	3.33	250 – 280	N263M	

6.	NUVN2	3.38	275 – 285	N279N	
7.	Silica-2	3.30	> 200	N242Wa	Not Preferred

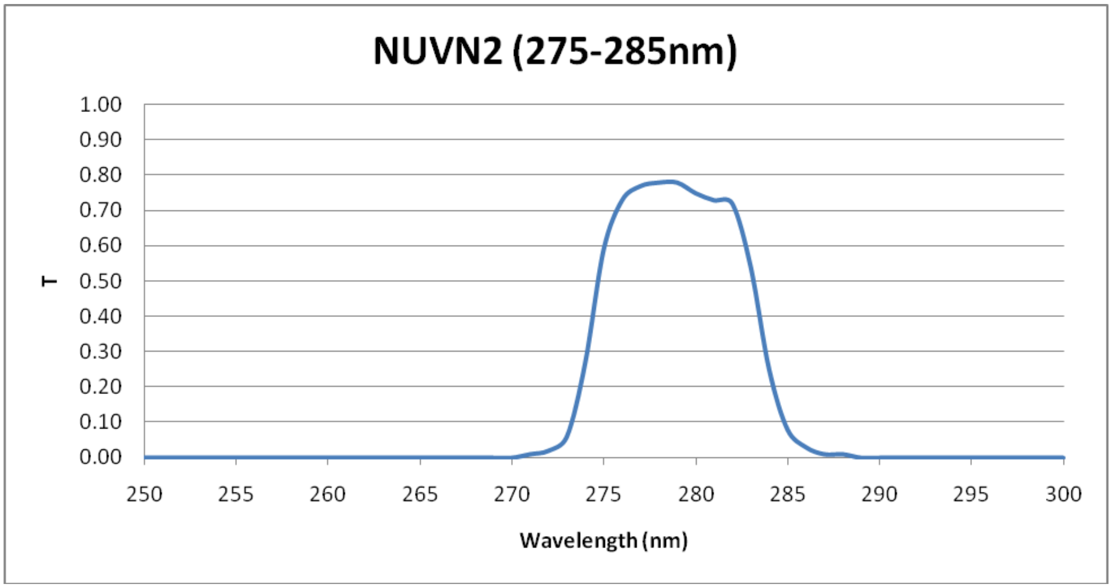

Fig. 2.6 Spectral transmission of NUVN2 filter measured in MGKML.

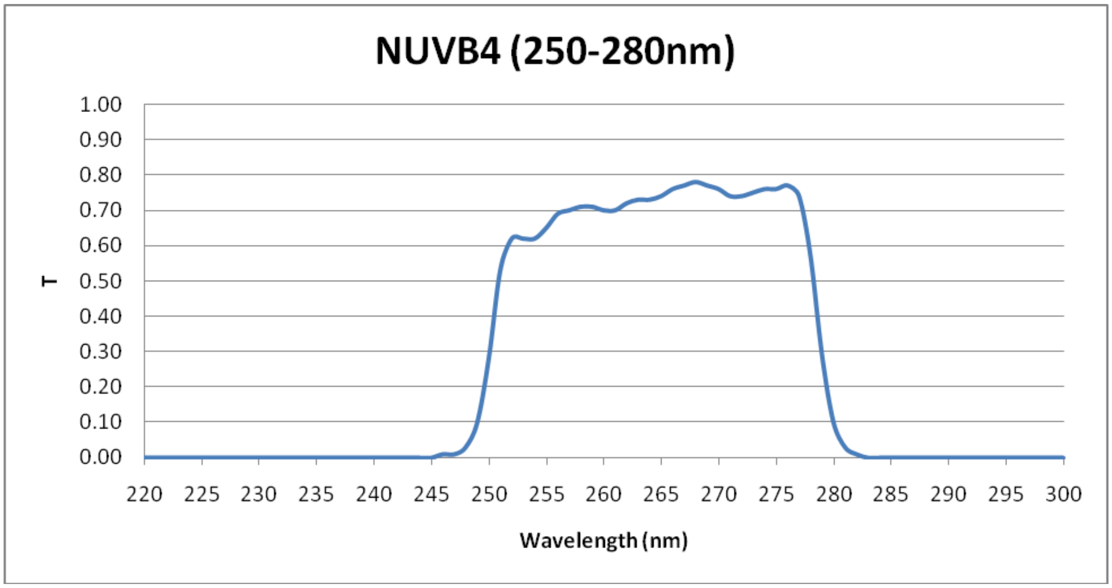

Fig. 2.7 Spectral transmission of NUVN2 filter measured in MGKML.

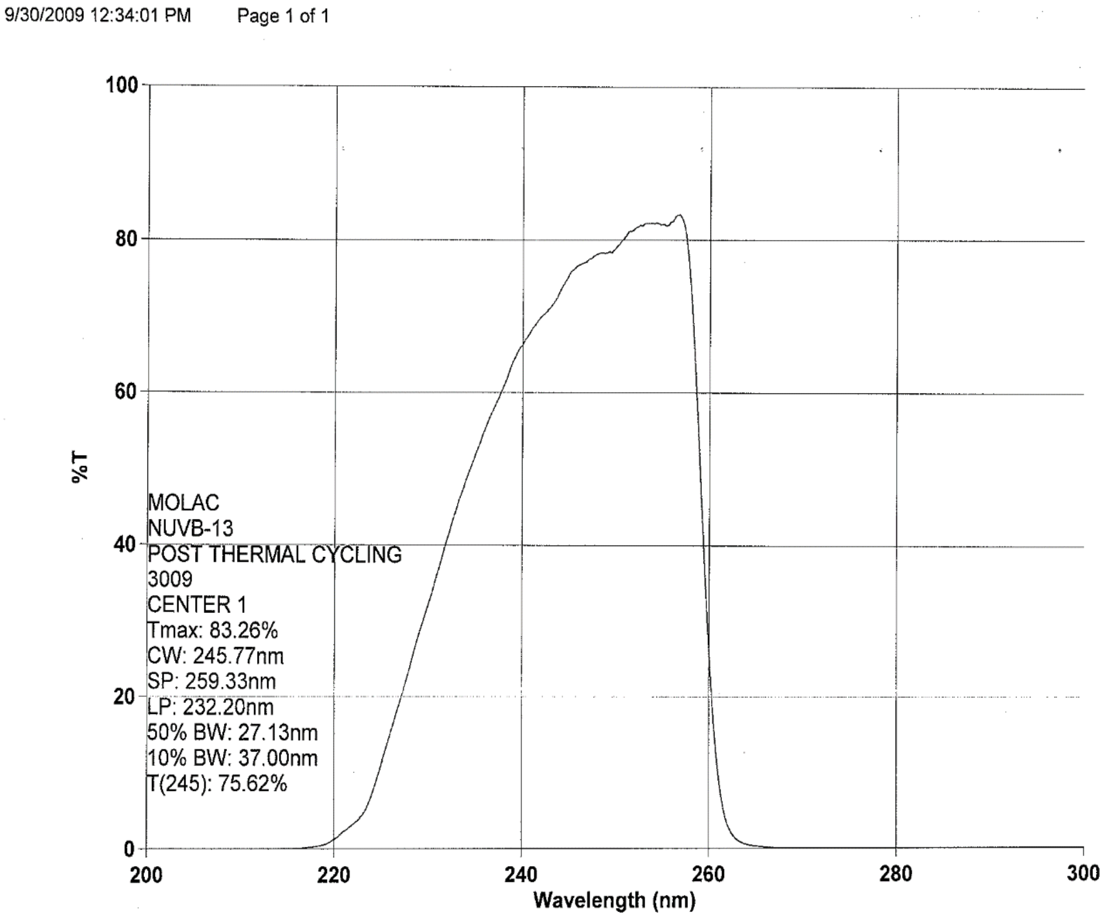

Fig *2.8: Spectral transmission of NUVB-13 filter obtained from supplier*

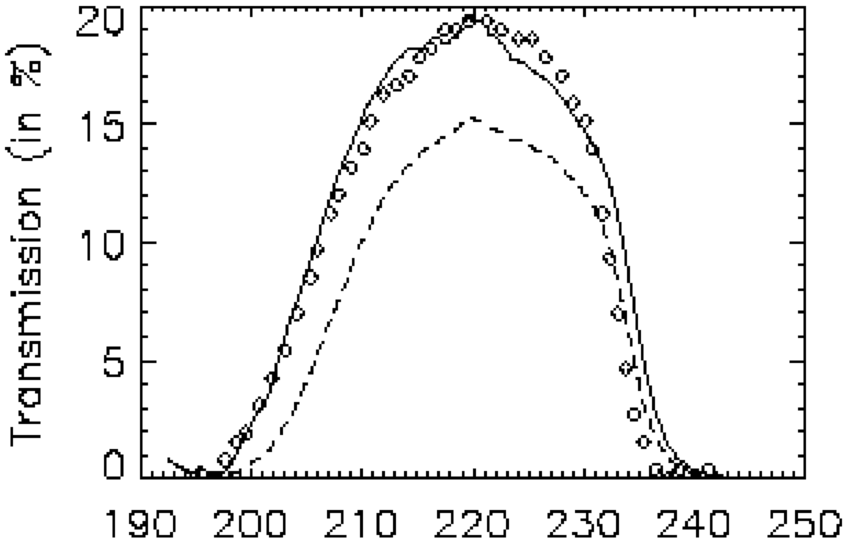

Fig. 2.9 Transmission curve for NUVB15 filter measured at LEOS Laboratory. Solid line: Vendors curve at the centre of the filter. Data Points (diamond): Measurements at the edges. Dashed line: Measurements at the centre. In these measurements wavelengths are shifted by +2.5nm to match curve from the vendor .

Table 2.3 VIS filter specification

Slot.No.	Filter Type	Filter Thickness mm	Pass Band Nm	Name
0	BLOCK	---		
1.	VIS 3	3.00	400 – 530	V461W
2.	VIS 2	3.00	370 – 410	V391M
3.	VIS 1	3.00	325 – 365	V347M
4.	Neutral Density Filter	3.00	> 380	V435ND
5.	BK7 – Window	3.00	> 320	V420W

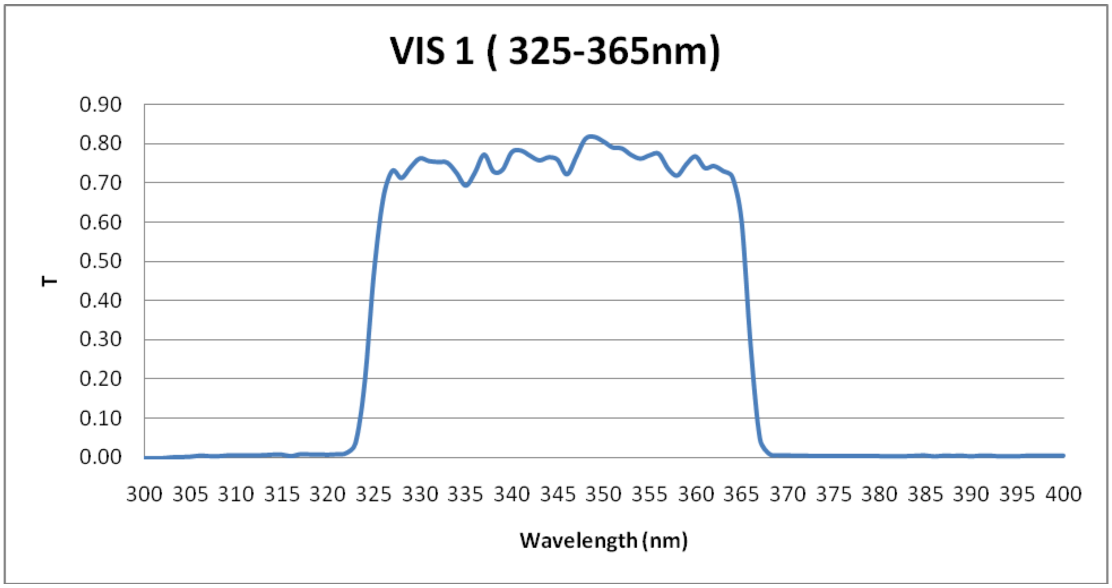

Fig2.10: Spectral transmission of VIS-1 filter measured in MGKML.

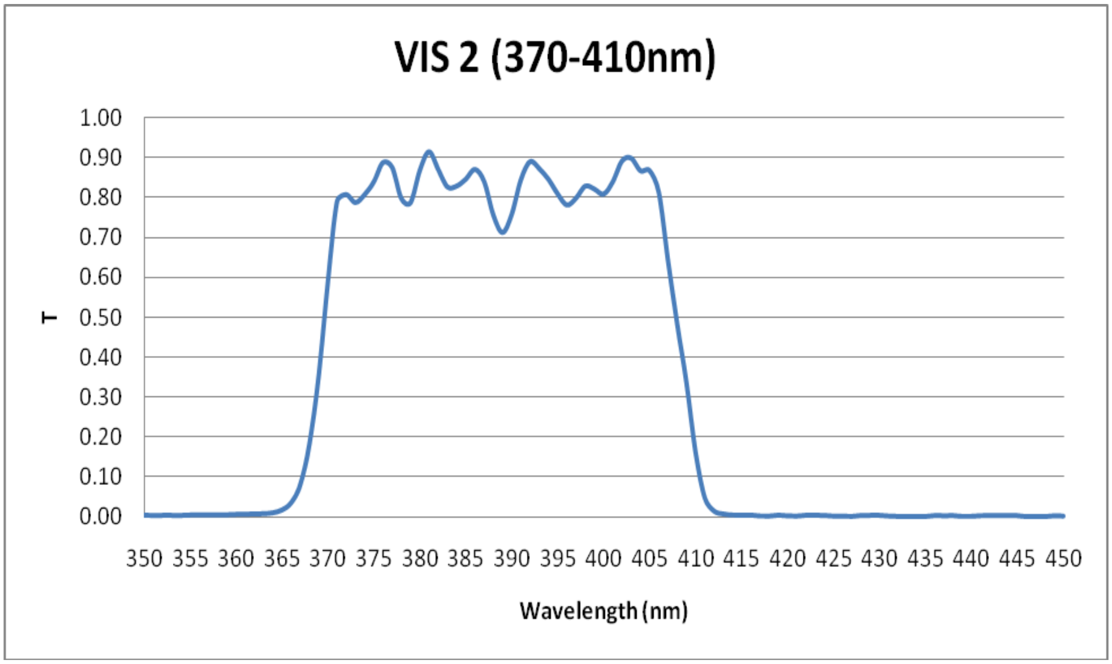

Fig. 2.11: Spectral transmission of VIS-2 filter measured in MGKML.

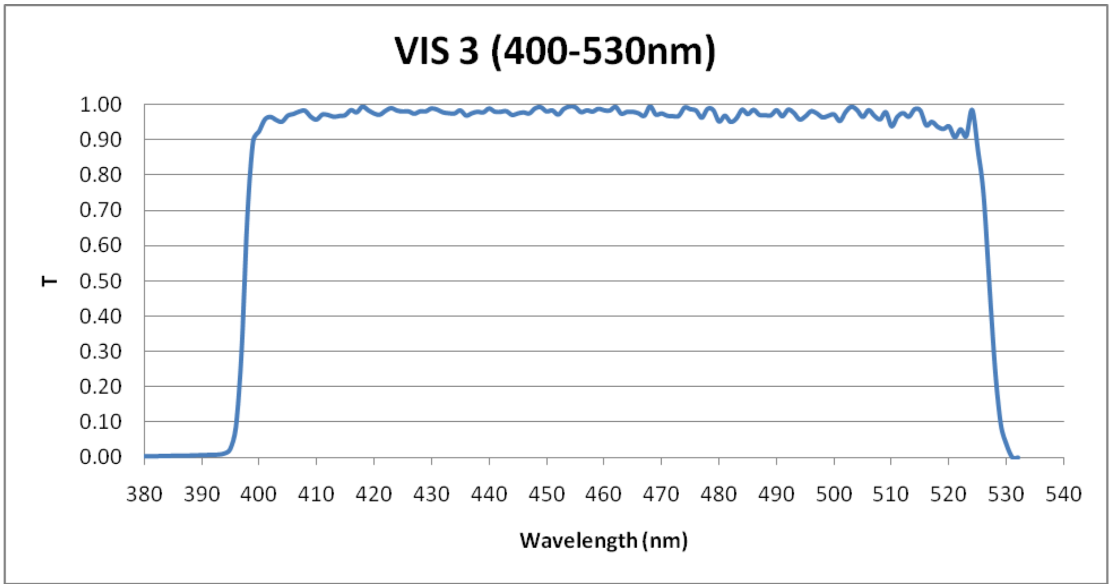

Fig2.12: Spectral transmission of VIS-3 filter measured in MGKML.

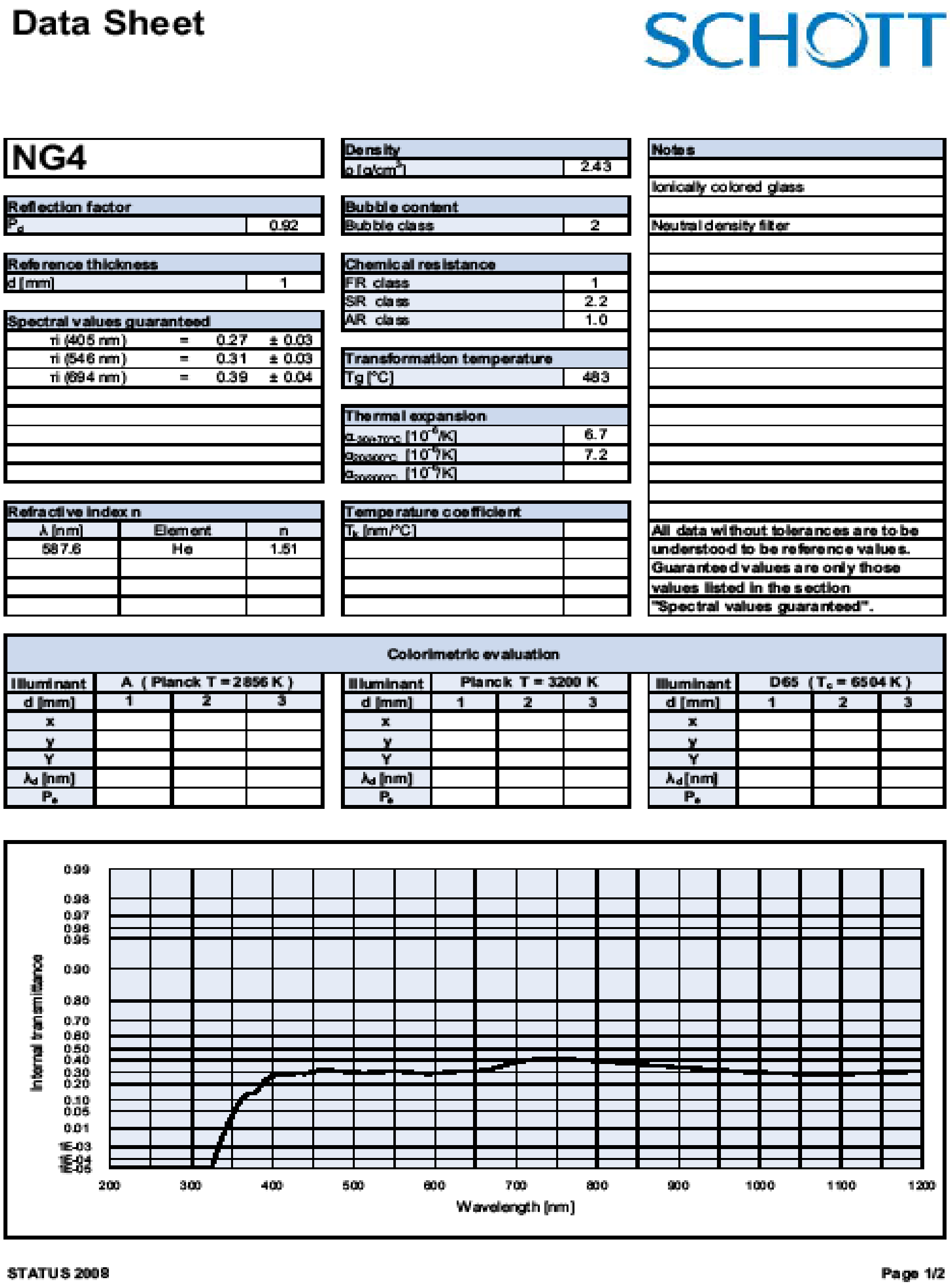

Data Sheet

SCHOTT

NG4

Reflection factor	
P_d	0.92

Reference thickness	
d [mm]	1

Spectral values guaranteed			
τi (405 nm)	=	0.27	± 0.03
τi (546 nm)	=	0.31	± 0.03
τi (694 nm)	=	0.39	± 0.04

Refractive index n		
λ [nm]	Element	n
587.6	He	1.51

Density	
ρ [g/cm³]	2.43

Bubble content	
Bubble class	2

Chemical resistance	
FR class	1
SR class	2.2
AR class	1.0

Transformation temperature	
Tg [°C]	483

Thermal expansion	
$\alpha_{-30/+70°C}$ [10^{-6}/K]	6.7
$\alpha_{20/300°C}$ [10^{-6}/K]	7.2
$\alpha_{20/200°C}$ [10^{-6}/K]	

Temperature coefficient	
T_k [nm/°C]	

Notes

Ionically colored glass

Neutral density filter

All data without tolerances are to be understood to be reference values. Guaranteed values are only those values listed in the section "Spectral values guaranteed".

Colorimetric evaluation

Illuminant	A (Planck T = 2856 K)			Illuminant	Planck T = 3200 K			Illuminant	D65 (T_c = 6504 K)		
d [mm]	1	2	3	d [mm]	1	2	3	d [mm]	1	2	3
x				x				x			
y				y				y			
Y				Y				Y			
λ_d [nm]				λ_d [nm]				λ_d [nm]			
P_e				P_e				P_e			

STATUS 2008

Page 1/2

Fig. 2.13 Internal transmission of VIS ND filter (Schott NG4) given by the vendor for 1 mm thickness. The actual thickness used is 3 mm and the net transmission is ~0.025at 450nm.

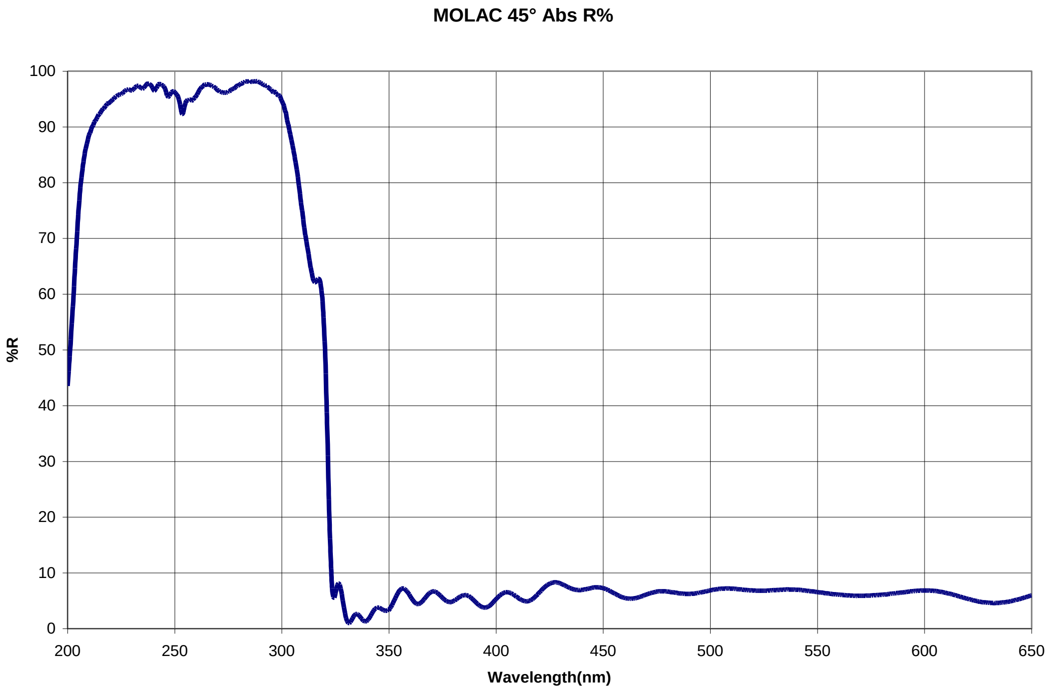

Fig. 2.14: Reflection efficiency of Beam splitter obtained from supplier.

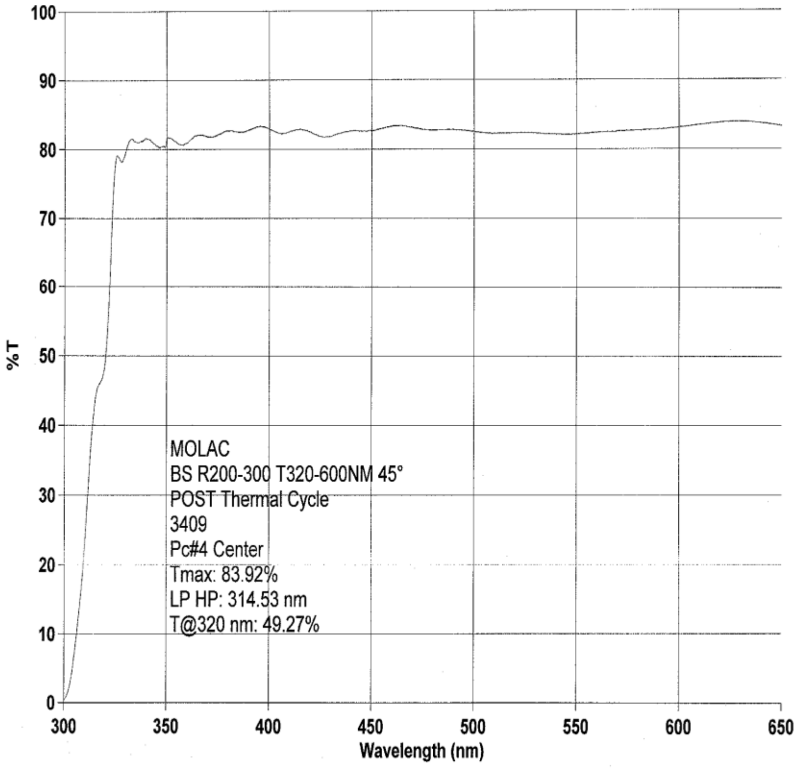

Fig. 2.15: Transmission efficiency of Beam splitter obtained from supplier

Gratings

The gratings, with 400 lines/mm, are ruled on CaF2 substrate of 4.52 mm thickness; the area of ruling is 36 mm X 36 mm (pl. see table 2.4). The dispersion obtained on the detector plane is 1.2 nm/ arcsec & 0.6 nm/arcsec in the first and second orders respectively at 136 nm, The transmission of the gratings is shown in Fig. 2.16 to 2.18. Aberrations are introduced by the grating and the PSF is ~ 2" FWHM.

Table 2.4 FUV/NUV Grating specification

.No	Parameter	FUV Grating		NUV Grating
	Substrate	CaF2	CaF2	CaF2
2	Grooves (lines/mm)	400	400	400
3	Diameter (mm)	52.00	51.95	51.99
4	Thickness (mm)	4.52	4.52	4.52
5	Ruled area	36x36mm	36x36mm	36x36mm
6	1st order peak wavelength (nm)	190	240	210*
7	2nd order peak wavelength (nm)	140	156	154
8	Crossover (nm)	150	175	166*

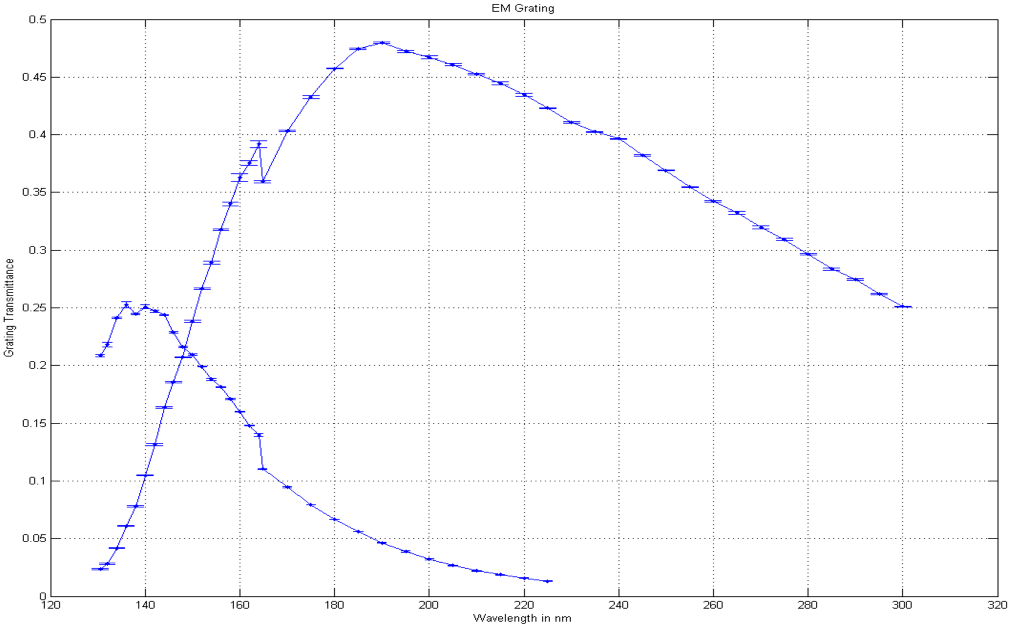

Fig. 2.16 : Transmission efficiency of FUV grating-1 measured in MGKML.

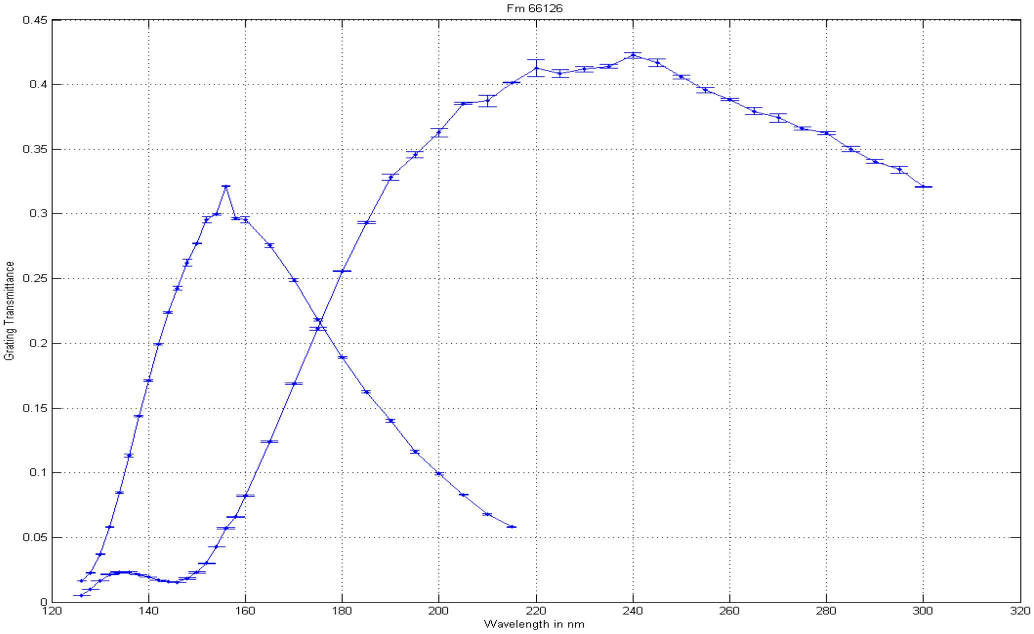

Fig. 2.17 : Transmission efficiency of FUV grating-2 measured in MGKML.

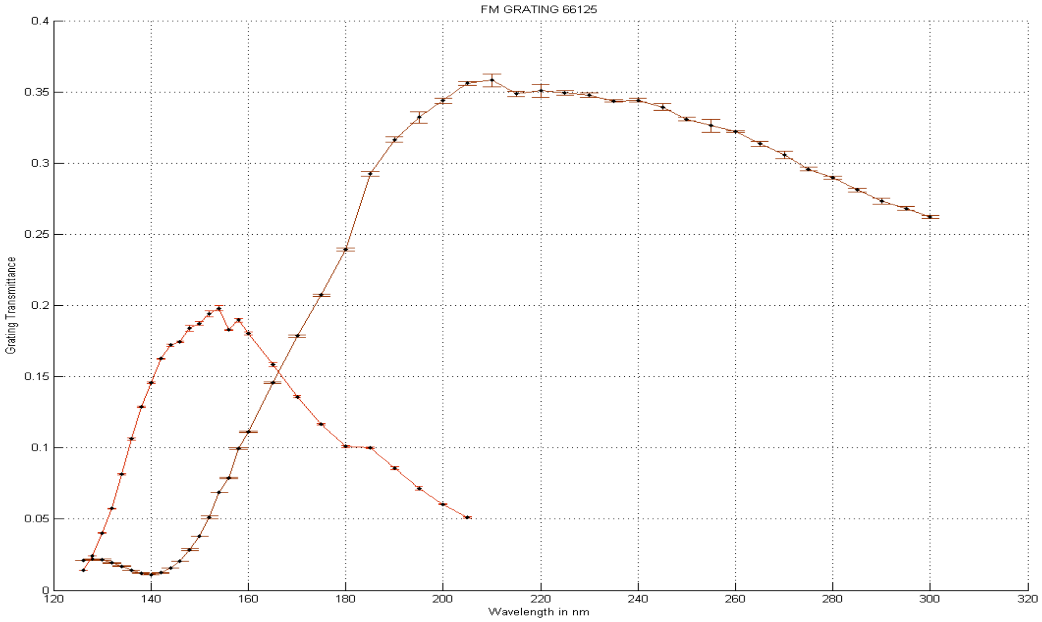

Fig. 2.18 : Transmission efficiency of NUV grating measured in MGKML.

Detectors

All the three detectors are intensified CMOS type with an aperture of ~ 40 mm diameter. Construction of the three detectors and their electronics are identical except for the photo-cathodes and the window. A 5 mm thick MgF_2 window is used for the FUV detector, while 5 mm thick silica windows are used for the NUV and the VIS detectors. A sketch of the detector module is shown in Fig. 2.19

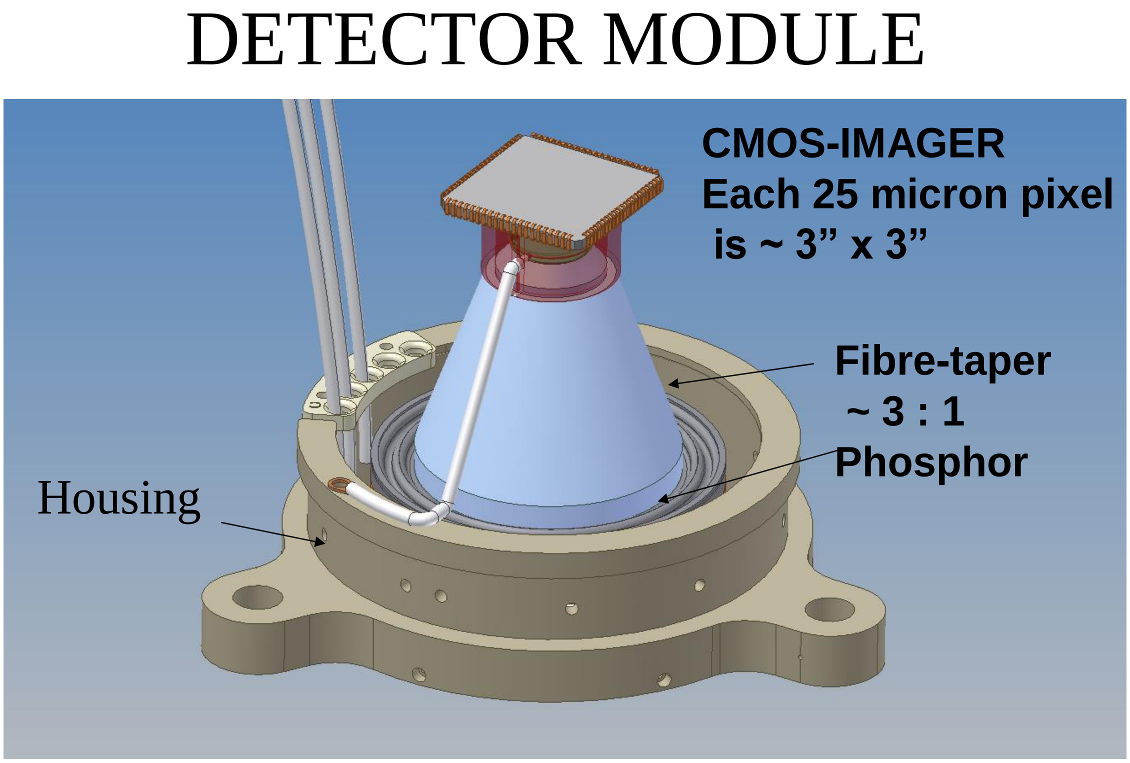

Fig. 2.19 : Configuration of the detector module is shown. At the bottom, and hidden by the housing, are the 5 mm thick window with photo-cathode deposited on it, and a set of two micro-channels-plates for multiplication (by up to about a million) of the photo-electron. The electrons are accelerated by ~ 5 kV and strike the phosphor to emit a pulse of photons. The light from phosphor is transmitted to Star-250 (C-MOS Imager) by a fibre-taper. The fibre-taper also matches the 40 mm diameter of the window to size of the C-MOS Imager (512 X 512 pixels of 25 X 25 microns).

Gap between the photo-cathode and micro-channel-plates is kept small (~ 0.1 mm) to minimize drift of the photoelectrons. With such small gaps, contribution of the detectors to the PSF is no more than ~ 1” FWHM.

The detectors can either be operated in photon counting mode (with a very high multiplication by the micro-channel-plates) where a list of coordinates of centroids of the detected photons is transmitted, or in integration mode with the multiplication kept at a low value where the raw frame of CMOS is transmitted. Typically the ultraviolet detectors are used in photon counting mode and the visible detector is used in integration mode. Either the entire array of 512 X 512 pixels can be read, at a max. rate of ~29 frames/s, to capture the full field, or a part of the field can be read in “window” mode at rates up to ~600 frames/s, depending on area of the window.

Thermal Effects

Variations in temperature can effect observations in several ways. Relative thermal expansion shifts focus of the telescope, and surface of the mirrors can get distorted. To minimize these effects, temperature of the telescopes is kept 20^0 +- 3^0 C and the structure is made of Invar. The mirrors are mounted on flexible supports made of Invar to minimize thermal stresses. There is no provision for adjustment of the focus in orbit, but the effect of temperature variations on the focus is expected to be small.

Transmission of the filters/gratings and quantum efficiency/gain of the detectors too can change with temperature. The temperature of these elements is kept in range 15^0 C to 30^0 C. The thermal effects are not calibrated on ground. As the photon counting mode is not very sensitive to the gain of the detector, this mode is affected less than the integration mode.

Correction for the drift is based on assuming that there is no relative drift between the three channels. Temperature variations can lead to relative drift between the channels, and this can only be modeled with in-orbit data.

Backgrounds

UVIT background has several sources. These are discussed below.

a) Dark counts in the detector:

At 20 degree C the dark photon counts are (as per the test data from Photek, UK , who supplied the CPUs of the detector systems):

VIS	NUV	FUV
1266/s	50/s	8/s

b) Bright limb of earth

At angles less than 45 from the axis, bright earth can give background which is in excess of the Zodiacal light.

c) Zodiacal light

Zodiacal light is ~ mag 22 per sq arcsec in the V band. This corresponds to ~ 5 x10^{-18} erg/(s A cm^2 $arcsec^2$) or ~ 0.08 detected photons per second per sq arcsec for an effective area of 50 sq cm for a band 5500 A to 6500 A. This background falls very slowly between 6000 A and 3000 A and it falls very fast at the shorter wavelengths. The photon flux per A is less by ~ 6 (300) at 3000 A (2000 A) as compared to that at 6000 A. These estimates are based on the data in "Chapter 6 of STIS Instrument Handbook for Cycle 21"., and the reader may find more information on backgrounds from this source.

d) Geocorona

Geocoronal lines are excited by solar radiations and vary in intensity by large factors. Typical counts of detected photons in the detectors, without filter, are listed below:

Geocoronal Line	Counts per second			
	FUV Detector (Effective Area 15 Sq cm)		NUV Detector (Effective Area 50 Sq cm)	
	Night	Day	Night	Day

1216 A Ly ά	129000	1290000		
1304 A OI	860	129000		
1356 A OI	64	12900		
2471 A OII			< 170	< 34000

It is clear that due to these lines observations cannot be made during the daytime in FUV channel. Further, the CaF_2 filter (the widest band filter in FUV) could have leak of a few percent for Ly ά, and the nighttime counts could be in range ~ 1000/s to 5000/s. The estimates in table are based on the data in "Chapter 6 of STIS Instrument Handbook for Cycle 21"., and the reader may find more information on backgrounds from this source.

Photon Counting and Integration Modes

The detectors can operate in two distinct modes:

i) Photon Counting Mode

ii) Integration Mode

In the photon counting mode, a very high multiplication is obtained in the MCPs such that each photo-electron generated in the short exposure (<100 ms) is detected as a light pulse in the CMOS imager, and its centroid is found. Thus, for each frame of exposure a list of centroid-positions is obtained from the detector. The expected spatial resolution in this mode is < 1.8" FWHM. If in a single exposure two or more photon events occur within a separation ~< 3 pixels of the CMOS imager (~ < 10"), these are detected as a single event or rejected as unacceptable event (see later discussion on choice of modes).

In the integration mode, multiplication of the MCPs is kept low, and signals in all the pixels of the CMOS detector are obtained. In this mode, many (weak) pulses of light, from many photo-electrons, could fall at the same location; the signal at any location is a measure of how many photo-electrons were detected. The expected spatial resolution in this mode is ~ 5" FWHM.

For imaging full field, minimum exposure time is ~ 34 ms. Therefore, given the background levels, imaging in the VIS channel in photon counting mode would lead to overlapping photon events. Further, the total flux of visible photons is such that in photon counting mode life of the MCPs would be exhausted in about one year. Hence, imaging in the VIS channel is normally done in integration mode.

Operational Constraints

Avoidance of ram-angle, Sun, and bright-Earth for safety:
In order to avoid any damage to coating of the primary mirror, due to atomic oxygen, a minimum angle of 12^0 is kept between the ram direction and the roll-axis, i.e. axis of UVIT. In order to avoid damage/UV-assisted contamination due to radiation from Sun/bright-Earth/Moon, a minimum angle of 45^0 / $12^{0/}15^0$ is kept between the axis and Sun / bright-Earth/Moon at all times even if UVIT is not observing.

Avoidance of bright objects:
Every field to be observed is checked for avoidance of very bright objects in a neighborhood of 2^0 radius; from 2^0., 1 part in 10^4 of the FUV flux could be scattered in the field.

Saturation with bright objects:
Any bright object which can give a detected photon count rate >1 count pr frame per ~ 10” X 10” would see serious saturation effects. Thus, to observe relatively bright objects in photon-counting mode a high frame rate can be used with partial field of view. (Minimum exposure time for the full field is ~ 34 ms, and it is ~ 2 ms for a field of 6’ X 6’.

Choices in Photon Counting Mode and Integration Mode

The nominal mode of observations for the ultraviolet channels is photon counting. Due to its large background, nominal mode of observations in the visible channel is integration mode with a low gain of MCP. To observe bright sources in the ultraviolet, either a high frame rate with a reduced (windowed) field can be used or the integration mode can be used. (As mentioned earlier, the spatial resolution in the integration mode is ~ 5” as compared to < 1.8” in the photon counting mode.)

In the photon counting mode a set of choices are available, in the hardware of the detector system, for selecting: a) thresholds for signals, in the pixels of Star250, to define a genuine photon event, and thus reject noise; a large threshold would reduce effective quantum efficiency, while a small threshold would bring in more noise-events, b) choice of centroiding algorithm for the events from a 3 square/5 square/3 cross windows. In addition, during the ground processing, a threshold can be set for rejecting bright pixels at the corners of the events to eliminate close pairs of photon events – this is required to minimize errors in determination of position of the centroid.

In the integration mode, the hardware allows selection of the gain of MCP by control of the high voltage. Thus, for a very bright source a very low gain can be selected to avoid saturation of the pixels of Star250.

Observing in Partial Fields

For the full field (~ 28’ circle), the maximum double frame rate is ~ 29/s. For those sources which have an intensity > ~ 5 photons/s/(10” X 10”), many frames would have close double photon events at this frame rate. In order to avoid double photon events for such sources a higher frame rate can be obtained by selecting a partial field for observations: the field is selected in units of pixels of Star250. The maximum frame rate is roughly in inverse proportion to area of the field. Thus, given the full field as 512 X 512 pixels, a rate of >600 frames/s is obtained for a field 100 X 100 pixels.

Choice is provided for the following sizes of partial fields, centered on the axis:

1. 100 X 100
2. 150 X 150
3. 200 X 200
4. 250 X 250
5. 300 X 300
6. 350 X 350
7. 512 X 512

In Photon Counting, frame rate is fixed at

1. ~ 640/s for 100X 100
2. ~ 300/s for 150 X 150
3. ~ 180/s for 200 X 200
4. ~ 115 /s for 250 X 250
5. ~ 82/s for 300 X 300
6. ~ 61/s for 350 X 350
7. ~29/s for 512 X 512.

Caution:
In window mode the data rate can be very high as each frame carries an overhead of 4kBytes and the maximum data rate allowed for the total of FUV and NUV images is 10 Gbits/orbit. The ex[osures asked for should respect this limit, i.e. for each orbit the total data for FUV and NUV images should be such that
((Number of FUV frames + Number of NUV frames) * 32000 + Time of exposure * 500000) < 10^{10}.

If Integration is selected, exposure time per frame can be selected as per the following:

1. For 100 X 100: in range 0.02 s to 0.30 s, steps of **0.02s**
2. For 150 X 150: in range 0.05 s to 0.45 s, steps of **0.02s**
3. For 200 X 200: in range 0.08 s to 0.65 s, steps of **0.02s**
4. For 250 X 250: in range 0.12 s to 0.80 s, steps of **0.05s**
5. For 300 X 300: in range 0.17 s to 0.95 s, steps of **0.05s**
6. For 350 X 350: in range 0.25 s to 1.10 s, steps of **0.05s**
7. For 512X 512: in range 0.50 s to 1.70 s , steps of 0.1s

Please note that all these options for integration mode are not operational. The only options available are :
For VIS :
only 512x512 window size, and with averaging of {16} frames for transmission, with ROW_GAP_TIME adjusted to achieve a frame_time of ~ 0.94 s for the averaged frame.

Please note that the design allows for selection of partial field of any size and at any position of the full field. However, for simplifications of the operations only some choices of square shaped partial fields, around the centre, are given. An off-centre partial field would call for a certain orientation of the field in addition to correct pointing of the axis, while safety of UVIT require that the field be oriented such that the sun is behind the doors.

Timing Observations

While the main focus of UVIT is not for timing observations, it is possible to record absolute time of each photon event, along with its position, with an accuracy < 5 ms. For such observations, the analysis on ground would generate a time series of all the detected photons along with their positions on the sky.

Observation Sequence

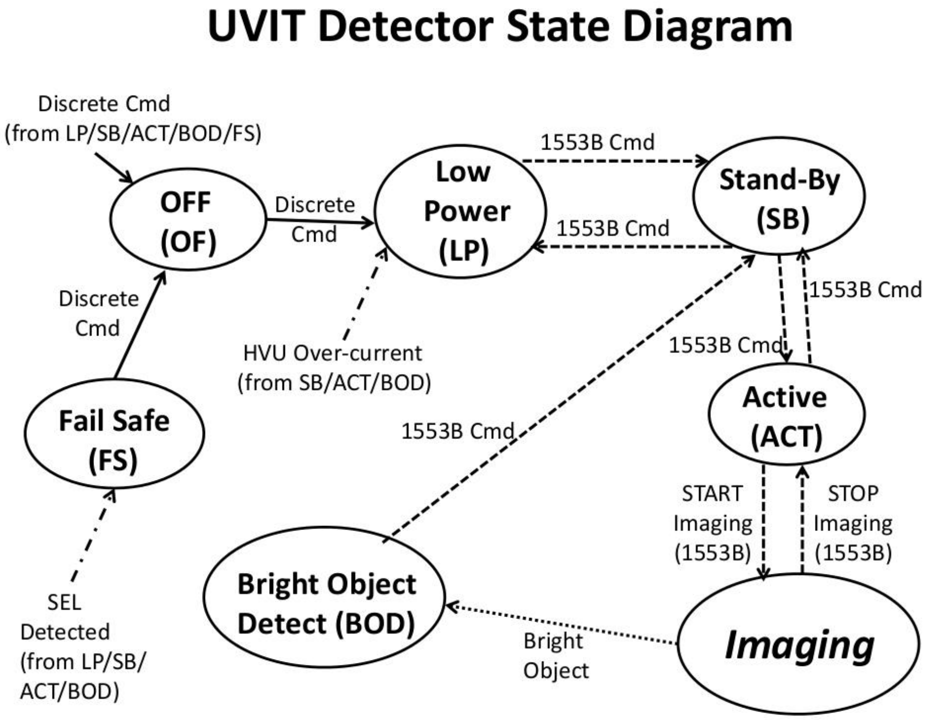

Fig. 2.21 : State diagram for UVIT

Modes of operation of UVIT

Description of Filter-Detector systems:

A brief description of the UVIT's Detector-Filter system will help comprehend the details of their OPERATION, which is somewhat complex. It will also help clarify the various acronyms used in the text.

The UVIT Filter system (for each of the 3 channels) consists of two distinct physical sub-units : Filter-Wheel-Motor Assembly (FWMA) & Filter-Wheel Drive Electronics (FWDE). The FWMA is located between the back of the primary mirror of the telescope and the Detector system. The FWDE is located on the spacecraft deck (inside the cuboid structure). Electrical signals run via ~ 4.5-m long cables between the FWDE & FWMA via a patch-board located near the focal volume of the 2 telescopes. All 3 FWDE units are housed inside the same mechanical enclosure / box.

The Detector assembly (for each of the 3 channels) consisting of the intensifier tube, fiber-optic-taper, CMOS image sensor and its fan-out board, electrical connectors & HV cables, is termed as 'Camera Proximity Unit' (CPU). The CPU is located at the focal plane of the respective channel (at the back of the telescopes; behind the primary). The High Voltage Unit (HVU) for the corresponding channel which generates the 3 voltages (V_PC, V_MCP & V_A), is located near CPU itself minimizing the lengths of the HV cables. The HV cables are an integral part of the CPU & connect to the HV connectors on the body of the HVU. The drive electronics for the CMOS sensor as well as the signal processing (including centroiding) is located in a separate unit called 'Read-out Electronic Assembly' (REA) located on the spacecraft deck (similar to FWDE). All 3 REA units for the 3 channels are housed inside a single mechanical enclosure / box, called the Electronics Unit (EU). The electrical cables between REA & CPU are through long cables via the patch-board (see above). Similarly REA & HVU are electrically connected through similar long cables via the patch-board. It is important to note that while all commands for Filter system (FWDE) are through conventional dedicated conductors between spacecraft system (Bus Management Unit, BMU) and the FWDE, carrying relevant electrical signals (for Pulse or Data commands), the control of various selectable parameters of the Detector & related read-out Electronics system as implemented within each REA, is programmed via the serial (1553B) communication link with the spacecraft sub-system BMU.

While all the science data from the Detector system flow through the spacecraft's Data Handling Unit (DHU), the status of the Filter wheel are available exclusively through the Low Bit-rate Telemetry (LBT).

Modes of the Detector :

Each of the 3 Detector sub-systems (corresponding to the 3 wavelength channels) are identical in regard to the 'Modes' in which they can be at any given time. The modes are like 'states' and they are named as :

a) Off
b) Low Power
c) Standby
d) Active
e) Bright Object Detected
f) Fail Safe

In 'Off' mode, all three units REA, HVU & the CPU are in powered off state. Only a discrete pulse command can take the detectors sub-system from 'Off' state to 'Low Power' state.

In 'Low Power' state, the REA is powered but the HVU and the CPU are still off, and 1553B communication line is now operational (ready to accept commands & respond to telemetry requests from the BMU).

Using a 'change-state' command via 1553B link, the detector can be taken from the 'Low Power' mode to 'Standby' mode and vice-versa. In this 'Standby' mode, in addition to the REA, the HVU and the CPU are also powered on (however, all the three control voltages of the HVU, viz., for Photo-Cathode, Micro-Channel-Plate & Anode are Low/zero).

In order to attain full functionality (of imaging), the detector system must be taken from 'Standby' mode to 'Active' mode via a 1553B command. Once in 'Active' mode, issuance of 'Star Imaging' with all the imaging parameters, initiates ramping up of the HVU & imaging as per programmed parameters. The science data stream now starts feeding the DHU sub-system. The imaging can be stopped by issuing a 'Stop Imaging' command (without leaving the 'Active' mode, meaning that we can re-start imaging with say, some different imaging parameters) or directly making a state-change to 'Standby'. All imaging is carried out in 'Active' mode only. Imaging parameters can be loaded only by the 'Start Imaging' command.

From the above, it should be clear that only certain sequences of changes of state of the detector system are meaningful (as evident from the state-diagram - Fig. 2.21 & Table 2.5). On receipt of any command implying departure from the allowed sequences, the command is ignored - and a suitable error flag raised for follow up safety actions by the BMU.

Table 2.5: State table of the detector system for exception cases

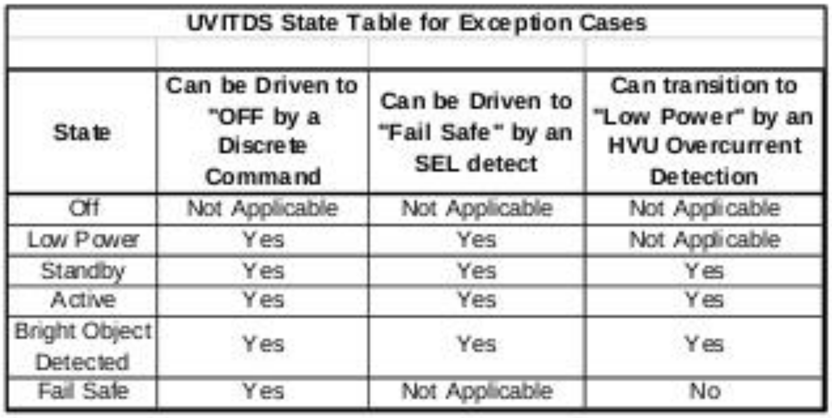

UVITDS State Table for Exception Cases

State	Can be Driven to "OFF by a Discrete Command	Can be Driven to "Fail Safe" by an SEL detect	Can transition to "Low Power" by an HVU Overcurrent Detection
Off	Not Applicable	Not Applicable	Not Applicable
Low Power	Yes	Yes	Not Applicable
Standby	Yes	Yes	Yes
Active	Yes	Yes	Yes
Bright Object Detected	Yes	Yes	Yes
Fail Safe	Yes	Not Applicable	No

Emergencies

Emergencies related to the Detectors

Recovery from any of the emergencies described here, involve action from ground station (i.e. there is no auto-recovery based on onboard logic).

1. While imaging, a Bright Object Detected (BOD) flag is generated in case certain conditions (above selectable thresholds) are encountered. These thresholds are: (i) intensity level (event height), (ii) size (event length in pixels along one axis) & (iii) persistence of this condition (over successive number of frames; to avoid 'false alarm'). The BOD flag/alarm is a 1bit hardware logic signal over a dedicated line (per UVIT channel), which is periodically monitored by the spacecraft system BMU. On receipt of BOD alarm, the BMU suspends all previously planned operations of UVIT & takes necessary action (issuance of commands) to take all 3 channels of UVIT into a 'safe' state. This includes: parking the filter wheels in 'light Block' condition, taking each of the 3 REAs to finally 'Low Power' mode via intermediate steps.

2. Another form of 'alarm'/emergency, possibly related to bright objects in the field is: Over Current (OC) of any of the High Voltage supplies. In this case, the channel detecting OC itself goes in to 'Low Power' mode & signals a flag to the BMU in the LBT telemetery (one bit in the1553B frame). BMU on receipt of the OC flag, will take action sequence leading to Power Off for all 3 channels (the sequence includes : suspension of all previously planned operations of UVIT; safe parking of filter wheels; all relevant intermediate steps to arrive at the Power Off' condition).

3. Yet another form of 'alarm'/emergency (possibly related to high charged particle background), occurs when the onboard electronics detects a Single Event Latchup (SEL) situation. The affected channel itself moves to a FAILSAFE state (with its secondary power system internally disabled), while the BMU detects this state from its periodic monitoring of the supply (+3.3 V) line. The BMU then takes all 3 channels to Power Off state following the usual sequence of intermediate steps.

4. An additional type of emergency occurs, when the 1553B command acknowledgment frame received from REA, has any one (or more) of the 'errorflagbits' in 'set' state. This implies at least one of the programmed selectable imaging parameters is 'wrong' (incompatible with current state) & hence that command frame has been ignored by REA. This means an error has occurred possibly in the mission planning software & hence the UVIT operations need to be shutdown till the cause is understood (just like any of the emergencies). On encountering this kind of emergency, the BMU takes all 3 channels to 'Low Power' state via usual sequence of intermediate steps.

5. Housekeeping values out of acceptable range : when any of the few selected temperatures & power supply voltages is found to be out of its acceptable operating range, this emergency is triggered. Although this out-of-range condition may have been detected in one channel, all the 3 detector systems of all the 3 channels are taken to 'Low Power' state via usual sequence of intermediate steps.

Emergencies related to the Filter wheels:

In case the filter wheel status shows abnormality (e.g. being in 'acquire'/slewing state for a time much longer than normal), BMU takes all 3 channels of UVIT to 'Low Power' state via usual sequence of intermediate steps (including parking the filters to 'light block' configuration).

Typical Observing Sequence

From the safety point of view of the UVIT payload, during all slews of the spacecraft, the Filter wheel is parked at the SAFE ('lightblock') configuration. Even when a UVIT channel is not being used for any observations, that channel is normally left in 'Standby' mode [this is to minimize the number of hard OnOff cycles over the mission life].

A typical observation sequence (for exposure with one filter) consists of the following steps [starting with filter at 'SAFE' parked configuration and Detector in 'StandBy' state, as stated above; assuming imaging in Photon Counting mode] :

The spacecraft (BMU) verifies that:
(A) the UVIT is presently in a 'SAA Safe ZONE'
(B) selected UVIT health parameters (temperatures & supply voltage monitors) are within allowed range
(C) the spacecraft attitude (AOCS) is at the target position

(1) Change state of the REA from 'Standby' to 'Active' mode;

(2) Collect DARK1 (for Star250 C-MOS imager) Image frames in Integration Mode, and High Voltages 'Low' [this involves 'Start Imaging', data collection & 'Stop Imaging' sequence of operations];

(3) Move from 'Active' state to 'StandBy';

(4) Prepare the Filter Wheel for motion by issuing 'Safe Reset';

(5) Move the Filter Wheel by issuing 'Target angle' (Filter selection for this observation);

(6) 'Kill time' for sufficient duration so that the Filter would have reached the destination;

(7) Disable Filter Wheel Motor (coils de-energized) to save power;

(8) Move from 'StandBy' to 'Active' state;

(9) Begin Imaging by issuing 'Start Imaging' command, which includes all imaging parameters;

(10)'Kill time' appropriate for the duration of the current exposure;

(11)Issue the 'Stop Imaging' command;

(12)Move from 'Active' state to 'StandBy';

(13)Park the Filter Wheel in SAFE ('lightBlock') configuration;

(14)'Kill time' for sufficient duration so that the Filter would have reached the destination;

(15)Disable Filter Wheel Motor (coils de-energized) to save power;

(16)Move from 'StandBy' to 'Active' state;

(17)Collect DARK2 (for Star250 C-MOS imager) Image frames in Integration Mode, and High Voltages 'Low' [this involves 'Start Imaging', data collection & 'Stop Imaging' sequence of operations];

(18)Move from 'Active' state to 'StandBy';

[Now the channel is back to its starting position; Detector (REA) in 'StandBy' & Filter wheel at 'SAFE'.]

Observations in Daytime

The backgrounds in daytime, due to geocorona and due to scatterings in ASTROSAT, are very large. However, in *exceptional* cases observations during the daytime may be considered, with reduced sensitivity, as long as the sun is > 90 deg. away from the field and limb of the earth is > 12 deg. away.

Optimisation for calibration with multiple nearby pointings in multiple filters

Change of a filter takes ~ 30 s. In addition, before every change of the filter the high voltages on the detector are taken to zero and then ramped up after the new filter is in position, which takes another ~30 s. Thus, observations for flat-field calibrations, by placing the calibration source at different parts of the field separated by < 10’, can be finished in one filter by changing pointing before changing to the next filter. *In all other cases*, the largest overhead would be time to change pointing and it is best to finish all the observations on one object before moving to the next.

Quantum Efficiencies

Quantum efficiencies of the detectors have been measured in photon counting mode, with reference to a NIST calibrated photo-diode. These are shown in Fig. 2.22.

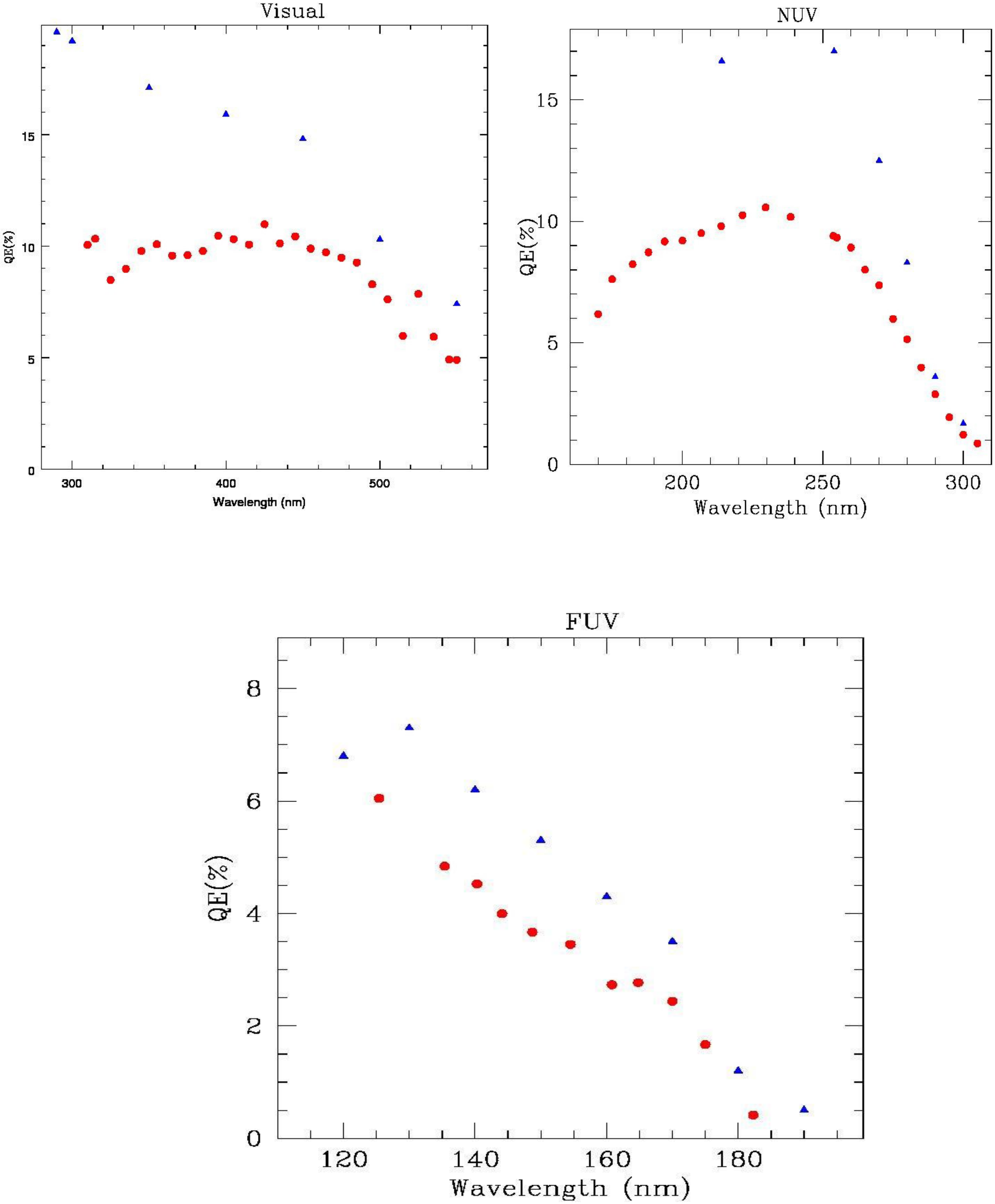

Fig. 2.22 : QE values for Ph. Counting mode are shown as red circles. The blue diamonds are QE values for the photo-cathodes measured by the vendor.

Effective Area

Based on the tests done on the various optical components, the effective areas have been estimated as a function of wavelength for all the filters. These are shown in Fig. 2.23, 2,24, and 2.25.

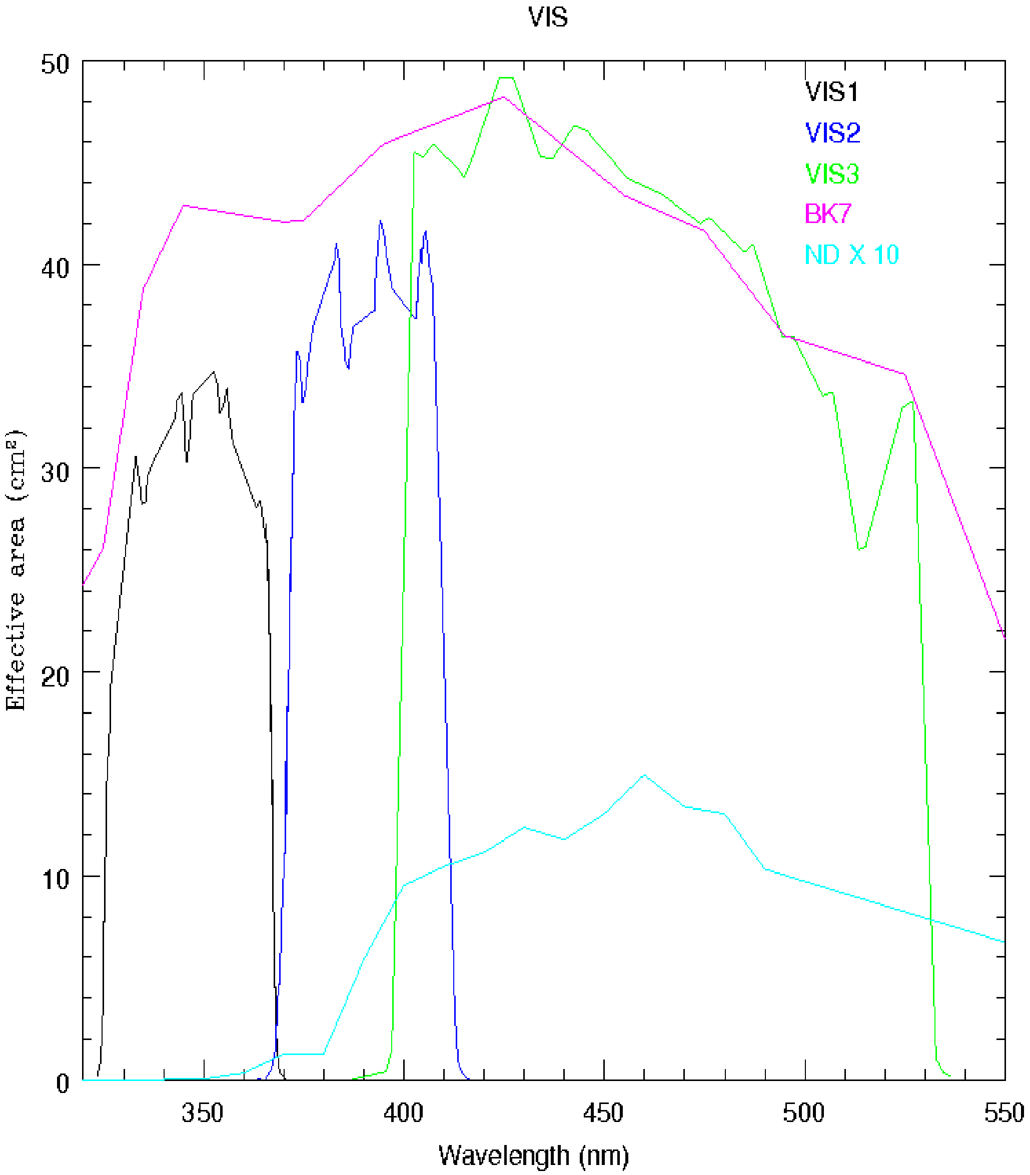

Fig. 2.23: Estimates of the effective area are shown for the filters of VIS channel.

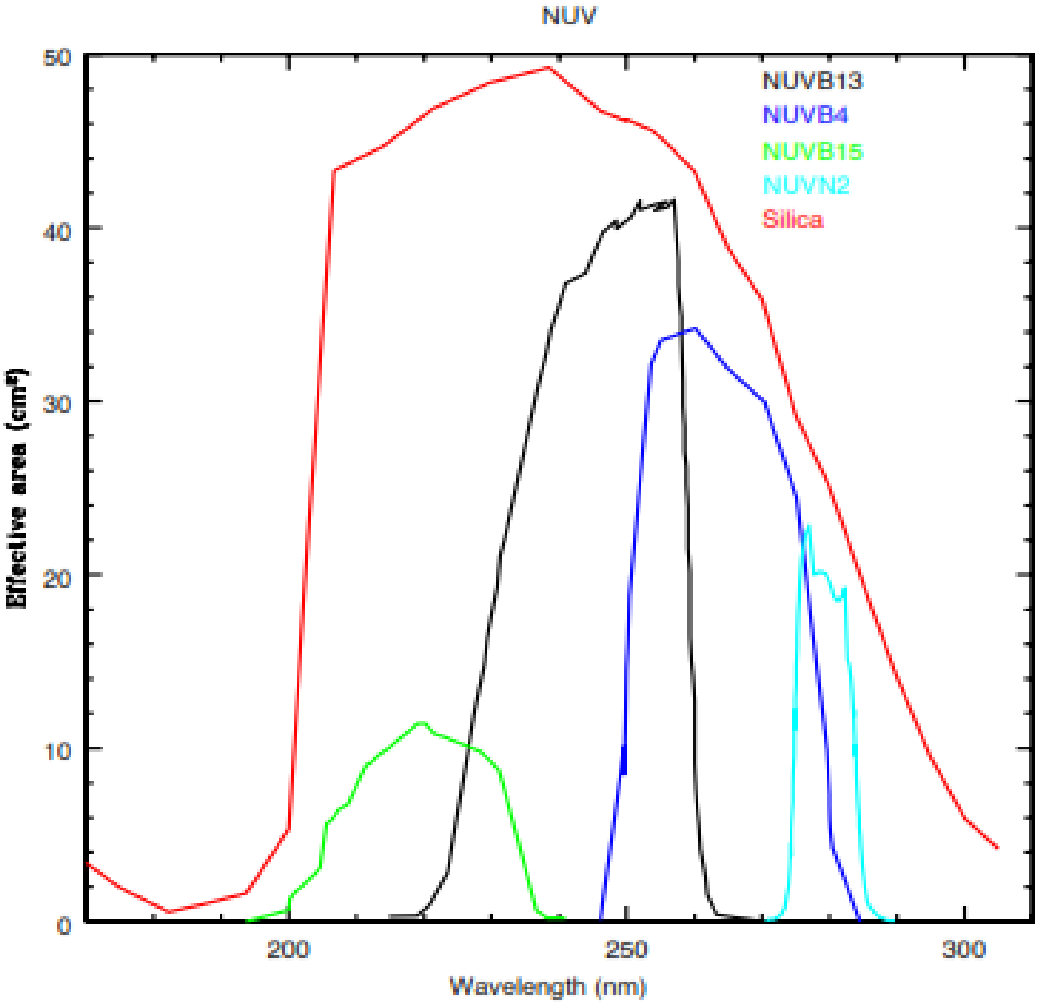

Fig. 2.24: Estimates of the effective area are shown for the filters of NUV channel.

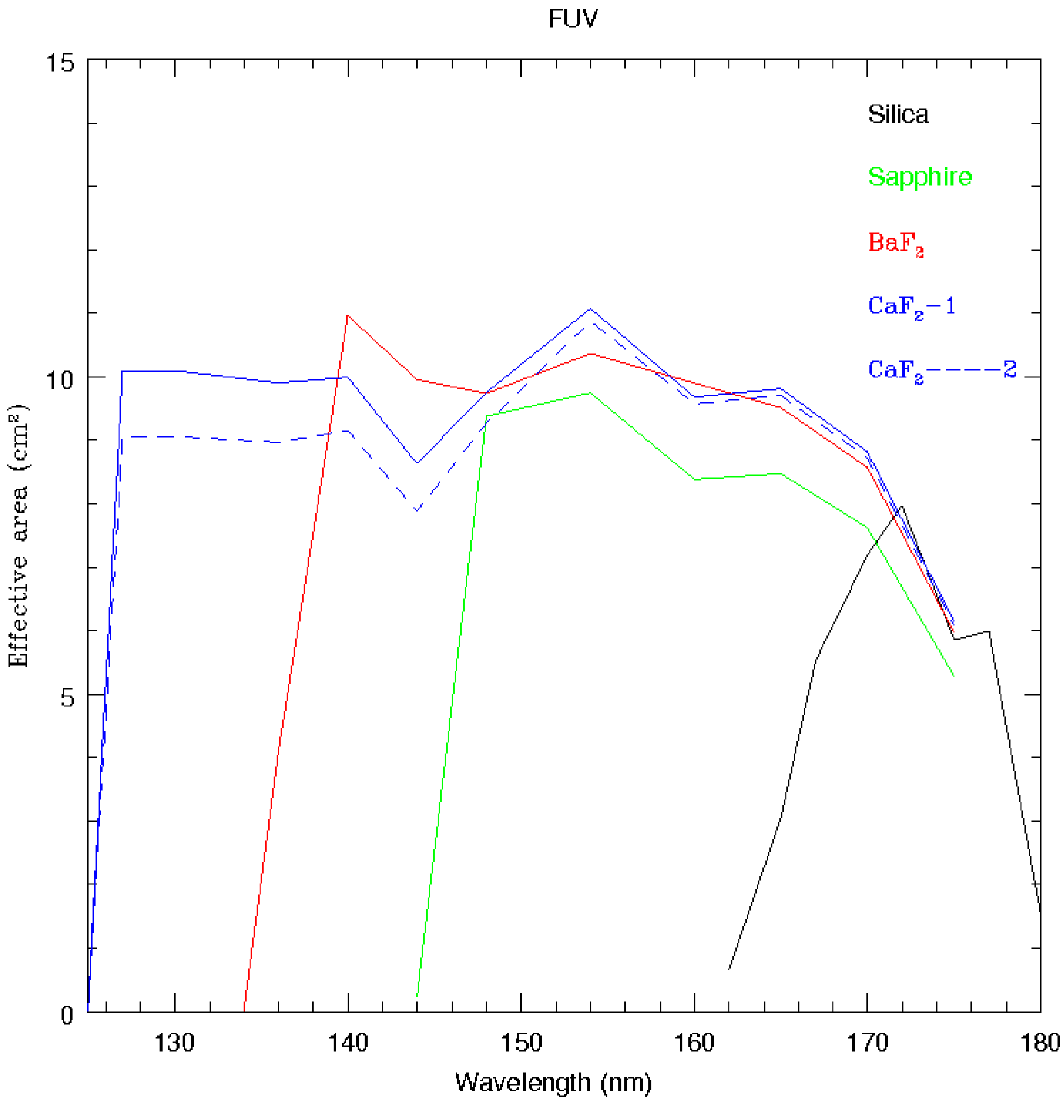

Fig. 2.25: Estimates of the effective area are shown for the filters of FUV channel. The effective area at 200 nm (250 nm) is estimated as 1.85 (0.1) sq cm. "

Calibration details

The calibration of the UVIT instrument is achieved through ground-based as well as in-orbit tests. The individual components of the UVIT instrument are tested and calibrated in the ground. The performance of the integrated system is tested during the performance verification phase after the launch. The results are presented below.

Ground based tests:

Detectors:

The CMOS-intensified imagers used in the three UVIT channels are tested at the Canadian facility in the University of Calgary, and at Indian Institute of Astrophysics at Bengaluru. The tests performed on the detector include tests for quantum efficiency as a function of wavelength, spatial variation of sensitivity, tests to estimate the centroid of the photons detected, gain as a function of MCP voltage etc., and distortions. These tests were done on both the EM and the FM detectors. Many of these results have been summarized in the preceding subsections, and to that we can add: a) based on the measurements on witness samples, reflectivity of the mirrors is estimated as ~ 70% in FUV and ~ 80% in NUV and VIS, b) any variability in sensitivity, on scales < 20 mm, is <5%.

All the details will be included in the calibration database.

Filters and gratings:

The EM and the FM filters are tested for their transmission and its spatial variability. No variability of > 5% is found, except for NUV-filter B15 which shows a variability of ~ 30% (see Fig. 2.9). The gratings are tested for dispersion and spectral transmission in different orders. The results have been summarised in preceding subsections.

Effective Areas

The parameters estimated above are integrated together to estimate the overall effective areas for the various filters (see Figs. 2.23, 2.24, and 2.25) . These are incorporated in the exposure time calculator. The calculator estimates the expected counts/sec for any object, when one provides its spectral energy distribution (or equivalent). This will be used to estimate the exposure times by the users at the time of proposal submission.

Integrated telescopes

Several tests have been done on the assembled telescopes. These tests show the following: a) in photon counting mode, FWHM of the PSF is less than 1.8" for all the filters through the field of 28', b) the effective areas match the estimated (based on the measurements on individual components) values within 25%, c) centres of NUV (FUV) and VIS detectors match within 15" (30"), d) scattered light from out of field sources, at 0.5 deg and at 1 deg., shows no ghosts and the background per 10 square arcsec is attenuated by >19 mag..

Integrated payload

After integration of the two telescopes on a common mount, which interfaces with the S/C, tests were made on alignments and plate scales. These tests show the following: a) for rotations on Yaw and Pitch axes of S/C give shifts in different channels are given by:

dxf = 0.001*dya + 0.29965* dpi & dyf = 0.29965*dya - 0.001*dpi
dxn = 0.15785*dya + 0.2554*dpi & dyn = - 0.2554*dya + 0.15785*dpi
dxv = 0.1627*dya + 0.2400*dpi & dyv = 0.2400*dya - 0.1627*dpi, and
separation between images in VIS are related to those in FUV/NUV by equations:
dxf = 0.85734 dxv - 0.57706 dyv & dyf = 0.57706 dxv + 0.85734 dyv
dxn = 1.03458 dxv - 0.04366 dyv & dyn = - 0.04366 dxv - 1.03458 dyv

where dxv/dxf/dxn are shifts/separations along "x" in VIS/FUV/NUV etc. in pixels Star250, and dya/dpi are rotations of the payload on Yaw/Pitch axis in arcseconds. (Note that each pixel of Star250 corresponds to ~ 75 X 75 micron in the focal plane.)

In orbit calibrations:

This subsection describes the overall goals of the in-orbit calibration and outlines a set of calibration tasks.

A calibration task is the configuration, observation and analysis required to calibrate a specific aspect of the instrument. The primary goal of this calibration is to ensure that the scientific quantities obtained from the

UVIT instrument conform to the requirements set forth by the instrument document. This also needs to fulfill the requirements set forward by the science projects.

UVIT-in orbit calibration is designed to allow automated processing of UVIT data by the pipeline with the goal of producing a calibrated set of images and spectra which can be used for quantitative data analysis in order to achieve the scientific objectives. The activities listed in this document pertain to four types of calibrations. Photometric calibration will yield a conversion of a measured count rates into a broadband flux for any given filter-detector combination. The spectroscopic calibration consists of estimation of wavelength coverage, dispersion and flux calibration. Distortion calibration is the measurement of detector distortion andangular separation across the detector. The relation between a point on the detector based on the image created by the telescopes and the absolute position in the sky will be used to estimate distortion as well as the imgage scale across the field. Photometric point sources will used to find PSF of the instrument for short exposures (which are not affected by drift of the S/C) and for long exposures (which are affected by drift of the S/C, and depend on how well the drift is corrected during the processing on ground). Timing calibrations will also be performed.

The in-orbit tests are performed during the performance verification (PV) phase of ASTROSAT. The total exposure time required for these is approximately one month. The photometric calibration tasks along with the other calibration will be performed in this time. The in-orbit calibration tasks will be performed during the PV phase and repeated at regular intervals to monitor any drifts in
the performance of the system as well as to improve the already estimated parameters. Hence, some of the calibration activities or tasks will be repeated at regular intervals. As per the recommendations of the monitoring team, certain calibration tasks may be included while planning the observing cycles also.

The following table summarises various calibration tasks planned to be taken up during the PV phase and later:

1. Photometric zero-point calibration (FUV, NUV, VISUAL):
2. Photometric standard stars with flux calibrated spectra in the 1300-3500A will be used. The standard star will be observed in the central field in all filters to obtain the flux calibration. Sources which are faint enough to have minimal saturation will be chosen.
3. Secondary photometric calibration (FUV, NUV, VIS):

   The photometric standard stars which are moderately bright be observed in the center and 8 more locations around the center to estimate the variation in zero-point across the field, in all filters.
4. Calibration of the gratings for dispersion and effective area (FUV, NUV):

   Sources such as WR stars or PN with strong emission line spectrum in the UV region will be used to estimate the wavelength coverage and dispersion relation for the two FUV gratings and one NUV grating.
5. Distortion and estimation of image scale across the field: Rich star clusters with UV bright stars and well defined astrometric position will be used. As this depends on the detector, observation in one filter per channel will be obtained.
6. Plate scale and relation between the coordinate system of the detectors and the S/C
7. PSF estimations: The photometric observations will be used to estimate the PSF across the field.
8. Timing calibrations: This will be performed using an appropriately chosen pulsar
9. Estimation of background: These will be estimated using the observations collecetd during the PV phase

Some of these calibrations have been completed and the results are presented below.

Results from In-orbit Calibrations

Photometric Zero Points

Filter	**Name of Filter**	**λ(mean)**	**Δλ**	**EEA**	**Unit Response**	**Zero Point**
FUV						
CaF2 -1	F148W	1480.8	500	8.70	0.309E-14	18.016
CaF2-2	F148Wa	1485.4	500	8.16	0.328E-14	17.994
BaF2	F154W	1540.8	380	9.55	0.355E-14	17.778
Sapphire	F169M	1607.7	290	9.70	0.4392E-14	17.455
Silica	F1172M	1716.5	125	8.62	0.1074E-13	16.342
NUV						
Silica	N242W	2418.2	785	47.21	0.222E-15	19.81
NUV_B13	N245M	2447.1	280	40.01	0.725E-15	18.50
NUV_B4	N263M	2632.2	275	32.52	0.844E-15	18.18
NUVB15	N219M	2195.5	270	6.39	0.525E-14	16.59
NUVN2	N279N	2792.3	90	22.58	0.350E-14	16.50
GALEX						
FUV		1538.6		19.6	0.140E-14	18.82
NUV		2315.7		33.6	0.206E-15	20.08

Except for the filter NUVB15, These Zero Points/Unit Responses are fainter by <20% as compared to those expected from the ground calibrations.

Photometric Flat-field

Some results on photometric flat field are shown in the following figures:

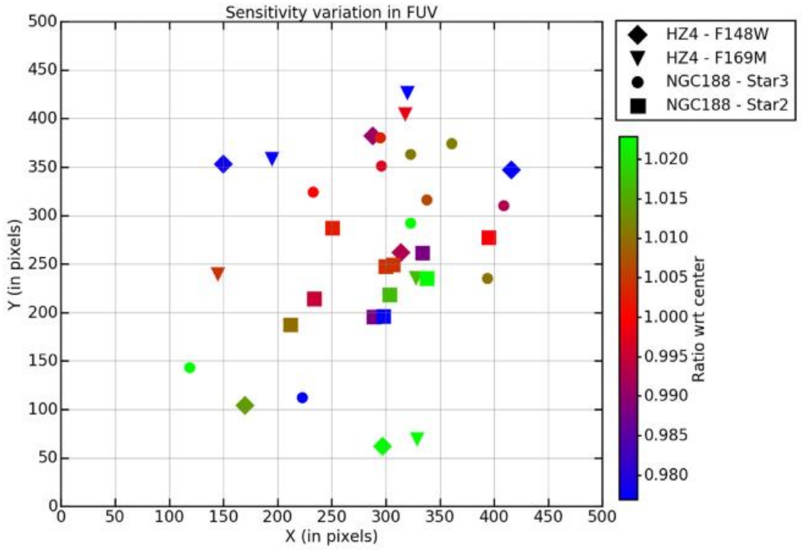

Figure 4. Spatial variation of sensitivity for the FUV channel. We have shown the estimations from the standard star, HZ4, and two stars from the open cluster field, for the filters F148W and F169M. The color code is based on the ratio of the CPS at each position and the CPS of the same source at the center.

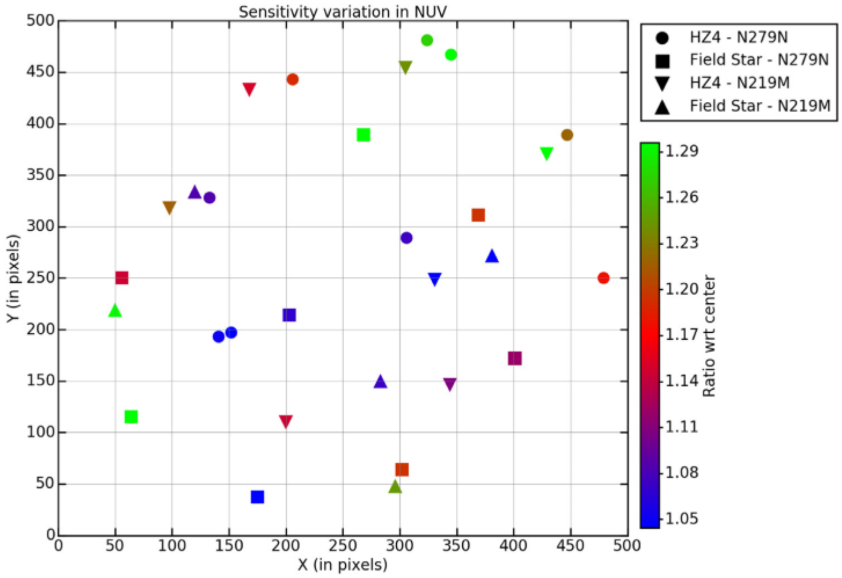

Figure 6. Spatial variation of sensitivity for the NUV channel. We have shown the estimations from the standard star, HZ4, and one more bright star in the field, for the filters N219M and N279N. The color code is based on the ratio of the CPS at each position and the CPS of the same source at the center.

The above two figures are taken from "The Astronomical Journal, 154:128 (14pp), 2017 September https://doi.org/10.3847" © 2017. The American Astronomical Society. All rights reserved. In-orbit Calibrations of the Ultraviolet Imaging Telescope"" and more details can be found there.

Spectroscopic calibrations:

Preliminary results from in-orbit calibrations are presented below.

a) NUV Grating:

Dispersion: 44.5 A/pixel in the first order, where each pixel is equivalent to ~ 3.3”

FWHM of the lines: It is equivalent of ~ 1.8” OR the resolution is ~ 24 A

The effective area as a function of wavelength is shown below; please note that these data have not been corrected for the effects of saturation (due to any overlapping photon events in the frames).

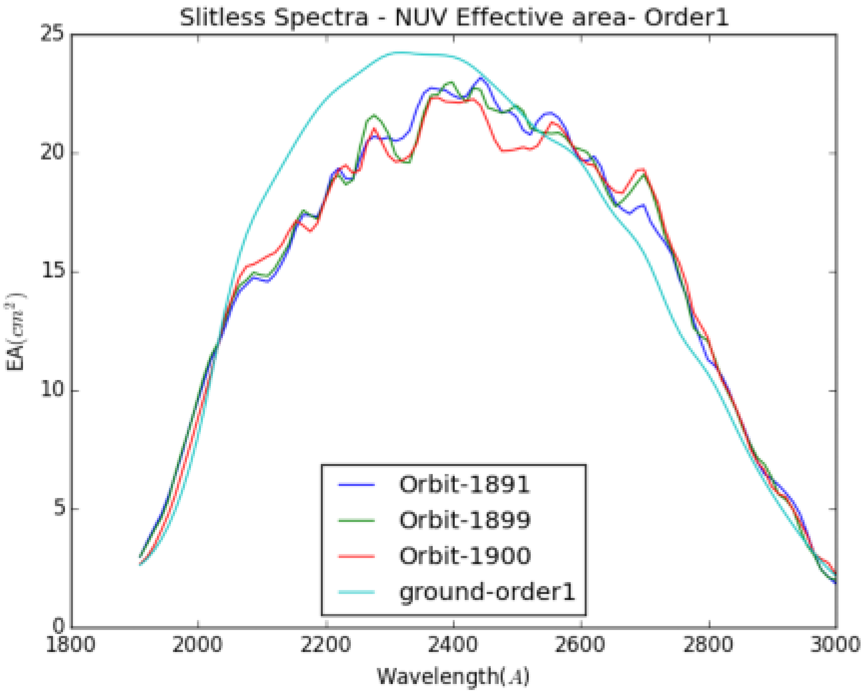

Figure :NUV Effective area (in square cm) from the observed data in the three obits in NUV detector in spectral order 1. Plot in blue, red and green colour is for orbit 1891, 1899,1900 respectively and light green one is derived from the ground calibration data

b) FUV Grating I:

Dispersion: 22.8 A/pixel in the second order, where each pixel is equivalent to ~ 3.3”

FWHM of the lines: It is equivalent of ~ 2.2” OR the resolution is ~ 15 A

The effective area as a function of wavelength is shown below; please note that these data have not been corrected for the effects of saturation (due to any overlapping photon events in the frames).

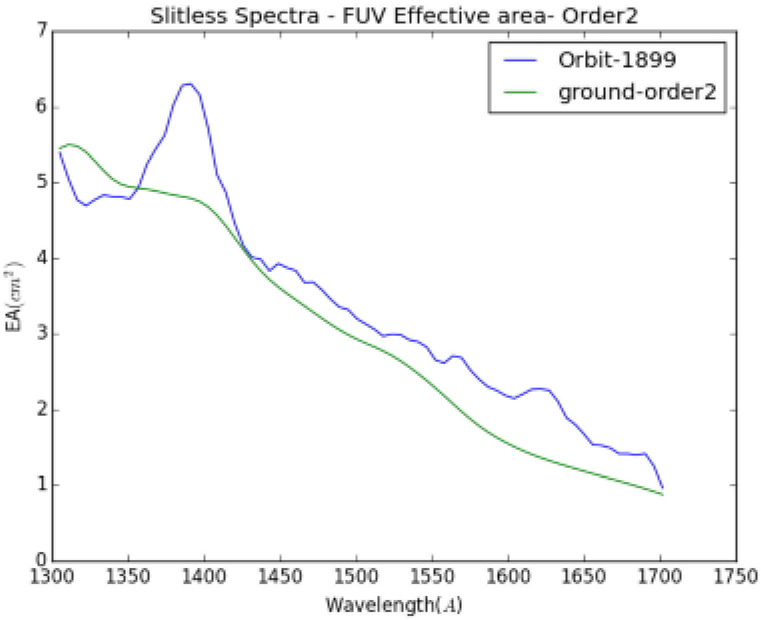

Figure: FUV Effective area from the observed data in FUV detector in spectral order 2. Plot in blue colour is derived from the observation in orbit, and the plot in green is from ground calibration data.

c) FUV Grating II:

Calibrations are not done yet for this grating. Its parameters are expected to be very similar to those of FUV Grating I, and its dispersion is orthogonal to the dispersion of FUV Grating I.

d) PSFs in FUV and NUV:

After correcting for the drift, estimated from the individual exposures in NUV/FUV, the integrated images (over several minutes) give FWHM ~1.3" (as against the specification of 1.8"). The curve of growth is shown in the table below (**taken from ""**The Astronomical Journal, 154:128 (14pp), 2017 September https://doi.org/10.3847

© 2017. The American Astronomical Society. All rights reserved.

In-orbit Calibrations of the Ultraviolet Imaging Telescope""" and more details can be found there.

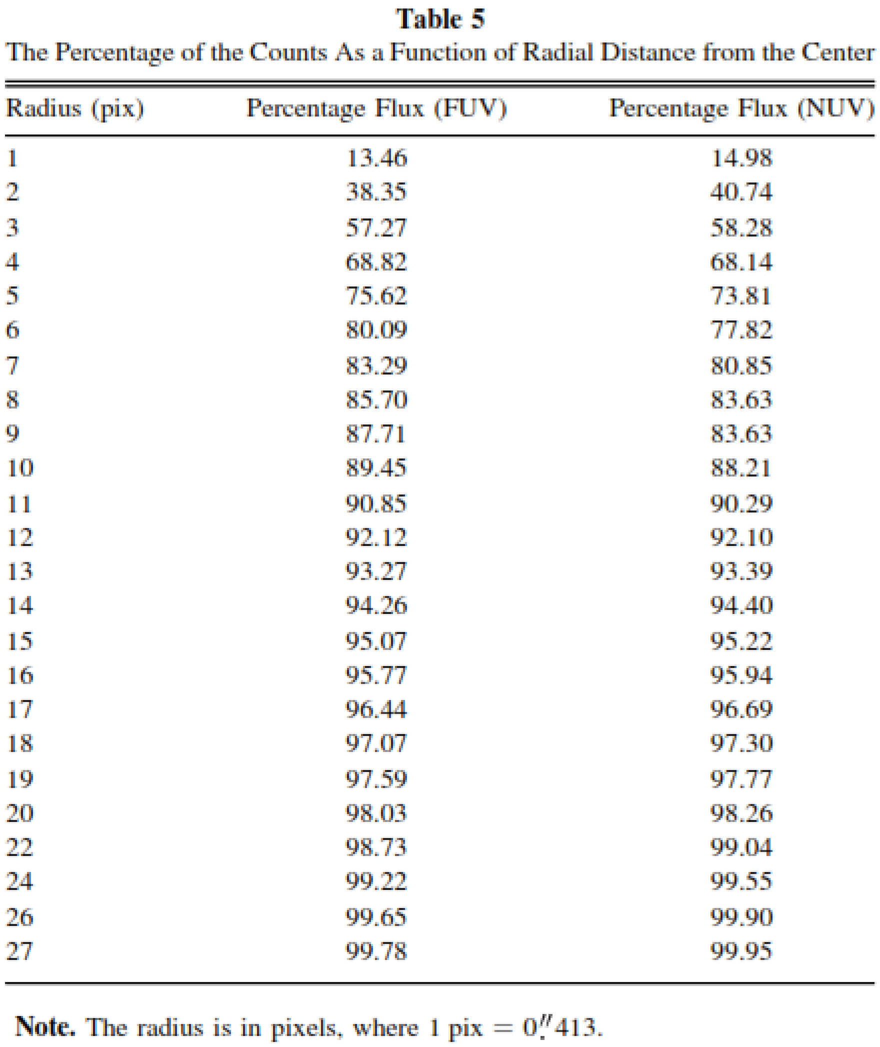

Table 5

The Percentage of the Counts As a Function of Radial Distance from the Center

Radius (pix)	Percentage Flux (FUV)	Percentage Flux (NUV)
1	13.46	14.98
2	38.35	40.74
3	57.27	58.28
4	68.82	68.14
5	75.62	73.81
6	80.09	77.82
7	83.29	80.85
8	85.70	83.63
9	87.71	83.63
10	89.45	88.21
11	90.85	90.29
12	92.12	92.10
13	93.27	93.39
14	94.26	94.40
15	95.07	95.22
16	95.77	95.94
17	96.44	96.69
18	97.07	97.30
19	97.59	97.77
20	98.03	98.26
22	98.73	99.04
24	99.22	99.55
26	99.65	99.90
27	99.78	99.95

Note. The radius is in pixels, where 1 pix = $0''.413$.

e) Background:

Shower-like background is seen in ~ 3 frames every second due to interaction of the cosmic-rays. The total background due to these is ~ 150 events/s

f) Coordinate Transformations:

The relation between the coordinate systems of the detectors and the S/C are found as below:

```
Inter-channel transformations
    VIS to NUV :

   dXn =     1.016306 * dXv - 0.05093 * dYv
   dYn = -   0.05093 * dXv -  1.016306 * dYv
```

```
        FUV to VIS :

       dXf =  0.83867 * dXv - 0.58435 * dYv
       dYf =  0.58435 * dXv +  0.83867 * dYv



 Detector-Spacecraft relations :

        VIS :

         dXv = 0.1627 * d_YAW + 0.2400 * d_PITCH
         dYv = 0.2400 * d_YAW - 0.1627 * d_PITCH


        NUV :

         dXn =   0.15313 * d_YAW  + 0.2522   * d_PITCH
         dYn = - 0.2522  * d_YAW  + 0.15313 * d_PITCH


        FUV :

         dXf = -0.0037911   * d_YAW  + 0.29635469  * d_PITCH
         dYf =  0.29635469 * d_YAW  + 0.0037911   * d_PITCH

Here, "v/n/f" refer to VIS/NUV/FUV detector.
```

Limits on Brightness for Observations with UVIT

1. **Introduction**

UVIT uses intensified imagers which can suffer permanent damage if exposed to excessive flux of photons. Therefore, it is required that observations are only allowed for those fields which have objects below defined levels of brightness in the field and its close neighbourhood. While a detected photon rate of 5000/s can be considered as a safe upper-limit for any point source is the field of the detectors, there is another considerations in defining a practical limit on the rate. The hardware has a provision for safety which initiates "BOD-trigger" if an excessively bright object (defined by some parameters) is in the field; BOD-trigger initiates actions which bring all the detectors to OFF condition.

2. **Recommended Limits on Count Rates**

2.1 The field and its neighbourhood

a) The field of view for UVIT is ~ 28' in diameter. However, the pointing error can be up to 3' and there could be some drift during the exposure. Therefore, for avoidance of bright sources we define the field as 40' diameter.

b) Scattered light from sources near edges of the field can reach the detector. For a source 30' away from the axis, ~ 0.5% of light can reach the detector- most of which would fall in one half of the detector. For sources at

60’ from the axis, ~ 0.1% of light can reach the detector. *Direct tests with the telescopes show that < 0.5% of the light reaches the detector for sources at 30’ and 60’ from the centre, and that there are no ghost images in the field. We take the value of 0.5% for defining limits on the brightness.*

2.2 Count Rates in the Field

The following upper limits on count rates are recommended for any point source, or any 100 sq arcsec part of an extended source, in a field of 40’ diameter around the centre: a) for VIS-CPU: 4800/s (in integration mode with an intensification ~ 1/20 of that used for photon-counting), b) for NUV-CPU: 1500/s (in Photon Counting Mode) and c) for FUV-CPU: 1500/s(Photon Counting Mode) .

The above limits are to be followed for most of the observations, but in special cases it may be possible to allow exposures to brighter sources with a suitable protocol.

2.3 Count rates in neighbourhood of the fields

A total rate of 10^5/s over the full face of the detector can be considered safe in photon-counting mode. Therefore, a source with count rate < 2 X 10^7/s can be allowed within 60’ (but beyond 20’) of the axis for observations with NUV and FUV CPUs. For the VIS-CPU, used in integration mode with a lower gain (by a factor ~10), a count rate of < 10 X (2 X 10^7)/s can be allowed.

Possibility of the ghosts at certain angles cannot be ruled out yet, and in the initial periods of the mission it would be best to keep the limit to a smaller number, e.g. 10^6/s, and look for possible ghosts.

>>>>>>>>>>>>>>>>>>>>>>>>>>>>>>>>>>>

Chapter 3

Soft X-ray Telescope

Soft X-ray imaging Telescope (SXT) onboard AstroSat is sensitive to soft X-rays in the energy range of 0.3 – 8 keV. X-rays in this energy range are amenable to focusing and will lead to: a) nearly 1000 times better sensitivity over non-focusing instruments of similar areas making over 10,000 sources detectable; b) separation of confusing sources; c) arc min imaging; d) spatially resolved spectroscopy; and e) variability studies.

SXT covers a very important energy range of the broadband spectrum observed with AstroSat, and will be able to investigate the following scientific problems.

1. Resolving the K line emission from Si, S, Ar, Ca and Fe in hot thermal coronal plasmas, as well as fluorescent line emission from these elements in the medium photo-ionized by strong X-ray continuum in accretion powered X-ray sources (neutron stars, stellar mass black-holes, supermassive black-holes etc.).
2. Carrying out spectroscopy of hot thin plasmas in galaxies, clusters of galaxies, nuclei of active galaxies, quasars, supernova remnants and stellar coronae.
3. Studying the physics of shocks and accretion disks, coronae, photo-ionized regions and their density, temperature, ionization degree, and elemental abundance.
4. Studying low energy absorption and the nature of absorbers, for example, whether these are cold (neutral) or warm (ionized).
5. Studying soft X-ray excesses due to a blackbody emission in AGNs, and in binary X-ray pulsars in conjunction with other higher energy X-ray instruments.
6. Carrying out Spatially resolved spectroscopy of Supernova Remnants and Clusters of galaxies.
7. Carrying out simultaneous wide-band spectral studies and time-resolved spectra of thermal as well as non-thermal plasmas in the universe using the unprecedented combination with sensitive hard X-ray detectors.

Telescope

The telescope consists of a tubular structure housing the assembly of X-ray reflecting mirrors and other components. There is a “Charge Coupled Device” (CCD) camera at the common focus of all the mirrors in order to image the cosmic sources.

Basic Components

The basic components of the telescope are given below (see Fig. 3.1).

a) A Mirror Assembly.

b) A Focal Plane Camera Assembly housing a cooled CCD.

c) A deployable cover/door at the top end of the telescope that covers the optical elements on the ground and protects them from contamination. This was deployed ~2 weeks after launch, in a one-time operation, and is perched at an angle of 256°.

d) A "Thermal Baffle" placed between the mirror assembly and the telescope door. All parts are made of anodized aluminum alloy 6061 T6. The function of the thermal baffle is to protect the telescope from the Sun, and to provide a base for mounting the heaters to maintain the optics within a certain specified range of temperatures, and to block the unwanted area of the optics. The sun avoidance angle with the thermal baffle is ~45^o.

e) A "Forward tube" made up of Composite Fiber Reinforcement Plastic (CFRP). The Forward tube extends from the bottom of the "Top Lid" and it covers the thermal baffle assembly and 1α section (see below) of the Optics assembly.

f) A metallic ring (Ring 1) provides an interface between the Rear tube 1 and the middle flange of the optics from the bottom side. Another ring (Ring 2) provides an interface between the Forward tube and the Rear tube 1 from the top size.

g) Rear tube-1 made up of CFRP is a hollow cylinder of diameter 343 mm ID and 347.8 mm OD and extends from Ring-1 to the "Deck Interface Ring" (DIR). It houses 3α (see below) optics while the Forward tube houses the 1α assembly (see below).

h) "Deck Interface Ring" (DIR) is made up of Al alloy 6061 and is used to assemble rear tube-1 and rear tube-2 of the telescope. DIR has 9 nos. of holes of size M8 to provide interface between the payload and the top deck of the satellite.

i) Rear tube-2 made up of CFRP is a hollow stepped cylinder with a top portion thicker than the bottom portion to provide stiffness. Rear tube-2 extends from the DIR to the CCD interface ring.

j) CCD interface ring is provided to align the CCD Camera with the Rear tube-2 tubular structure to the desired accuracy. This is made up of aluminum alloy 6061.

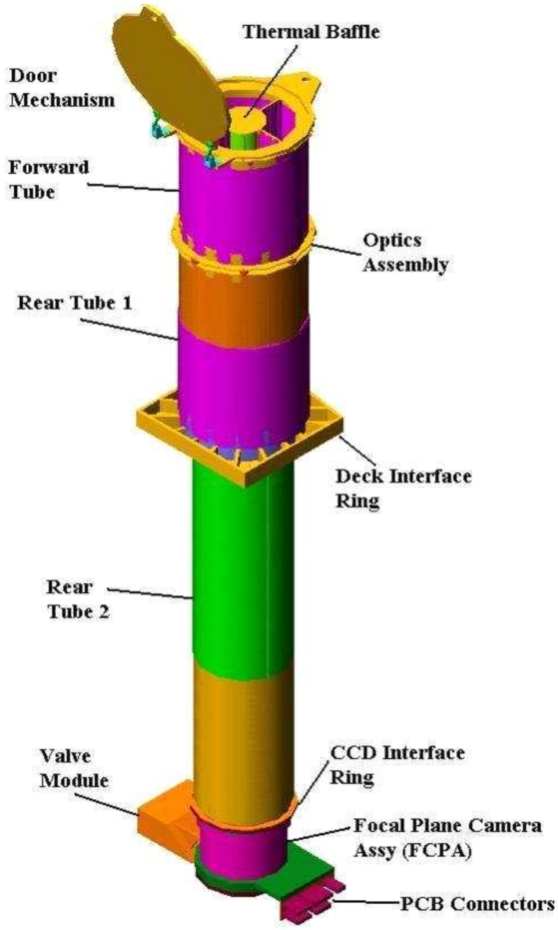

Figure 3.1: Left: Structure and various components of the Soft X-ray Telescope from outside (simulated picture). Top: The optical modules with gold-coated mirrors (upper: 1α; lower: 3α; actual photo).

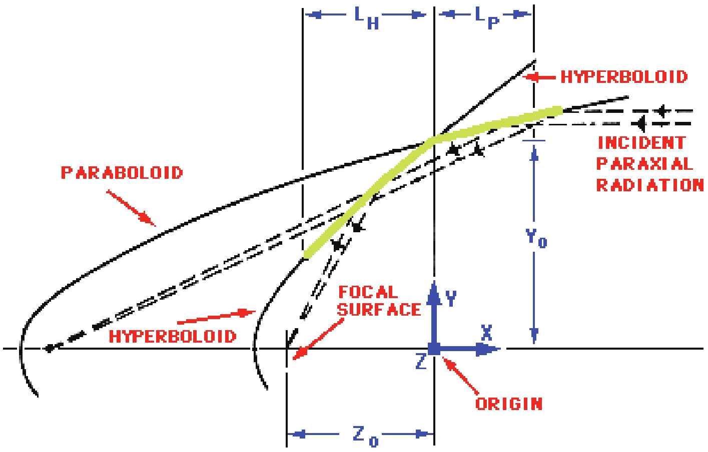

Figure 3.2: The principle of the Wolter I optics using ray diagram. The green lines show the conical approximations of the paraboloidal and hyperboloidal mirrors.

The Mirror Assembly for X-ray reflection

The mirror assembly of the X-ray telescope in the SXT consists of a set of coaxial and con-focal shells of conical mirrors approximating paraboloidal and hyperboloidal shapes and arranged behind each other. This geometrical arrangement is known as Wolter I optics (Fig. 3.2). X-rays are first reflected by an internally reflecting paraboloidal (1α section) mirror and then reflected to the prime focus of the telescope by an internally reflecting hyperboloid (3α section) mirror. At grazing incidence, the active region of the mirror is just a thin annulus giving a small collecting area even for a large diameter mirror. Thus nesting of Wolter I shells is incorporated to improve the filling factor of the circle defined by the outermost shell. Higher nesting is achieved by using shells made of very thin foils but figured in a conical approximation to Wolter I optics. SXT has 40 complete shells of mirrors assembled quadrants wise (320 mirrors) for 1α and 3α mirrors (Fig. 3.1). The focal length of the telescope is 2000 mm, constrained by the available space in the launch vehicle flaring. Each mirror is made of aluminum (thickness ~0.2 mm) covered with gold on the reflecting side. The length of each mirror is 100 mm. The radius of the outermost shell is 130 mm, while that of the innermost shell is 65 mm. The on-axis FWHM and half-power diameter (HPD) of the point spread function (PSF) in the focal plane is ~2' and ~10' respectively. The on-axis effective area of the telescope is about 90 cm^2 at 1.5 keV (Fig. 3.3).

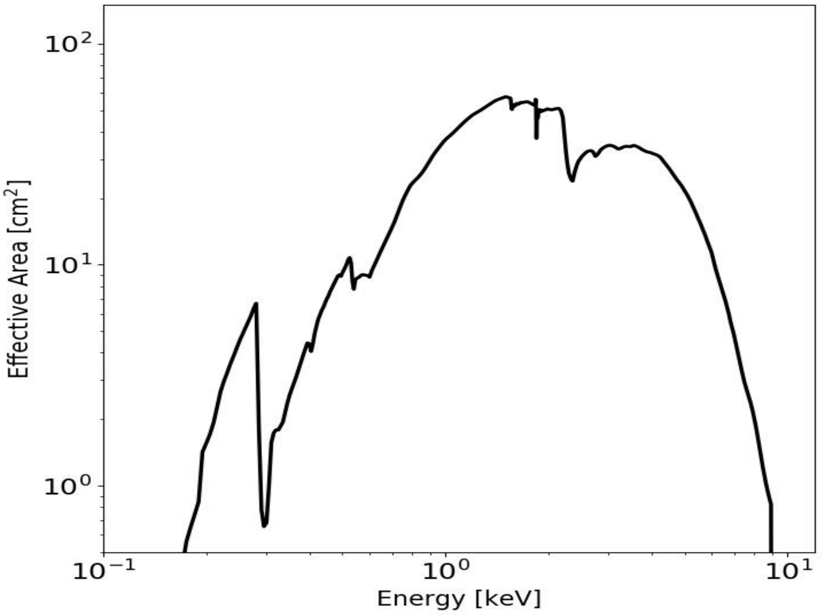

Figure 3.3: Telescope effective area (including CCD Quantum Efficiency (isolated and bi-pixel events 1-4) and the absorption by the optical blocking filter as measured) vs. energy for on-axis.

Focal Plane Camera Assembly

The primary instrument in the Focal Plane Camera Assembly (FPCA; see Fig. 3.4) of the SXT is a special CCD, which is the focal plane imager. The health and the operational conditions of the CCD require vacuum, low temperature and protection from the optical light and energetic protons. Therefore, components such as thermo-electric cooler (TEC), optical blocking filter, proton shield, etc. have been included in FPCA. The operation of the CCD also requires the processing electronics, and the calibration of the CCD + processing electronics requires calibration sources.

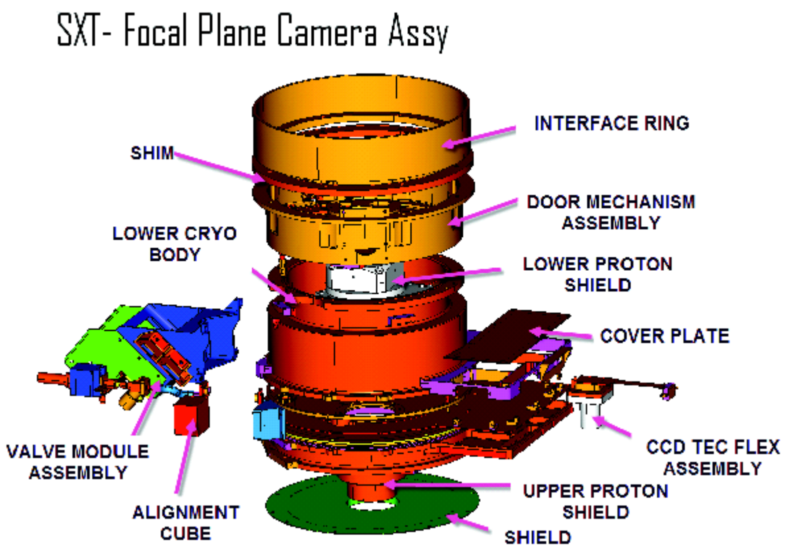

Figure 3.4: Focal Plane Camera Assembly (FPCA) and its components.

Focal Plane Camera Assembly Devices and Components

(i) Charge Coupled Device CCD-22:

It is a MOS device built by the e2V Technologies Inc., UK, for the European Photon Imaging Camera (EPIC) onboard the XMM-Newton observatory and supplied to the University of Leicester and has the following characteristics (also see Fig 3.5):

(a) A three-phase frame transfer.

(b) Open electrode structure for useful band pass of 0.2 to 10 keV.

(c) Operating area of 610 × 602 array of 40 micron by 40 micron pixels including over-scan.

(d) The storage region is a 600 × 602 array of 38 x 12 micron pitch.

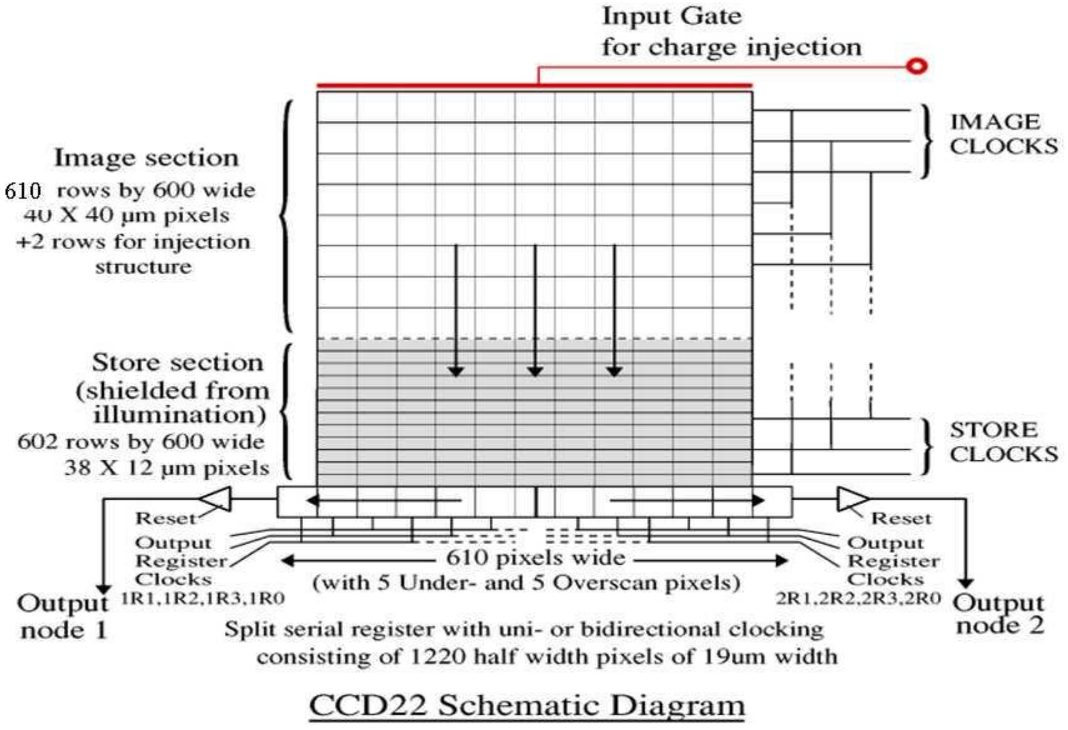

Figure 3.5: Schematic Diagram of the CCD22.

(ii)Calibration sources:
Four individual ^{55}Fe radioactive calibration sources are provided in the camera for in-flight calibration at energies of ~5.9keV (Mn). These illuminate the corners of the CCD outside the Field Of View (FOV). A fifth source under the door facing the CCD is no longer available after the deployment of the door. See Figure 3.6.

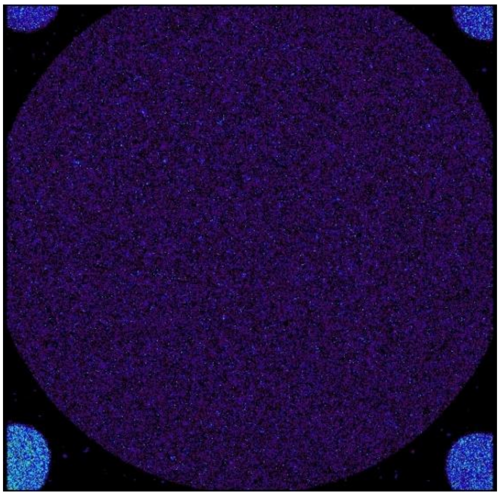

Figure 3.6: The CCD illuminated by 4 internal calibration sources, shown at corners.

(iii) Optical Blocking Filter:
A thin filter is installed in front of the CCD to block visible light. The filter consists of a single fixed polyimide film 1840 A° thick coated with 488 A° of Aluminum on one side. The typical optical transmission of the filter is less than 5×10^{-3} (similar to the XMM-Newton thin filter).The filter design provides ~ 7 magnitude of optical extinction over the visible band. For the SWIFT XRT with a PSF of ~15" a 6th magnitude star gives an optical loading of ~ few e^- per pixel, at which point the quality of the X-ray data begins to be affected. For the SXT with a ~7-8 times larger PSF and a 2 times larger (angular) pixel the safe optical limit should be closer to a ~4 magnitude star. This limit is best set using a bright non-X-ray emitting star. The X-ray transmission of the filter is shown in Fig. 3.7.

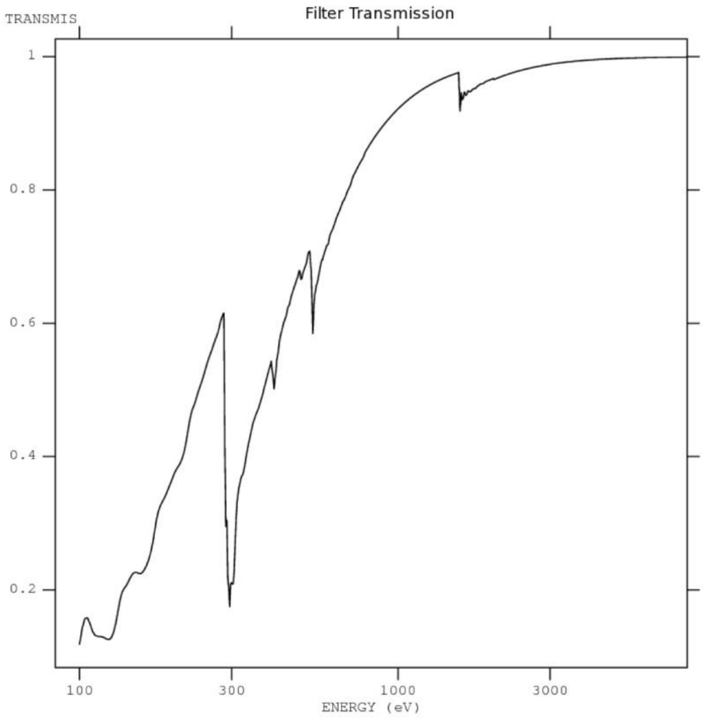

Figure 3.7: The transmission of X-rays through the optical blocking filter.

(iii) Operating Temperature of the CCD:
The X-ray CCD detector is cooled to 191^{o}K (-82^o C) by a thermo-electric cooler (TEC) and a radiator assembly during its operation for low dark current and to reduce sensitivity to radiation damage. The TEC is coupled to a cold finger connected to a “Heat Pipe” unit which is connected to a radiator plate designed by ISRO for effective heat dissipation and which provides a maximum temperature of −40°C at the junction between the heat pipe and the camera cryostat.

(iv) Proton Shield:
The camera is provided with a proton shield to minimize any damage to the device due to energetic protons. The degradation of energy resolution is, therefore expected to be contained during the 5 years lifetime of the AstroSat mission. Due to the orbit of the AstroSat being more benign than the orbit of SWIFT, the mass and size of the proton shield was significantly reduced from the original SWIFT design.

(vi) Readout Nodes:
Provision has been made for readout from either left node or the right node using node with two individual pre-amplifiers.

CCD Quantum Efficiency (QE) Curves

The flight device has been calibrated across the energy range giving the measured QE values for iso events, for events up to 4 pixels in size, and for “all” events, i.e. including those with 5 or more active pixels. The results of these calibration tests are shown in Fig. 3.8.

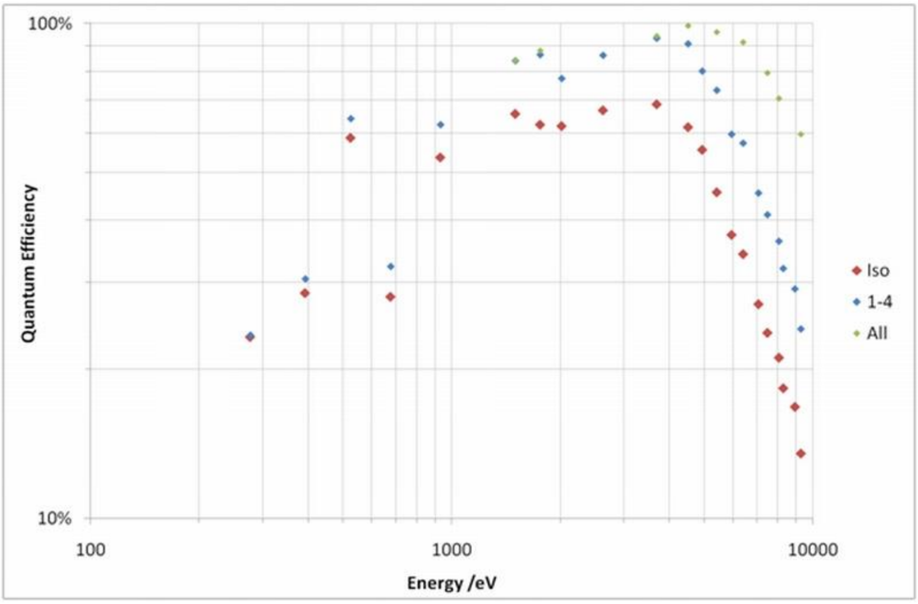

Figure 3.8: CCD Quantum Efficiency points (refer to the subsection "CCD Quantum Efficiency Curves”).

The Energy Resolution

The energy resolutions estimated from the calibration data given below.

Line ID and Energy E (eV)	Resolution (ΔE) (FWHM in eV)	Resolution (%ge)
Al –Fl : 1487	90 ± 8	6.0 ± 0.5
Si –K : 1740	92 ± 6	5.1± 0.3
Cl –F : 2621	104 ± 5	4.0 ± 0.2
Mn-Kαesc : 4155	120 ± 5	2.0± 0.15
Ti –F : 4511	126 ± 6	2.8 ± 0.15
Mn-Kβesc : 4750	128 ± 7	2.7 ± 0.15
Mn-Kα : 5895	136± 8	2.3± 0.15
Mn- Kβ : 6490	145± 10	2.1± 0.15

Charge Transfer Inefficiency (CTI) and Pile-up effects

The Charge Transfer Inefficiency (CTI) has been measured along both the serial and parallel readouts using the four corner sources. The serial and parallel CTIs thus measured are shown as a function of energy in Fig. 3.9.

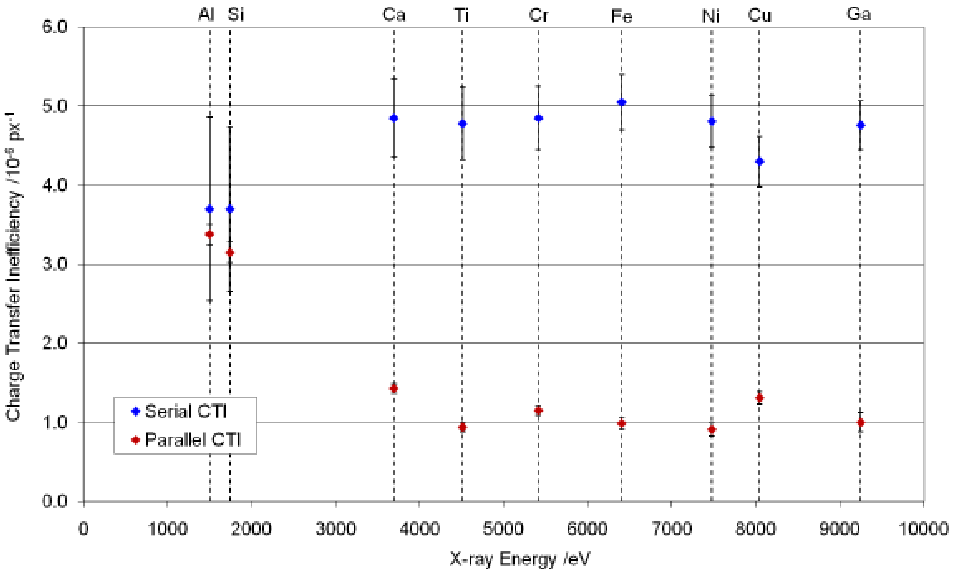

Figure 7. Serial and parallel charge transfer inefficiencies as a function of x-ray energy.

Figure 3.9: The serial and parallel CTI as functions of energy.

The CCD camera door is always open and remains open during the data readout. Therefore, if the source is too strong or the PSF is too sharp then multiple photons can fall on the same pixel during the 2.4 s that it takes to readout the CCD, leading to a pile-up and affecting spectra, light curves and images. The amount of pile-up depends on the PSF of the telescope and will need to be corrected for when the source count rate at the maximum of the PSF becomes ~0.5 cts/pixel/frame. The measurements of the PSF suggest that it will not become an issue in the PC mode for sources fainter than ~200 mCrab. For *Chandra, XMM-Newton* and *Swift* in imaging modes pile-up occurs for sources of intensity ~0.1, 1 and 5 mCrab respectively. *The pile-up effect depends on the sharpness of the PSF and the intensity of the source. The exact measurement of this effect is complicated due to corrections for the attitude variations that are still being implemented, and it will be provided soon.* At present, if a source is producing (or expected to produce) < 40 counts/s, it is safe to assume no pile-up for the PC mode. This limiting count rate will be ~8.6 times larger in the FW mode. Our current analysis shows that in order to get rid of pile-up for ultra-bright sources like Crab, Cyg X-1 etc., a 1 arcmin central removal of the PSF is enough. However, a more rigorous study of pile-up using the most recent analysis procedure will be discussed in the next version of the handbook.

Observational Characteristics

Detector:	e2V CCD-22.
Pixel Size:	40µm × 40µm.
Pixel Scale:	4.12” per pixel.
Useful Image Area:	600 pixel × 600 pixel.
Field of View:	~40’.
PSF:	2.0' FWHM. 10.0' HPD.
Position accuracy:	2.0’
Energy Range:	0.3-8keV.
Energy Resolution:	90 eV at 1.5 keV. 136 eV at 5.9 keV.
Time resolution:	~ 2.4 s (full frame)

~ 0.278 s (150x150 centered pixel frame)

Effective Area: ~90 cm^2 at 1.5 keV.

Sensitivity (obs. time): ~10^{-13} ergs cm^{-2} s^{-1} (5 σ) (20000 s)

Data Modes and Telemetry

Data from the SXT CCD are stored on-board, and then sent to the ground station once in each orbit around the Earth. The SXT on-board memory quota is 280 Megabytes per orbit (~ 98 minutes). This puts serious constraints on the data modes and how the data are packaged. There are four data modes and one separate mode for only housekeeping. In each mode, data are packed in 2 Kbyte (2K) segments. So the SXT memory per orbit is filled with approximately 143360 2K blocks.

The various data modes are "Photon Counting" (PC) mode, "Fast Windowed Photon Counting" (FW) mode, "Bias Map" (BM) mode and "Calibration" (Cal) mode (CM). There is also the "House Keeping" (HK) mode for health parameters of the electronics system. In the PC mode, data from the entire CCD (i.e., 600 X 600 pixels) are collected, provided these are above a specified threshold energy (set through a tele-command by the SXT team and it can be between 100 - 200 eV). Currently the default value set is 105 eV that is 4σ above the noise peak. *It is, however, recommended that low energy threshold to be used during analysis should be >=200 eV*. Moreover, data from a maximum of 36000 pixels only can be transmitted in this mode. The read-out time of this mode is ~2.4 s. In the FW mode, a 150 X 150 pixel window is used in the center of the CCD. The read-out time of this mode is ~278 ms. Data in the FW mode are also thresholded as in the PC mode. The Cal and bias modes are used to check the calibration of SXT and the zero point for the noise level. The read-out time of the Cal mode is ~2.4 s. Data from 4 corner windows of the CCD with a size of 80x80 pixels (under 4 X-ray radioactive sources) and a central window with a size of 100x100 pixels are transmitted with *zero threshold in the CM*. BM mode is a separate mode in which the entire CCD frame is sent with zero threshold. Incrementally addressed 60 rows per CCD frame along with their co-ordinates are sent in this mode. On the ground, these rows of each incrementally addressed CCD frame are mapped to generate an individual CCD frame. It takes 24 seconds of data to generate one completely mapped CCD frame. The HK mode is operated only when there is a failure of both LBT telemetry channels (main and redundant). When HK mode data command is uploaded, LBT data information in the form of HK data are sent in 2K data package. Hence only one frame will be generated and pushed in currently operating mode data package. Spectral information is available under all 4 modes: PC, FW, CM and BM.

Data (Level 1) in each mode are packaged in 2K blocks. However, the content of a 2K block is not the same for all the modes. For the PC and FW modes (i.e., the science data), only the channel number above the pre-selected threshold is stored in the 2K block along with the pixel coordinate and the CCD frame identification. These data are stored in the 15th to 2042nd bytes of the total of 2048 bytes of a 2K block. Three bytes are required to store each of (a) CCD frame identification, (b) CCD row number of the pixel and threshold value and (c) CCD column number of the pixel and the channel number. The bytes 1-14 (header) and 2043-2048 (footer) store the 2K block number, mode information, on-board time, window location and numbers to check the validity of the 2K block.

Operation Procedure

Normal operations began after the SXT door was opened. The CCD is currently maintaining its operational temperature with an accuracy of ±2 degs. SXT is pointed towards a celestial source only after all the observational constraints are met, and the FPCA is normally operated in the PC mode with full CCD readout unless specified otherwise. The calibration data from the four corner point sources are part of the observations but unlike in the CM these have a threshold already applied. Thus normal data have full energy resolution and time resolution of 2.4 sec.

On-board Electronics

The SXT electronics box consists of ten cards of circuits (EL-01 to -08, EL-3A, Motherboard), including three Field Programmable Gate Arrays (FPGAs). The science data and the bias map data from the CCD are passed on to the EL-03, where the analog to digital conversion happens. The science data are then stored in a memory (M1) in EL-05 via the 1st FPGA (EL-04). This memory has two portions: upper and lower. When the 1st FPGA stores the data in the upper memory, the 2nd FPGA (EL-06) takes the previous set of data from the lower portion of memory M1. Next time, when the 1st FPGA stores in the lower portion of memory M1, the 2nd FPGA takes from the upper portion of memory M1. This way data are continuously passed on from the 1st FPGA to the 2nd FPGA. For bias map generation, separate dedicated mode can be enabled which sends the entire CCD frame in ~24 seconds. In the 2nd FPGA, the data are packaged in 2 Kbyte blocks (as mentioned in the previous section), and passed on to the 3rd FPGA (EL-07). Here the data are sent to the satellite memory (allocated for SXT) via high bit rate telemetry (HBT; rate is 4 MHz). The housekeeping (HK) data from the FPCA are passed on to the 3rd FPGA via EL-3A, and eventually sent to the satellite memory via low bit rate telemetry (LBT; rate is 40 kHz). The power from the satellite interface is supplied to various cards via the relay card (EL-02) and the DC-DC tray (EL-01). The input of the DC-DC tray is between 28 V and 42 V, and its output to each card is a regulated voltage. The tele-commands from the satellite interface are passed on to the various cards, and eventually to the FPCA via EL-3A and EL-02.

Observational Constraints

There are several pointing constraints on the SXT observations, primarily to protect the CCD, the optical blocking filter above the CCD, and the mirror coating. The most important one is the Sun avoidance angle (> 45 degree) and is absolutely essential for the safety of the SXT. The other constraints that can affect the data quality are the Earth limb / bright Earth avoidance angle, the RAM direction avoidance angle and the Moon avoidance angle. The RAM avoidance of >12 degree is applied by the mission operations for all the observations as it can also affect the mirrors. The bright Earth avoidance angle of >110 degree is used in the SXT pipeline while converting level1 data to level 2 data products.

In-flight Performance

The first six months of observations with AstroSat were dedicated for performance verification (PV) observations, followed by a six-month long guaranteed time (GT) observation phase. In a typical orbit, parts of the SXT data are not usable due to SAA passage, eclipse of the source by the Earth and by the bright Earth viewing that floods the available memory allocation. The net observing efficiency of the SXT varies from source to source but on the average it is about 25%.

The SXT has observed many X-ray sources including PKS 2155-304, Tycho SNR, 1E 0102-72.3 - an SNR, AB Dor - an active sun-like star, A1795 - a cluster of galaxies, and other AGN, X-ray binaries, etc. An example of Tycho spectrum is given in Fig. 3.10. A comparison of the 1E 0102-72.3 spectrum with the IACHEC model is also shown in Fig. 3.11. The spectral comparison with IACHEC model confirms the spectral calibration of SXT. SXT was pointed such that 1E 0102.2-7219 and PKS 2155-304 were incident on different parts of the CCD to determine the bore-sight of the telescope and the vignetting in the SXT at different off-axis angles. Since PKS 2155-304 had shown strong variability during our monitoring, we have mostly relied on the use of the supernova remnant 1E 0102.2-7219 in the Small Magellanic cloud which, however, required long observations, as the source is very weak in the SXT. This source emits mostly soft X-rays and is seen in 0.3 - 3 keV energy band. The results from these observations showed that the bore sight of the SXT is close to center of the foV at the CCD detector coordinates X=302±7 and Y=285±7 in pixels. The vignetting of the telescope or the projected area as a function of off-axis angle was also determined.

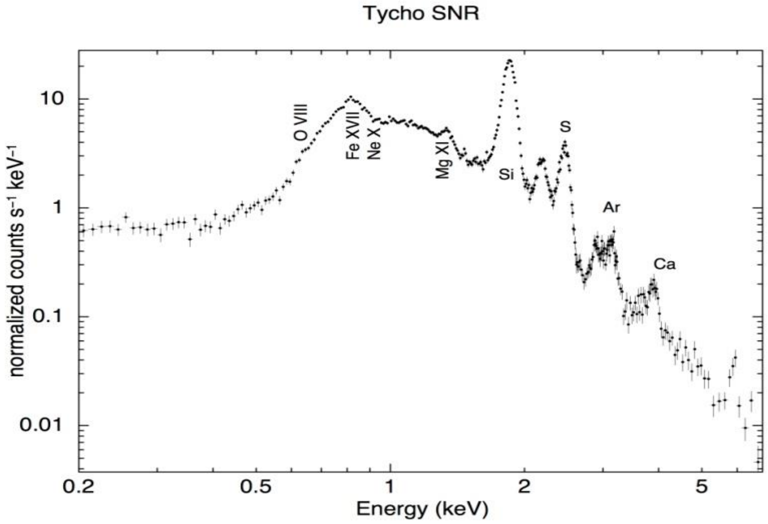

Figure 3.10: The SXT sprectrum of Tycho.

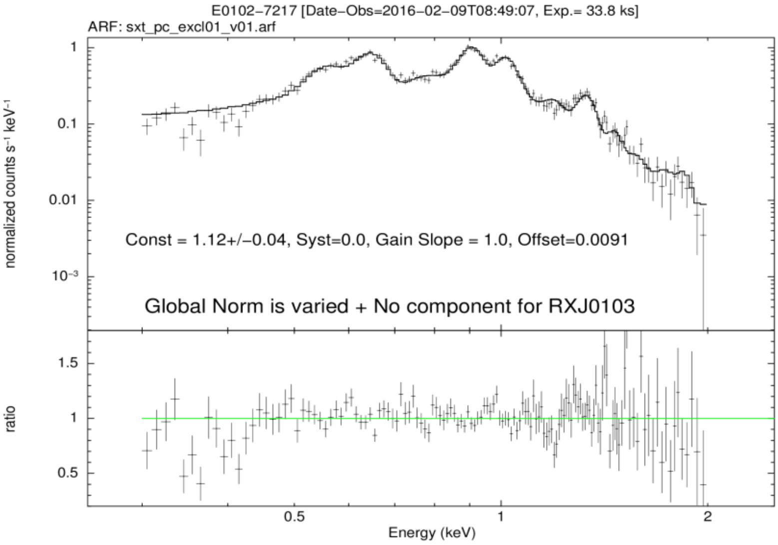

Figure 3.11: The X-ray spectrum of 1E0102-72.3 as fitted with the IACHEC model derived from several X-ray observatories carrying a CCD camera in the focal plane of a telescope. The SXT spectrum was extracted from a radius of 10 arcmin. No significant contributions from the closest (<2arcm) XRB are noticed.

The on-axis point spread function (PSF) in the focal plane is well characterized by a double King function (see Fig. 3.12). The two King functions have core radii of 54±8 and 680 (-200, +400) arcsec respectively with the broader King function having ~8% of the intensity compared to the narrower King function. The broader King model is indicative of the misalignment and the scattering in the mirrors. The half light (intensity) radius is ~70 arcsec, the half encircled energy radius is ~7-8 arcmin. Care must be taken to include as much of the encircled energy as possible while extracting a spectrum, and then use the corresponding response for the telescope area function from those provided. For very bright sources, the user may have to include a radius as large as 18 arcmins to get all the photons and then use background from a deep field with no detectable objects. The deep field background images to be used for image analysis of extended sources like clusters etc. During the last two years of AstroSat, the CCD gain of SXT has been changed by 30-40 eV and the users are requested to apply it externally (using gain command) when fitting the spectrum. One should confirm it by matching the RMF (by shifting the gain) with gold absorption edge, seen clearly in the spectral data.

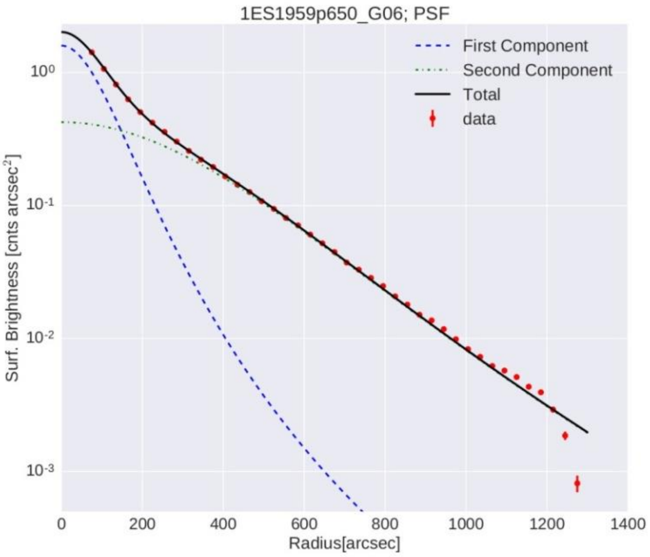

Figure 3.12: The point spread function for on-axis SXT observations of the blazar 1ES 1959+650 (exposure: 71 ks; 0.3-7.0 keV) made by using equal distance method. The X-axis shows the distance from the bore sight (arc sec), whereas, Y-axis gives the normalized counts. The best-fit double King function model, as well as the two King function components, are shown.

A description of the in-flight performance can be found in

Singh, K. P., et al., “Soft X-ray Focusing Telescope aboard AstroSat: Early Results”, Current Science, in press, 2017.

Singh, K. P., et al., “The Soft X-Ray Focusing Telescope aboard AstroSat and its Post-launch Scientific Capabilities”, JAA, in press, 2017.

Singh, K. P., et al., “In-orbit performance of SXT aboard AstroSat”, Proceedings of the SPIE, 9905, 2016.

The numbers corresponding to the most recent pipeline updates (coordinator tool) are being worked out - a preliminary report can be obtained from the SXT-POC on request (email: astrosat_sxt@tifr.res.in).

Data Analysis Tools

The raw data obtained from the AstroSat are processed and made available in required format for use. The data analysis software has been developed for the purpose of processing data at different data Levels as described below.

Level-0 data: The Level-0 data are considered as instrument-wise raw data in binary format along with its associated auxiliary data, which are segregated from all instrument combined raw-data obtained through telemetry. These data are very mission specific and hence are not available for public use.

Level-1 data: These data are obtained by applying various transformations on Level-0 data and are stored in the FITS format. The data will be available for public use after some initial lock-in period. The PI of the proposal will be given access to the data at the earliest possible time after a pre-processing to level-2 and a check out by the SXT-POC. Level-1 data directory would contain science data file, time calibration file, attitude file, orbit-file, level-1 MKF file and house-keeping data file.

Level-2 data: These data contain standard science products obtained from processing of Level-1 data for a default set of parameters and would be available for public use. The level-2 software offers user interface for proper selection of parameters and desired analysis of Level-1 data. One can have selections of these parameters depending on science objectives.

The Level-1 to Level-2 data processing software:

Pipeline data analysis software requires Level-1 data files and calibration data files from SXT Calibration database, CALDB as input for its execution. The data processing steps involve, event extraction using SXTEVTGEN, time tagging of events using SXTTIMETAG, coordinate transformation from raw to detector and XY co-ordinates using SXTCOORD, bias subtraction and adjustment using SXTBIASSUB and SXTBIASADJ, flagging of bad pixels and calibration source events using SXTFLAGPIX, events grading and PHA construction for each event using SXTEVTGRADE, search for hot and flicker pixels using SXTHOTPIX and then carrying out PHA to PI conversion of events using SXTCALCIPI. The data processing thus generates an unfiltered event file. The tool SXTFILTER is used to create Level-2 MKF file. To generate cleaned event file, data screening is done using tool SXTSCREEN on unfiltered event file utilizing Level-2 MKF file, HK and event range files from calibration database. Basic Level_2 data products such as image, light curve and spectrum are generated utilizing clean event file by product generation tool, SXTPRODUCTS designed based on XSELECT interface from HEASARC (NASA).

The Level-2 data products so generated using pipeline processing are used for scientific analysis. The corresponding procedure is given in the SXT website data analysis page:

http://www.tifr.res.in/~astrosat_sxt/page1_data_analysis.php

More information about SXT can be found at the SXT POC website:

http://www.tifr.res.in/~astrosat_sxt/home.php

Writing an SXT Proposal

The details of proposal preparation and required resources can be found at

http://astrosat-ssc.iucaa.in/?q=proposal_preparation

Note that there is an offset between the SXT pointing and the pointing of LAXPC, CZTI and UVIT. These offsets are of the order of a few arcmins. Therefore, the proposers should use the PC mode when SXT is not the primary instrument. This is because, the source may be out of the SXT FoV for the FW mode in this case. However, one may need to use the SXT FW mode for some science goals in order to reduce pile-up and/or to have better time resolution. In such a case, proposers should make SXT the primary instrument, even if SXT does not serve the primary science.

Chapter 4

Large Area X-ray Proportional Counter

Large Area X-ray Proportional Counter (LAXPC) is one of the major payloads on ASTROSAT, which covers energy range of 3 – 100 keV and with its large area of collection, about 6000 cm^2, it is well suited for timing and spectral measurements. The large detection volume (15 cm depth) of LAXPCs and being filled with xenon gas at 2 atmospheres pressure, results in detection efficiency greater than 50%, in 30-80 keV band. These three LAXPC units on ASTROSAT will thus have the largest effective area and sensitivity among all the satellite missions flown so far for X-ray astronomy studies in 20-100 keV energy range.

The principal scientific objectives of LAXPC are as follows:

- Detailed studies of stellar-mass black holes with masses ~ 3-10 $M_{\cup}$ in our Galaxy and the neighbouring galaxies and massive black holes (~10_6 to 10_9 $M_{\cup}$) in AGNs will be realized with the LAXPC instrument. This will be achieved by measuring variations in the luminosity of sources and the time scales of variations.

- Studies of periodic (pulsations, binary light curves, QPOs etc.) and aperiodic (flaring activity, bursts, flickering and other chaotic variations) variability in X-ray pulsars and other X-ray binaries, coronal X-ray sources, Cataclysmic Variables (CVs), Active Galactic Nuclei (AGNs) and other galaxies etc. by high time resolution (~10µsec) photometry over a wide spectral band covering 3-100 keV with

- a single instrument. Rapid variability studies e.g. sub-second variations, high and low frequency QPOs and kHz QPOs in soft and hard x-ray bands, probe astrophysical processes closest to the central source.

- Low to moderate spectral resolution studies of continuum X-ray emission over a broad band of 3-100 keV for X-ray binaries, Supernova remnants (SNRs), CVs, Stellar Coronae, AGNs etc. This will be done using large area and low to moderate energy resolution (Δ E / E ~ 10 to 20 %) of LAXPCs.

- Correlated time variations of intensity in 3-100 keV band with those in the visible, UV and soft X-ray (0.3-8 keV) bands to investigate the origin and mechanism of emission of radiation in different wave bands.

- Discovery of non-thermal components in the X-ray spectra of SNRs and Clusters of Galaxies by accurate spectral measurements in 3-100 keV band combined with simultaneous measurements from SXT in 0.3-8 keV region to estimate their magnetic field strength as well as to understand the acceleration processes and origin of cosmic rays in the case of SNRs.

- Measuring magnetic fields of neutron stars by detection and studies of cyclotron lines, most of which lie in 15-60 keV regions in the X-ray spectra of x-ray pulsars.
- Search for X-ray transient sources will be conducted by repeated surveys in the limited regions of the galactic plane with the LAXPC

Payload configuration:

The LAXPC instrument sensitive in 3-100 keV band, consists of 3 identical units, each with its own independent front-end electronics, HV supply, and signal processing electronics to facilitate easy replacement of the entire LAXPC unit in case any problem is encountered before the launch. The Time mark generating electronic unit is common for all the 3 LAXPCs. The data from all the 3 LAXPCs are independently acquired preserving the identity of each unit. These data are merged in a single telemetry data stream from which data for each LAXPC is recovered.

LAXPC Flight Packages

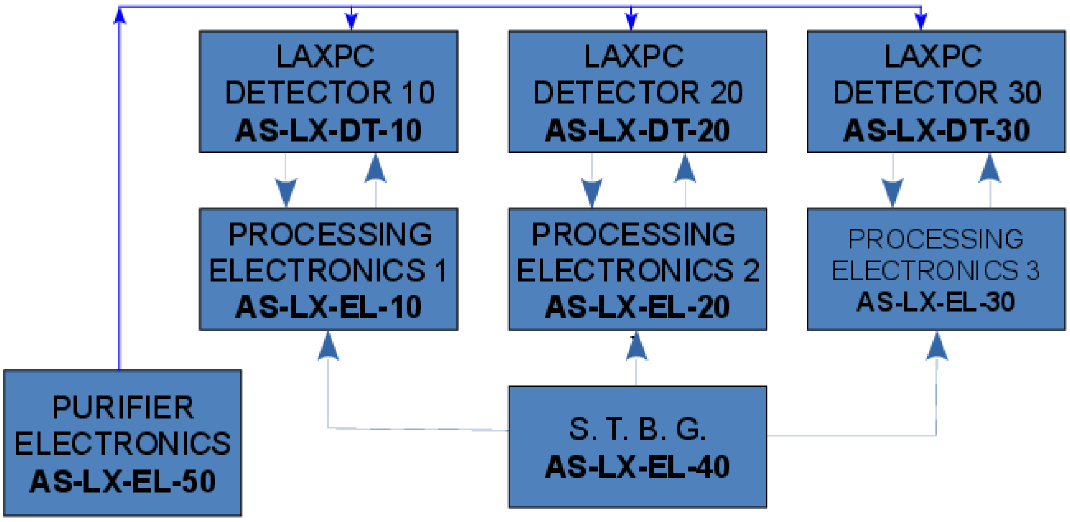

All the three LAXPC flight detectors in Assembly, Integration and Testing lab (AIT) lab of ISAC after successfully completing all flight tests and final calibration (20 th October, 2014). The purification pump is seen as black box in each detector. At the top is the protection cover which was removed before the launch

Instrument Specification:

No. of LAXPC Detectors	Three (3) Identical units
Detector size	120 cm x 50 cm x 70 cm
X-ray detection volume	100 cm x 36 cm x 15 cm
No. of anode layers	5 anode layers : each has 12 anode cells surrounded on 3 sides with Veto cells
Veto layers	46 anode cells each with cross-section of 1.5 cm x 1.5 cm arranged on three sides of X-ray detection cells
Collimator field of view	0.9^o X 0.9^o for all the LAXPCs
Collimator Height	45 cm for WSC+FOV collimator
Counting Gas	Xenon + Methane
Gas Pressure	Two atmosphere (1520 torr)
Energy range	3-100 keV
Total Effective Area of 3 LAXPC Detectors	About 6000 cm^2 in 5-20 keV
Total Weight of LAXPC	419 Kg (Detector + Electronics)

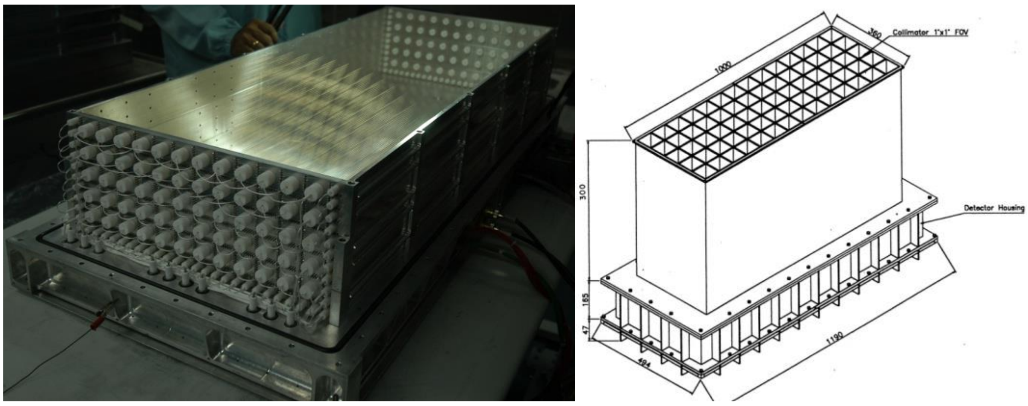

LAXPC Detector wire frame and detector schematic

Details of detector system:

Each LAXPC detector consists of 60 anode cells of 3 cm x 3 cm cross-section and length of 100 cm, arranged in 5 layers providing a 15 cm deep X-ray detection volume. Each Anode Layer thus has 12 anodes with a total width of 36 cm. A Veto Layer made up of 46 anode cells each with cross-section of 1.5 cm X 1.5 cm surrounds the main X-ray detection volume on 3 sides to reject events due to charged particles and interaction of high energy photons in the detector. The alternate anode cells of Layer 1 and 2 are linked together and thus 4 outputs are obtained from Layer 1 and Layer 2. The anode cells in each of the Layer 3, 4 and 5 are linked together to provide one output from each layer. Thus, there are 7 anode outputs that are operated in mutual anticoincidence to reduce the non-cosmic X-ray background The Veto layer is divided in 3 parts providing 3 Veto Layer outputs. The left side and right side veto anodes are linked together to provide one output from each one and the third veto output is from the bottom layer veto anodes linked together. The configuration of anodes is shown in the figure.

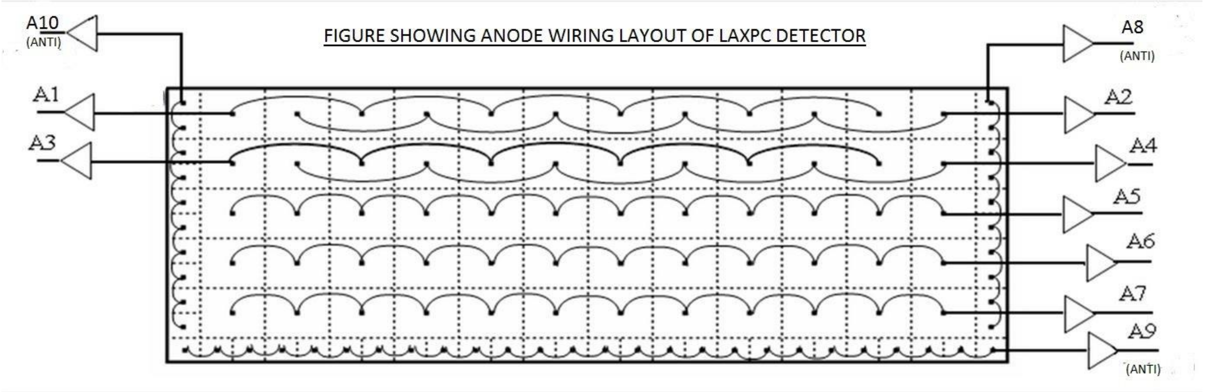
FIGURE SHOWING ANODE WIRING LAYOUT OF LAXPC DETECTOR

To suppress background from charged particles all events, which register in multiple anodes, or those, which trigger the veto anodes are rejected, except for the situation where one of the energies is in the K X-rays for Xenon. For X-rays with energy above the K-edge of Xe, a K-electron may be ejected and the ion can radiate a K X-ray photon in energy range 29.4 - 34.4 keV. These X-ray may escape from the detector or be absorbed in a different anode. In order to include such events the anticoincidence logic is modified to detect this energy range. If two main anodes register an event and at least, one of them is in the energy range, of 25-35 keV, then the energy of the two anodes are added and the event is accepted. The lower threshold for this (KLLD) and the upper threshold (KULD) can be set through tele-command.

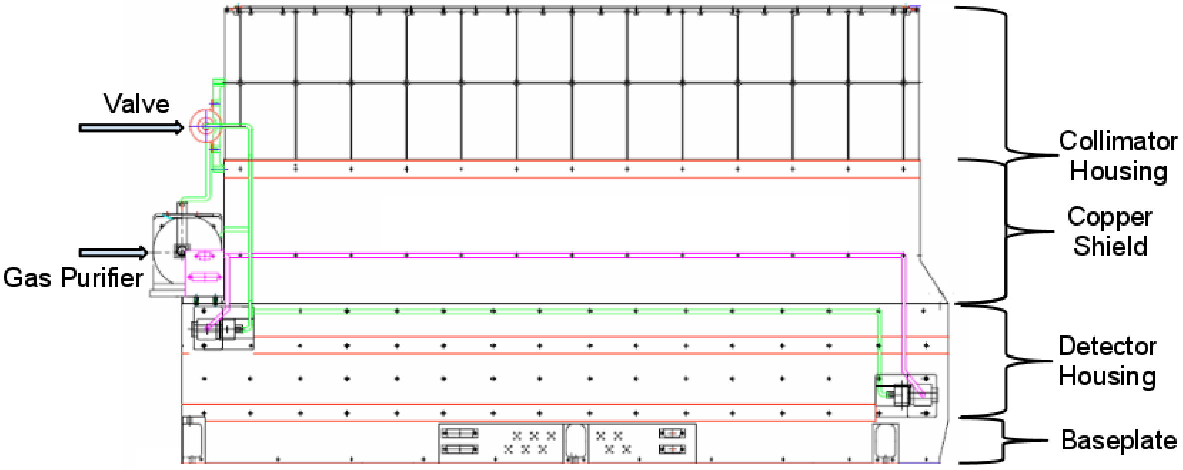

LAXPC SCHEMATIC BLOCK DIAGRAM

A 50 micron thick aluminized Mylar film serves as the gas barrier as well as the X-ray entrance window for the detector. The detector is filled with a mixture of 90 % Xenon + 10 % Methane at a pressure of 1520 torr. LAXPC30 has a slightly different gas-mixture as compared to other two detector units (84.4% Xenon, 9.4% Methane and 6.2% Argon). The Mylar window is supported against the gas pressure by a honeycomb shaped collimator made of square geometry aluminium cells termed as Window Support Collimator (WSC). The Field Of View Collimator (FOVC) is placed above the WSC and is aligned with the openings in the WSC. The FOVC is made of sheets of tin, copper and aluminium and is placed in a collimator housing. The total height of the collimators is about 45 cm giving a Field of View (FOV) of about 0.9 degree X 0.9 degree. A one mm thick tin sheet coated with copper serves as the shield for X-rays entering the detector from the sidewalls.

Processing electronics and Timing capability:

There are 7 anode outputs from the X-ray detecting cells and 3 veto outputs from each detector that are fed to 10 charge sensitive preamplifiers (CSPAs). High voltage to the anodes is supplied from a command controlled HV unit whose HV output can be varied by command. The 7 X-ray anode and 3 Veto layer outputs from the CSPAs are sent to the peak detectors and events satisfying the selection logic as true X-ray events are further processed by signal processing electronics for

(a) Broad Band (BB) counting

(b) for time tagging of every event with its energy to an accuracy of 10 micro-sec.

Details of Broad Band Counting:

For the purpose of BB counting the Bin time can be selected, in multiple of 2, from 16 msec to 2048 msec, 128 msec being the default value. The Bin times for the BB counting is selectable by command.

For BB counting output Anode 1 & 2 are combined as layer-L1, similarly Anode 3 & 4 are combined as layer – L2 and Anode 5, 6 & 7 are combined as layer – L3. All Anti anode A8, A9 & a10 are combined as Anti counter. All the events in each LAXPC above a lower energy threshold of 3 keV in main anodes (A1 to A7) (LLD), upper energy threshold of 80 keV in main anodes (A1 to A7) (ULD), all the three Veto layer counts termed as Anti counts and several other count rates detailed below, are also recorded in separate counters.

Counters Pulses for LAXPC counters from Event Processing Logic

There are 7 Main Anodes and 3 Anti Anodes structured as follow:

Layer-1:	Anode-1 & Ande-2. (Frame-1)
Layer-2:	Anode-3 & anode-4. (Frame-2)
Layer-3:	Anode-5 (Frame-3) & Anode-6 (Frame-4) & Anode-7 (Frame-5).
ANTI-1:	Right-side Anti-Anode -A8
ANTI-2:	Bottom Anti-Anode -A9.
ANTI-3:	Left-side Anti-Anode -A10.

COUNTER	No of bits (counter bits+over flow flag bit)	REMARK
LLD	12 (11+OFF)	Events crossing 3keV in any of 7 Main Anodes (A1 to A7)
ULD	11(10+OFF)	Events crossing 80keV in any of 7 Main Anodes (A1 to A7)
ANTI	12 (11+OFF)	Event in any of 3 Anti Anodes (A8 to A10) above 3keV.
MTO	11 (10+OFF)	More than One Simultaneous Events (within 6uS) in any of 10 Anodes (A1 to A10).
MTT	11 (10+OFF)	More than Two Simultaneous Events (within 6uS) in any of 10 Anodes (A1 to A10).
ANTI-1	11 (10+OFF)	Events crossing 3keV in Right ANTI Anodes (A8).
ANTI-2	11 (10+OFF)	Events crossing 3keV in Left ANTI Anodes (A9).
ANTI-3	11 (10+OFF)	Events crossing 3keV in Bottom ANTI Anodes (A10).
GE/JE	12 (11+OFF)	Genuine Events which has satisfied the criterion.
NK	11 (10+OFF)	MTO Events, None of the events in K-band.
DEK	9 (8+OFF)	MTO Events, One in K-band and another in Non-K-band.
DK	9 (8+OFF)	MTO Events, both events are in K-band.

Colour Counts	L1	L2	L3	
3-80keV	11 (10+OFF)	11 (10+OFF)	11 (10+OFF)	Single Events between 3-80keV in Particular Layer / Anode.
3-6keV	11 (10+OFF)	9 (8+OFF)	9 (8+OFF)	Single Events between 3-6keV in Particular Layer / Anode.
6-18Kev	11 (10+OFF)	9 (8+OFF)	9 (8+OFF)	Single Events between 6-18keV in Particular Layer / Anode.
K-band (25-35keV)	9 (8+OFF)	9 (8+OFF)	9 (8+OFF)	Single Events in K-Band (i.e. between 25-35keV) in Particular Layer / Anode.
18-40keV	9 (8+OFF)	9 (8+OFF)	9 (8+OFF)	Single Events between 18-40keV in Particular Layer / Anode.
40-80keV	9 (8+OFF)	9 (8+OFF)	9 (8+OFF)	Single Events between 40-80keV in Particular Layer / Anode.

Note:

All counters are counting pulses after about 1.5/2uS of the Master Gate Closing.

All Colour counts are counted for Single events only,

Total = 30 counters =>3x12 ibt, 12 x 11 bit & 15 x 8 bit counters. Each counters has an Over Flow Flag (OFF).
11 & 10 bits countes uses two bytes with remaining MSB bits set to zero: 0000 0ccc, cccc cccc / 0000 00cc, cccc cccc.
All over flow bits are combined as bytes and put seperatly.

Various counters in BBC frames are as follow:

16 (11/10) bit Counters	**Description**
0	ANTI-2 (2+8 BIT)
1	ANTI-1 (2+8 BIT)
2	ANTI (3+8) (all 3 ANTI ORed)
3	ANTI-3 (2+8)
4	ULD (2+8)
5	MTO (2+8)
6	LLD (3+8) (only main 7 anodes ORed)
7	MTT (2+8)
8	L1-3-80K (2+8)
9	GE/JE (3+8)
10	L2-3-80K (2+8)
11	L1-6-18K (2+8)
12	L3-3-80K (2+8)
13	L1-3-6K (2+8)
14	NK (2+8) (MTO events but both Non-K)

8 bit Counters	**Description**
0	K1 *(Layer-1 K-event)*
1	L1-40-80K
2	L3-18-40K
3	L3-6-18K
4	L2-18-40K
5	L2-6-18K
6	L1-18-40K
7	L3-3-6K
8	L2-40-80K
9	K2 *(Layer-2 K-event)*
10	L3-40-80K
11	K3 *(Layer-3 K-event)*
12	DK *(MTO events but both K)*
13	DEK *(MTO events: one K & other Non-K)*
14	L2-3-6K

B57 to 60 OFF bytes of BBC sub-frame

Over-Flow-flag (OFF) BIT	Counter
B57.7	OFF-ANTI-2
B57.6	OFF-ANTI-1
B57.5	OFF-ANTI
B57.4	OFF-ANTI-3
B57.3	OFF-ULD
B57.2	OFF-MTO
B57.1	OFF-LLD
B57.0	OFF-MTT
B58.7	OFF-L1-3-80K
B58.6	OFF-GE
B58.5	OFF-L2-3-80K
B58.4	OFF-L1-6-18K
B58.3	OFF-L3-3-80K
B58.2	OFF-L1-3-6K
B58.1	OFF-NK
B58.0	OFF-K1
B59.7	OFF-L1-40-80K
B59.6	OFF-L3-18-40K
B59.5	OFF-L3-6-18K
B59.4	OFF-L2-18-40K
B59.3	OFF-L2-6-18K
B59.2	OFF-L1-18-40K
B59.1	OFF-L3-3-6K
B59.0	OFF-L2-40-80K
B60.7	OFF-K2
B60.6	OFF-L3-40-80K
B60.5	OFF-K3
B60.4	OFF-DK
B60.3	OFF-DEK
B60.2	OFF-L2-3-6K
B60.1	0
B60.0	0

Modes of operation of LAXPC:

The LAXPC payload consists of three independent LAXPC units with identical operational modes. There are three different modes of operation and each instrument can be operated simultaneously in more than one mode.

The LAXPC data carries information about cosmic X-rays detected with the instruments and it has three entries:

(a) time of detection

(b) energy (spectral channel) of the X-ray photons and

(c) identity of the detecting element (detector/anode-layer) including double-identity in some cases.

The signals generated by the instrument after detection of X-rays are processed and stored in any of the following modes.

- **Normal (or Default) Modes of Operation:**
  In Normal operation, there are two modes running simultaneously and data are acquired from each LAXPC.

  (a) Broad Band Counting Data: Records the rate of occurrence of events in various energy bands with selectable time Bin (16 msec to 2048 msec). Default value is 128 msec. Details of the count rate capabilities of the various counters are given in the table. There are 15 counters for the broad band counting of the valid X-ray events in different energy bands covering 3-100 keV from 3 layers as discussed earlier.

  (b) Event Mode Data: in this mode, arrival time of each event is time tagged to an accuracy of 10 microseconds. Simultaneously the energy and identity of each event is also recorded. This mode generates 5 bytes data for each accepted and analysed event. In this mode, the dead time of the detector is around 54 microseconds.

- **Fast Counter Mode:**
  In this mode, the event rate is measured only from the top layer of each LAXPC detector in 4 energy channels covering 3-20 keV band with a fixed time bin of 160 microsecond. In this mode, dead time is about 10 microsecond. Each of 4 counters are 8 bit deep and cover 3-6,6-8 , 8-12 and 12-20 keV energy bands. This mode is to be used for studying rapid variability during the short duration flares or outbursts of sources.

Data from different modes of observation will be treated separately. The extraction criteria will be user defined and will require input from the housekeeping parameters. The auxiliary data will have to be processed separately. Certain housekeeping information will be derived independently from detector raw data.

Detection Efficiency and Effective Area:

Detection efficiency is determined by the thickness of entrance window at the low energy end and by the probability of photoelectric interaction in the detector gas volume at the higher energy end. GEANT4 simulations of detector have been used to estimate the effective area and field of view. The simulations were validated by comparing the simulations with observations using radioactive sources. The field of view (FWHM) is found to be 43’ at 15 keV, 47’ at 50 keV and 52’ at 80 keV. The increase in field of view with energy is due to some part of the collimator becoming nearly transparent to high energy X-rays. The effective area calculated through simulations is reduced by 7% to account for imperfections in collimator as estimated by calibration using radioactive sources. A plot of effective area of the detector as a function of energy of X-rays is shown in figure, which also shows the same for RXTE.

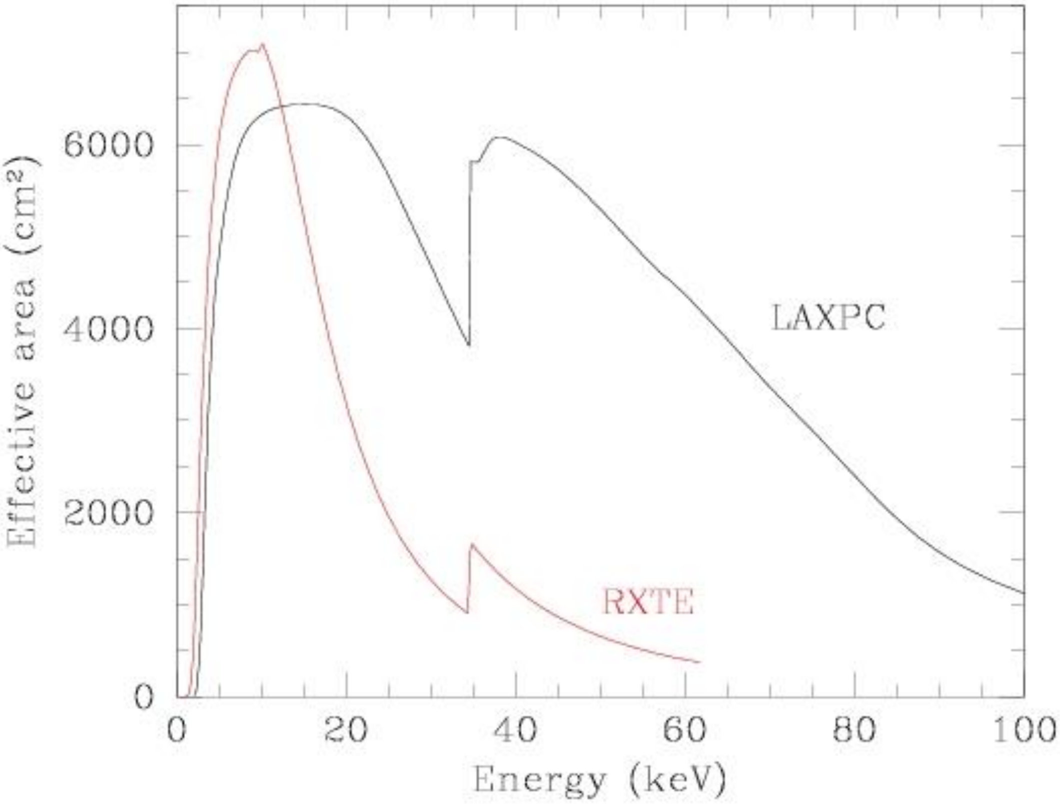

Effective area of LAXPC and RXTE. The LAXPC effective area first derived in lab from simulation and finally corrected with Crab observations in the orbit
(Antia et al (2017) http://arxiv.org/abs/1702.08624)

Dead Time Measurement of LAXPC Detector:

The test has been carried out using commercial mini X-ray gun (MINI X) mounted on specially designed X-Y source motion jig. The jig allows movement of the X-ray gun in controlled speed along both X and Y axis over the complete area of LAXPC detector. To avoid overexposure at one spot on detector, the X-ray gun is kept moving at slow speed along the length of cell. A commercial MCA is used to record the spectrum and counts for different event rates. The MCA provides dead time corrected incident event rate. The same setting of X-ray gun and jig is then used and event data are acquired with LAXPC PE and STBG unit. The counts as measured by MCA, is used as actual input counts and using the measured counts, the dead time is calculated as shown in figure. This measurement confirms with the number arrived at from analysis of processing time in electronics and the timing diagrams for the same.

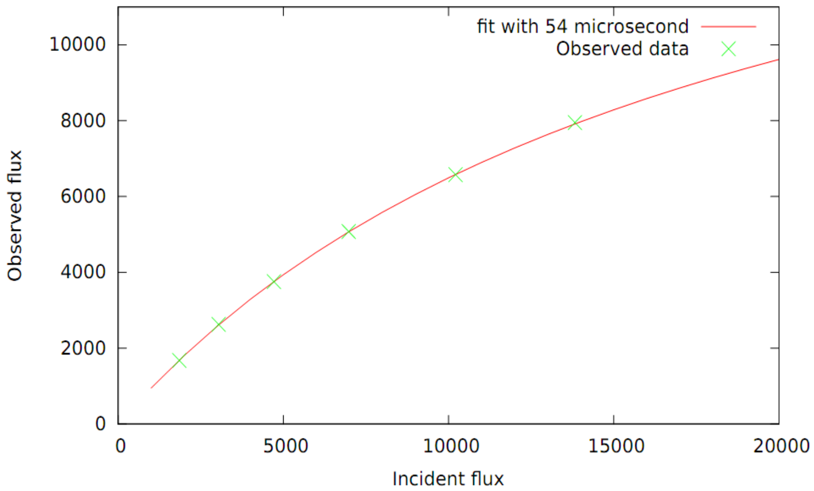

Dead time of LAXPC detector observed during initial development of the LAXPC instrument in the lab

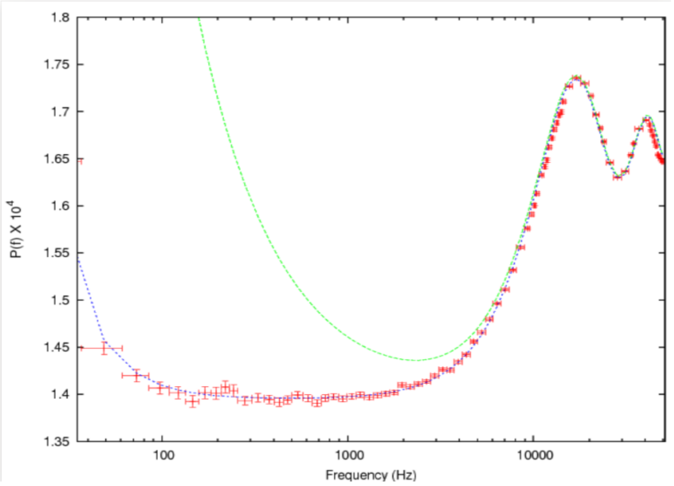

High frequency re-binned Power Density Spectrum (PDS) of GRS 1915+105 in the SPL class observed during 5-7 March 2016 which estimates dead time of 42.3 microsecond (Yadav et al. (2016) ApJ, 833, p27). See text for detail

Dead time was further reduced to ~ 43 microsecond by optimising reading and writing sequences. During the performance verification phase, Astrosat observed the black hole system GRS 1915+105 during 5-7 March 2016. To test the timing characteristics of the detector, event mode data is used to calculate the power density spectrum (PDS) up to the Nyquist frequency of 50 kHz which is shown in above figure. The resulting PDS does not show any instrumental effect other than peaks beyond 10 kHz due to thedead time of the detector (which gives dead time ~42.3 microsec). The green line in the figure shows the expected peak power of a quasi-periodic oscillation (QPO) with quality factor Q=4 and rms of 5%. This implies that LAXPC instrument can detect QPOs of such a strength easily till 3000 Hz.

Instrument Calibration:

Ground calibration:

To obtain the energy response of detectors, 3 radioactive sources at different energies in the range of LAXPC detector were used. The calibration was repeated at 3 temperatures of 10°C, 20°C and 30°C to study the temperature dependence of detector response. The following 3 sources were used:

1. **Fe_{55} with energy 5.9 keV.** These X-rays are absorbed in the top layer and hence only the two top anodes A1, A2 register these events.

2. **Cd_{109} with energies, 22.1 keV (54.5%), 21.9 keV (28.8%), 24.9 keV (13.7%), 88.0 keV (3.0%).**

   The detector cannot resolve the first two peaks, while the third one gives a small feature at the high end of the main peak, which can be fitted with some effort. The last peak is beyond the range of the detector, but it can give a small contribution when the Xe-K X-ray escapes the detector. However, the resulting peak is too weak to be detected.

3. **Am_{241} with energy 59.6 keV.** This source also gives additional peaks because of loss of energy due to Xe-K X-rays escaping the detector. The detector logic is built to add contributions in 2 channels, if one of them is in the range of Xe-K (25 –35 keV). Hence, the 59.6 keV peak consists of 2 parts, one where the entire energy is absorbed in the same anode and second where the Xe-K X-ray is absorbed in a different anode and the two contributions are added to one of the anode. If only one anode is in the Xe-K range the energy deposited in that anode is added to the other anode where remaining energy is deposited. If the energy deposited in both anodes is in the Xe-K range then the lower of the two energies is added to the anode, which has higher energy. The Xe Kα X-rays have energies of 29.8 keV and 29.5 keV, which account for about 81% of Xe-K X-rays, while the remaining fraction comes as Xe K-beta with energies 33.6–34.4 keV. Thus in addition to the 59.6 keV peak we also get two peaks when Xe-K X-rays escape from the detector giving the energies of about 30 keV and 26 keV. Because of limited resolution of the detector, the last two peaks are not well separated.

In order to estimate detector background, the counts are recorded without any source, before and after the source measurements are done. The background counts over a time interval equal to that for source are then subtracted from counts with source to get the net contribution from the source. All these measurements were done inside the thermovac.

In order to perform the calibration inside the thermovac chamber, an x–y motion platform for movement of radioactive sources above the Field of View (FOV) Collimator was designed. This can hold all three sources and expose one or more of them at a time. The x–y motion platform can function in vacuum and its movements and source on/off status can be controlled remotely. The movement of sources is controlled by a program to move the source at predetermined rates in x or y direction. To cover the entire area of the detector the source was moved along the y direction that moves it across the 12 cells followed by a movement along X axis. The sequence is repeated until the entire range is covered. Figure below shows the route traced by the source. To determine the characteristics of individual cells some scans were also done along each of the 12 cells, where the movement was restricted to x direction only along the wire.

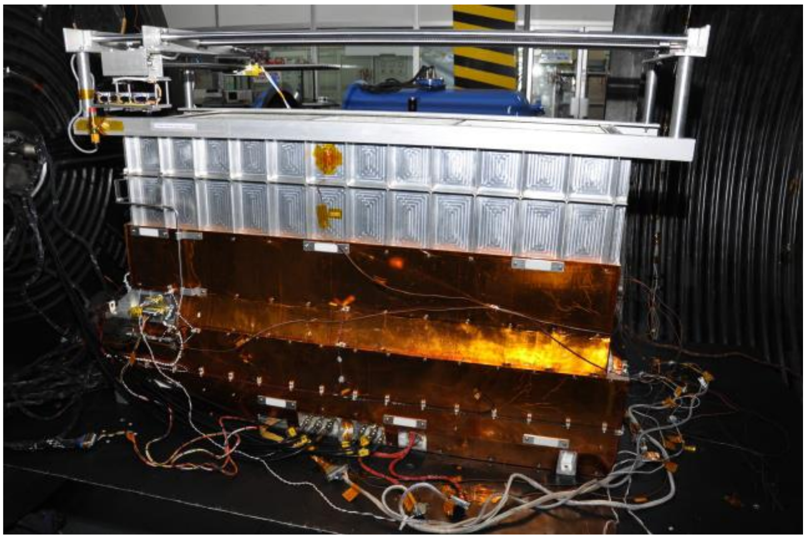

X-Y source motion on LAXPC Detector for the calibration in vacuum chamber

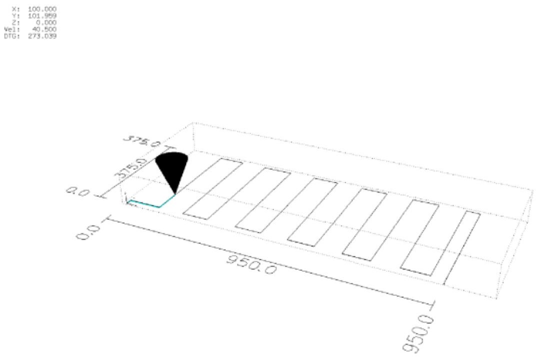

X-axis (across the anode wire) calibration pattern.

Energy Resolution as a function of energy:

The energy resolution and channel to energy mapping were calibrated using three radioactive sources, Fe_{55} (5.9 keV), Cd_{109} (22 keV/ 24.9 keV) and Am_{241} (59.6 keV). In order to perform the calibration inside a thermovac chamber, an x-y motion platform for movement of radioactive sources above the FOVC was designed. This can hold all these sources and expose one or more of them at a time. The movement is controlled remotely and can be programmed. The movement of source across the detector also allows us to estimate the transmission efficiency of collimator due to possible imperfections in the collimator fabrication. The calibration was repeated at temperatures of 10 C, 20 C and 30 C to study the temperature dependence of energy resolution and peak position.

The spectra of the three sources and background obtained from observations at 10 C and the energy resolution and the peak channel for the 4 main peaks in the spectra are shown in the following figure.

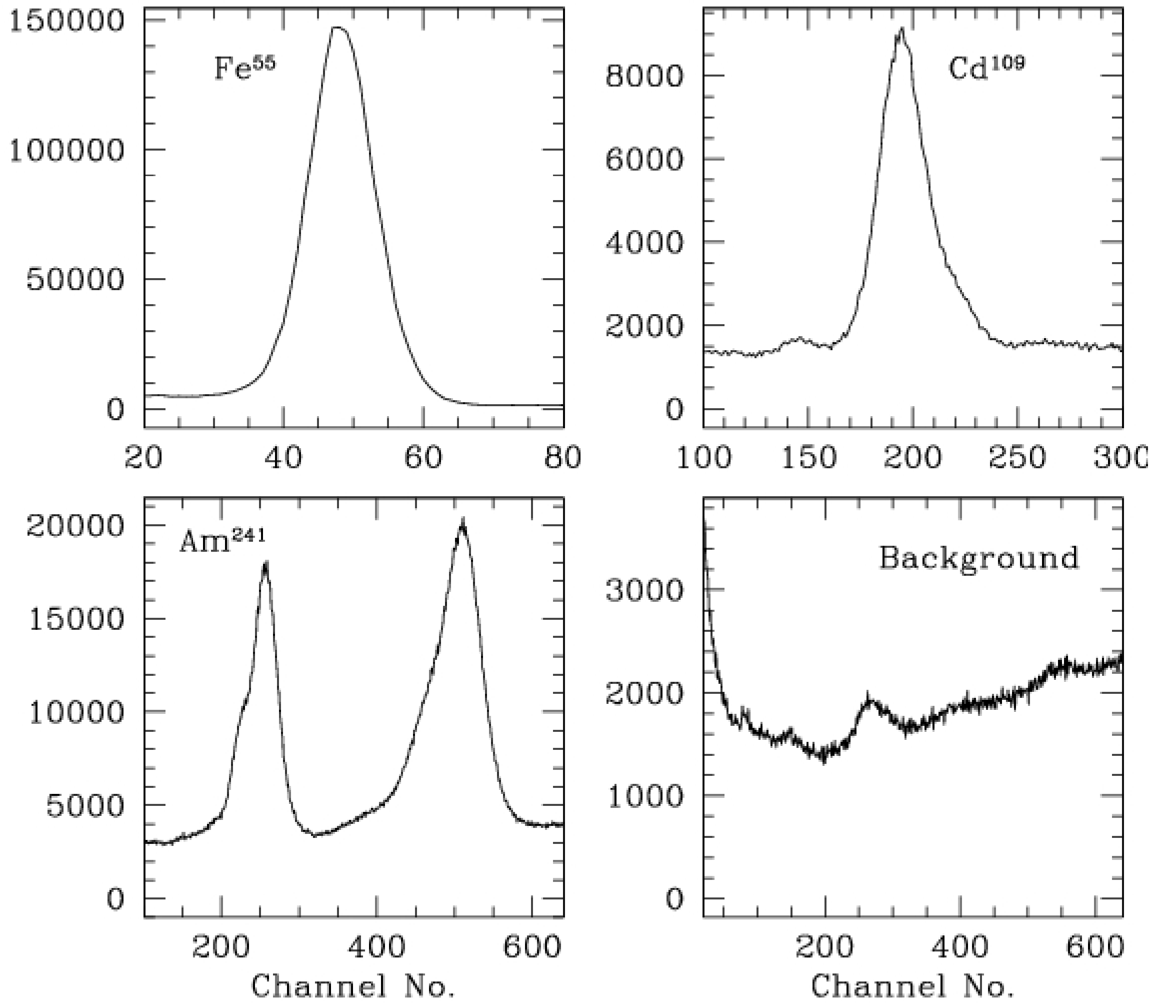

The observed spectrum of three radioactive sources and background in thermovac

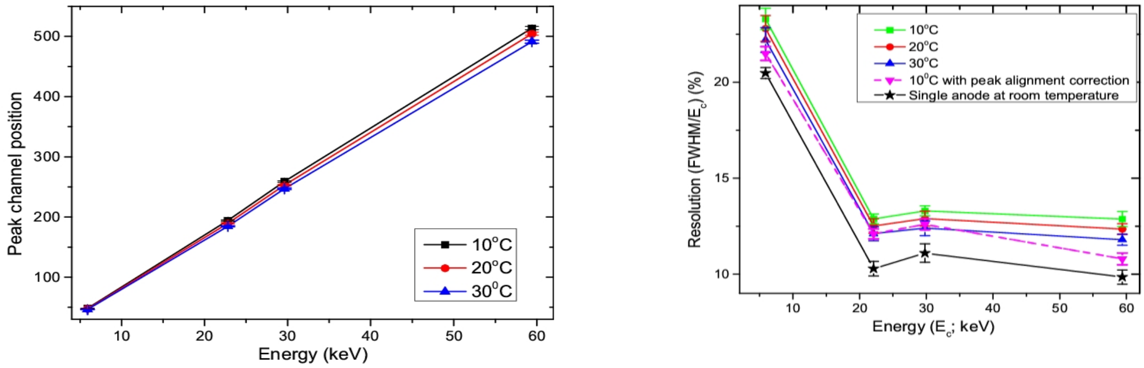

The energy to peak channel mapping and the energy resolution for LAXPC10 as measured on ground

Energy(keV)	Energy Resolution (%)			Peak Channel		
	10° C	20° C	30° C	10° C	20° C	30° C
5.9	23.4±0.6	22.9±0.7	22.2±0.7	48.2±0.6	47.4±0.6	46.3±0.6
22.1	12.9±0.3	12.5±0.4	12.1±0.6	194.2±2.5	189.5±2.3	184.6±2.4
29.8	13.3±0.3	12.9±0.4	12.5±0.4	259.0±3.4	253.0±3.0	247.0±3.2
59.6	12.9±0.4	12.4±0.3	11.8±0.3	513.9±6.7	504.5±6.1	491.2±6.4

To validate the GEANT4 simulation the events for each radioactive source were simulated. The total energy deposited in each anode was calculated for each event. In order to simulate the effect of finite energy resolution a random number with normal distribution is added to the energy in each cell. The random number is selected to have a zero mean and a standard deviation of σ. Here the relative standard deviation σ are treated as free parameters, which are chosen to get the best fit to observed spectra. For each peak in the spectrum we use a different σ. This gives 4 parameters, one each for Fe^{55} and Cd^{109} peaks and two for Am^{241} spectrum. Although, some of these peaks have multiple energies which are not resolved, we use the same σ for the entire peak. The total energy, E, in each anode is translated to channel number, n_c, using

$$n_c = e_0 + e_1E(1+e_2E)$$

Here e_2 gives a small nonlinear contribution, which is required to fit all spectra. Because of this nonlinearity the peak in Am^{241} spectrum around 60 keV is split into two parts, one due to events where entire energy is deposited in one anode, and second where the energy is split between two anodes and is then added, as one of the energy is the Xe K rays range. This gives rise to an asymmetry in this peak. The energy resolution of the two peaks is also different. The effective resolution of this peak quoted in the table above is in between that for the two peaks. The fitted resolutions for the four peaks are shown in figure, which also gives a linear spline interpolation for σ^2.

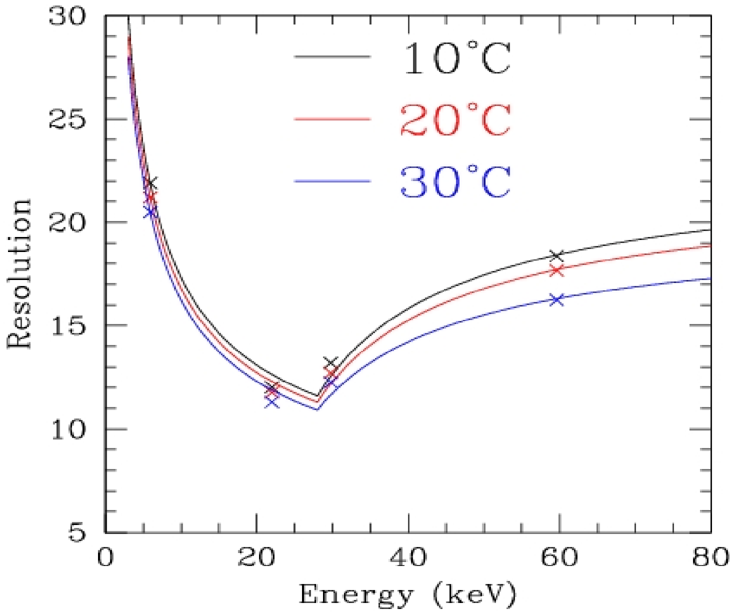

Energy Resolution at various energy at three different temperatures

The energy resolution of LAXPC 10 detector as estimated by fitting observed spectrum for the three radioactive sources to that from GEANT4 simulations.

At 20 C, the channel number is given by e_0=-3.3, e_1=9.16 keV^{-1}, e_2=0.0018 keV^{-1}. These fitted parameters are used to generate the response matrix for the detector.

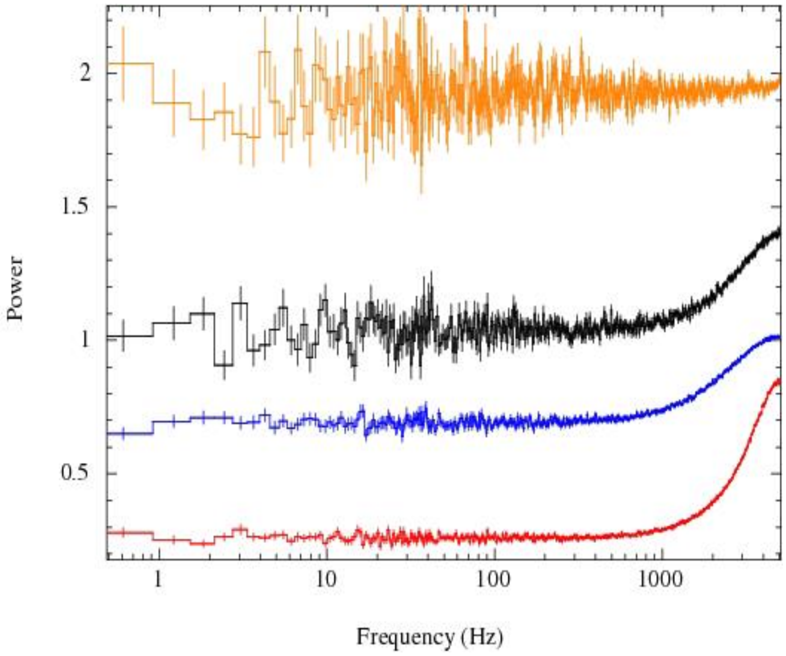

Power spectra obtained from event mode data at different count rates

The timing characteristics of LAXPC event mode data is as expected (featureless) at frequencies below 390 Hz corresponding to bin size of 2.56 ms. The power density spectra obtained from light curves at different rates up to 12500 c/s are shown in above figure. At higher count rate, the spectra shows lesser power, which is expected due to the dead time of the LAXPC processing electronics.

Expected background in different energy bands:

Background spectra in the laboratory is shown in figure below. To estimate the background in orbit we did GEANT4 simulations for photons and charge particles with various energies. These simulations included the collimator as well as shield surrounding the detector. It appears that major contribution may be due to diffuse X-ray background. For this purpose, we assumed a background flux of 87.4 $E^{-2.3}$ cm^{-2} s^{-1} keV^{-1} steradian^{-1}. The estimated background combining all 3 LAXPC detectors is shown in the figure. The actual background in orbit can only be measured after launch of ASTROSAT.

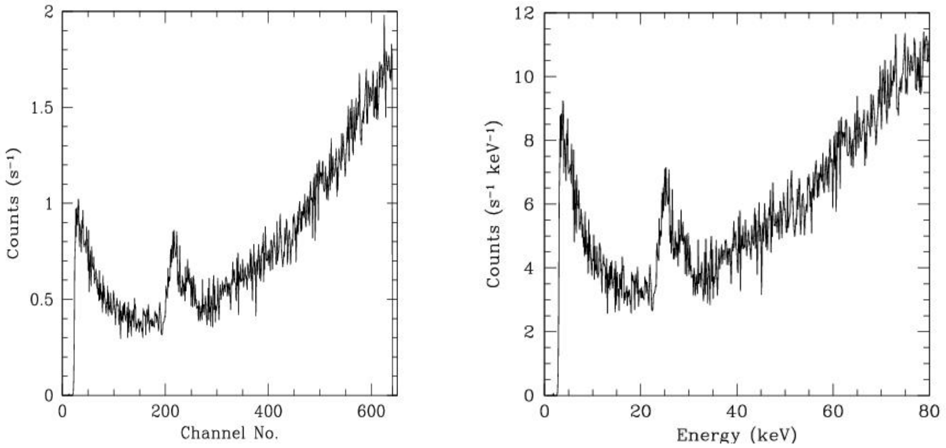

The total background is expected to be about 500 s^{-1}. In the low energy band of 3-20 keV the background is about 80 s^{-1}

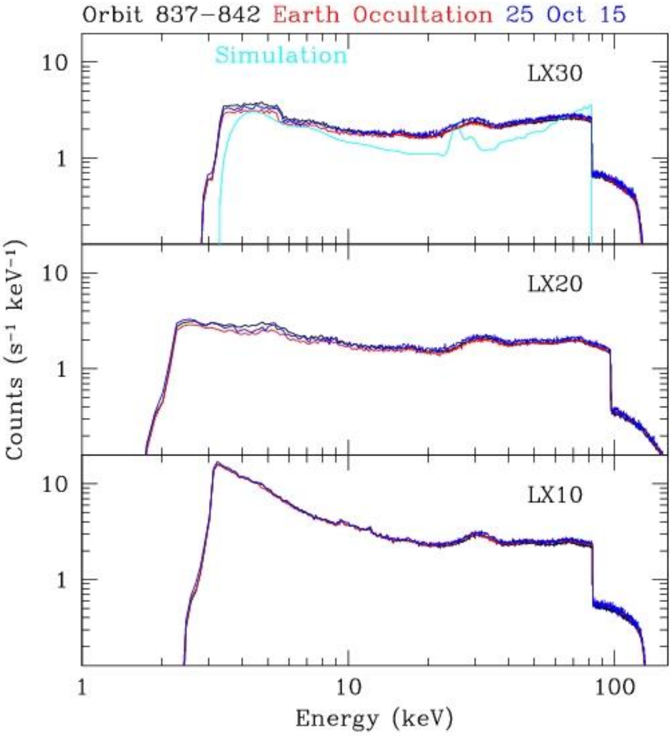

Above Figure shows the observed background in orbit 837-842 (black), earth occultation background and simulation X-ray background (for LAXPC30 only) from diffused X-ray flux (local satellite contribution is not take care). LAXPC 10 (lower panel has more background at lower energy as veto Anode 10 is disabled in this detector unit

Time exposure for sources of different intensity:

Using the response matrix generated it is possible to simulate the response of detector at different energy spectra. The figure shows the response for different mono-energetic sources.

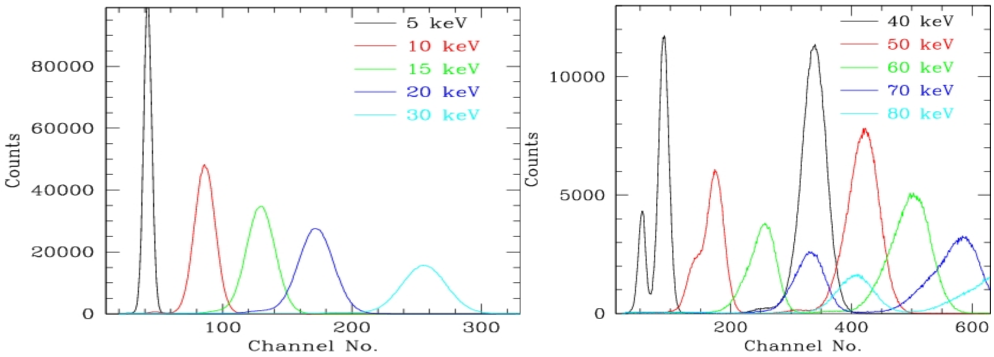

The simulated spectra for the Crab source with 100 s observation is shown in the figure. This gives a count rate of about 5000 s^{-1}

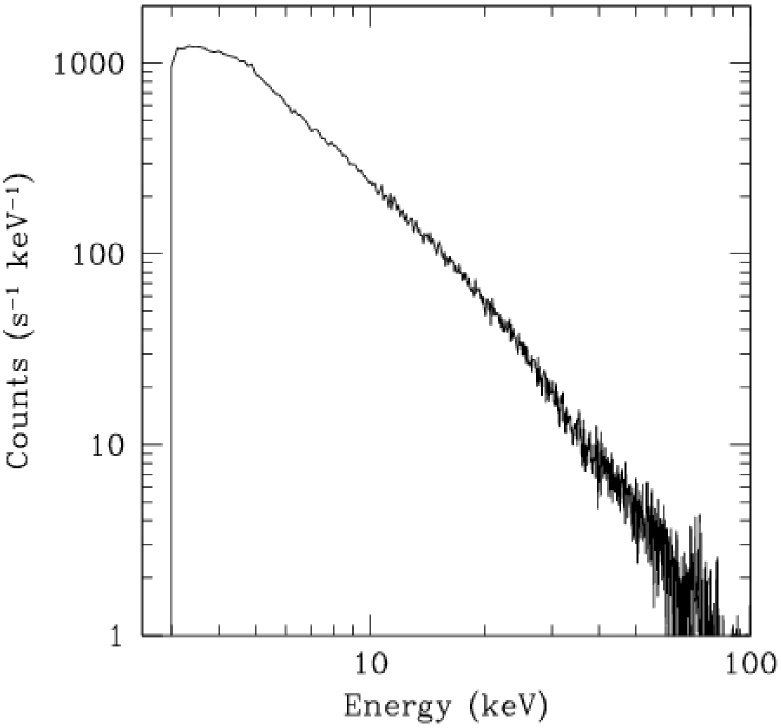

Simulated spectrum for Crab X-ray source

For a 1 mCrab source observation over 100 s can detect it at 3σ level in 3-100 keV. If the energy range is restricted to 3-10 keV, the detection improves to 6σ level.

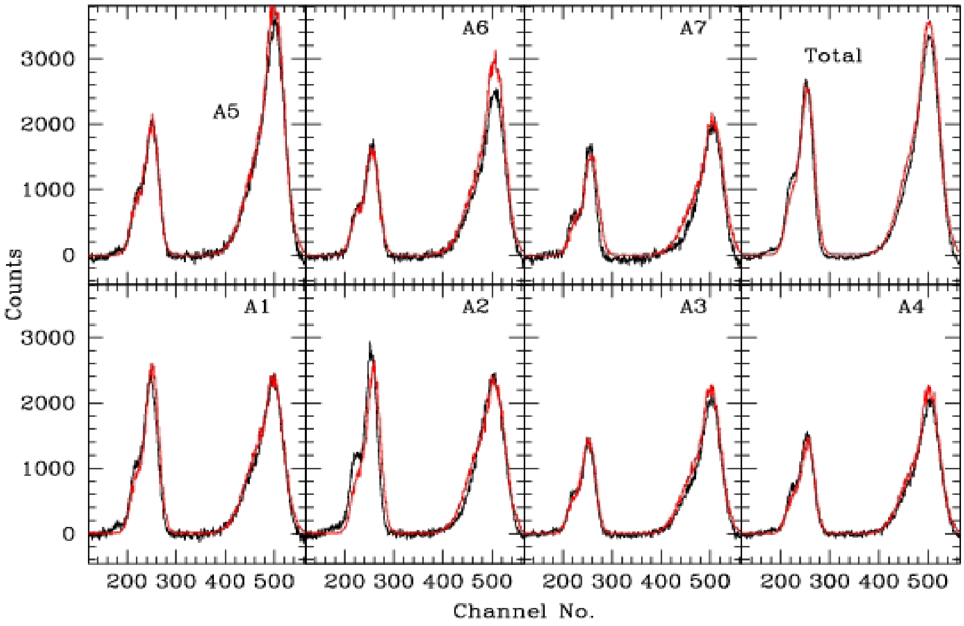

Above figure shows GEANT4 simulation for Am^{241} scan for LAXPC30 detector system. It provides 30 and 60 keV peaks. The results are shown for individual anodes A1-A7 with total. Black is Am^{241} scan data while red is GIANT4 simulated results

Observation Strategies for LAXPC:

- Time tagged photons for periodic and fast time variability studies
- Spectral features using individual photon energy measurement data
- Fast timing mode data for bright and bursting sources
- Broad Band Counting (BBC) for quick study of time variability

Integration time for the BBC will depend on the source intensity and time scale of variability.

- For studying variability over time scale << 1 sec, use BBC integration time of 16 msec, for a few sec variability use 64 / 128 msec and for still slower variations use 1.024 sec BBC BIN time.
- For study of fast pulsars (e.g. 33 msec pulsar in Crab Nebula) or millisecond accreting pulsars or rotation powered pulsars of << 1 sec period use time tagged photon data**.**
- For very bright sources like Sco X-1, Cyg X-1, Crab Nebula, Bright Transients etc that may give a count rate of about 10 k per sec or more, use time tagged photon data for variability and spectral studies.

On-board Purification:

Each of the LAXPC detectors will have an onboard gas purification system. This system will be operated as and when required to purify the gas filled in the detector by command. Since operating power required for purification system is large, all the three LAXPC detectors as well as their associated processing electronics will be powered down before gas purification system is powered on.

We have taken great care by keeping evacuated all the three detectors with the top cover for most of the time when detectors are not being tested. During last two months prior to ASTROSAT launch on 28 September 2015, we replaced top cover by nitrogen purging cover designed by ISAC team.

Bagging and Nitrogen purging of LAXPC:

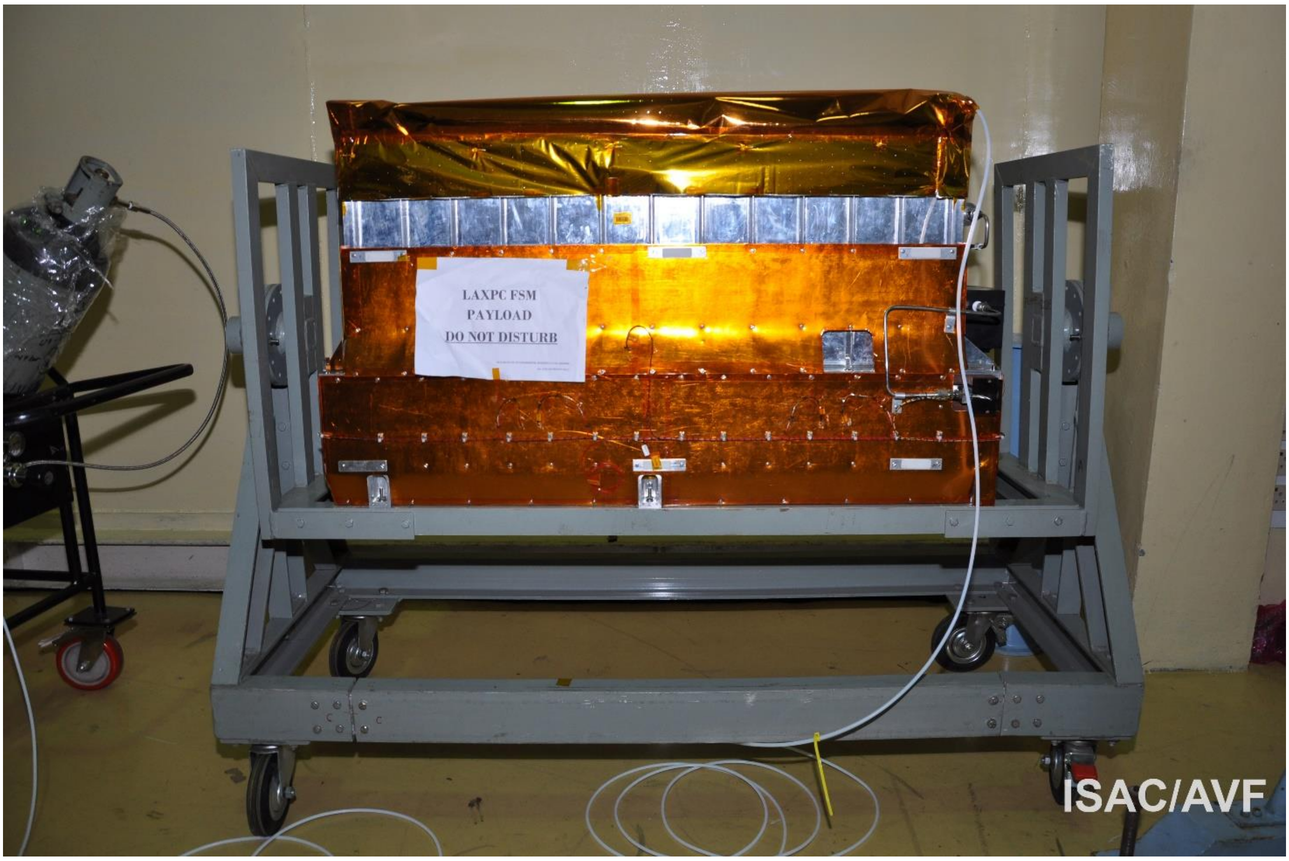

LAXPC flight Spare detector with Nitrogen purging arrangement in ISAC clean room

Each of the LAXPC detectors has an onboard gas purification system. This system will be operated as and when required to purify the gas filled in the detector when detector resolution deteriorates below threshold. It is expected that energy resolution of LAXPC detector will degrade as impurity increases. LAXPC10 detector was last purified in November 2013 (almost two years back) and was likely to absorb more impurities than the LAXPC30 which was last purified in October 2014 before final calibration in lab. All the LAXPC detectors were kept without cover many times specially for about 20 days at SHAR prior to the launch. *The purification systems were operated during 20-21 October and 24 November 2015 and the results are shown in figure next page. The purification system was operated for* LAXPC10, LAXPC20 and LAXPC30 detectors. The energy resolution of LAXPC10 detector improved after purification from 21% to 11% at 30 keV and from 16% to 9% at 60 keV. All the three LAXPC detectors have energy resolution 10-12% in the energy range 22-60 keV. We also observed CAS-A supernova remnant on 25 November 2015 to study energy resolution at lower energy, which shows ~20% energy resolution at 6.4 keV.

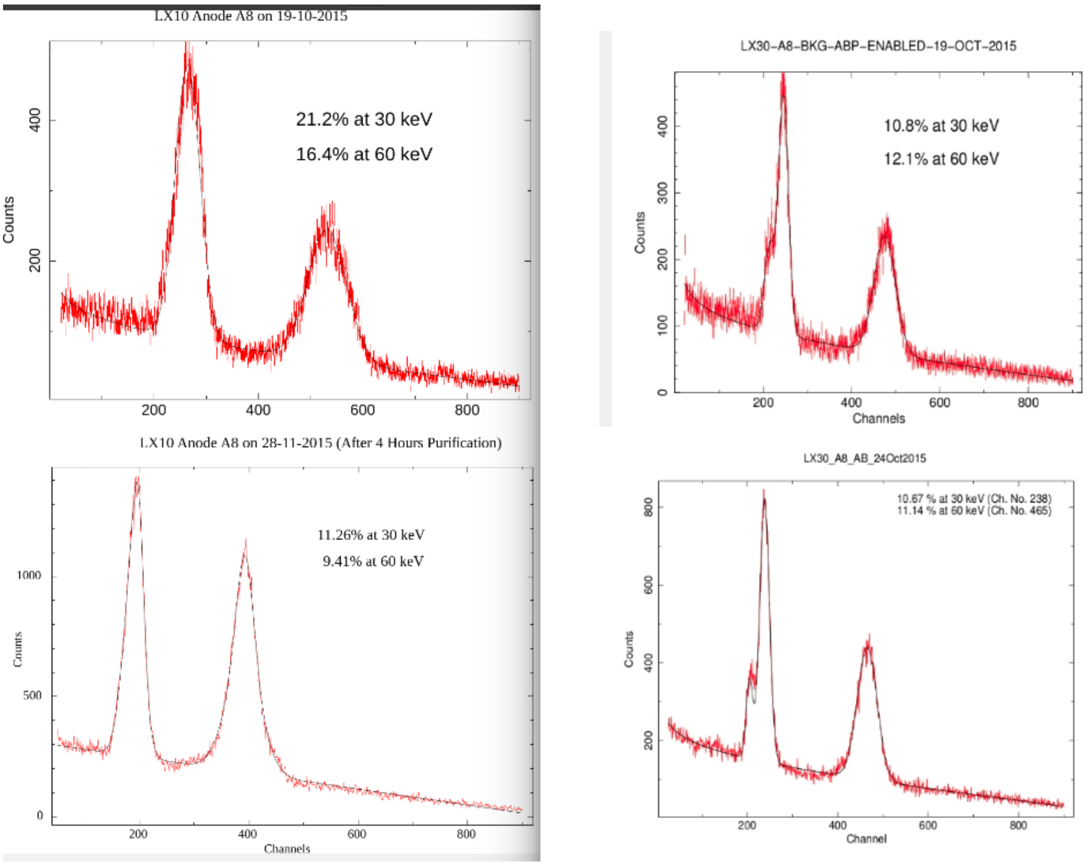

Improvement in energy resolution, after purification in orbit, measured with on-board calibration source

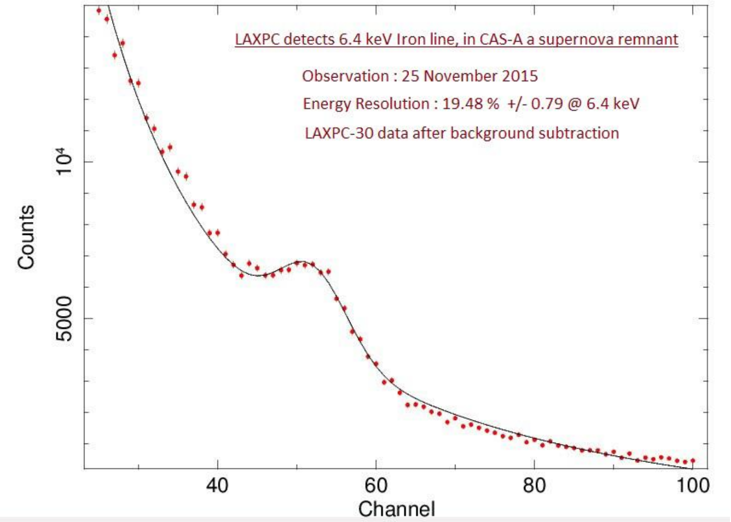

The observed spectrum for CAS A source with Iron line is fitted to estimate the energy resolution (Yadav et al. Proc. of SPIE (2016) Vol. 9905 99051D)

Calibration in orbit:

To determine the field of view of collimator we performed scan across the Crab X-ray source to find a FWHM value of about 0.9 degree. The scan was also used to estimate the offset in pointing between the Satellite axis and each of the 3 LAXPC detectors. The pointing directions for the three detectors are summarised in the following Table:

Detector	RA	Dec	offset
LAXPC10	83.78	22.01	0.15
LAXPC20	83.62	22.08	0.07
LAXPC30	83.74	22.03	0.11
Mean	83.71	22.04	0.09
Crab	83.63	22.01	

These offsets are expected to reduce the efficiency of detectors by 8-15% as determined from the scan. The ULD and anti count rate in orbit is about 1000 counts/s, which would also reduce the efficiency by about 5%.

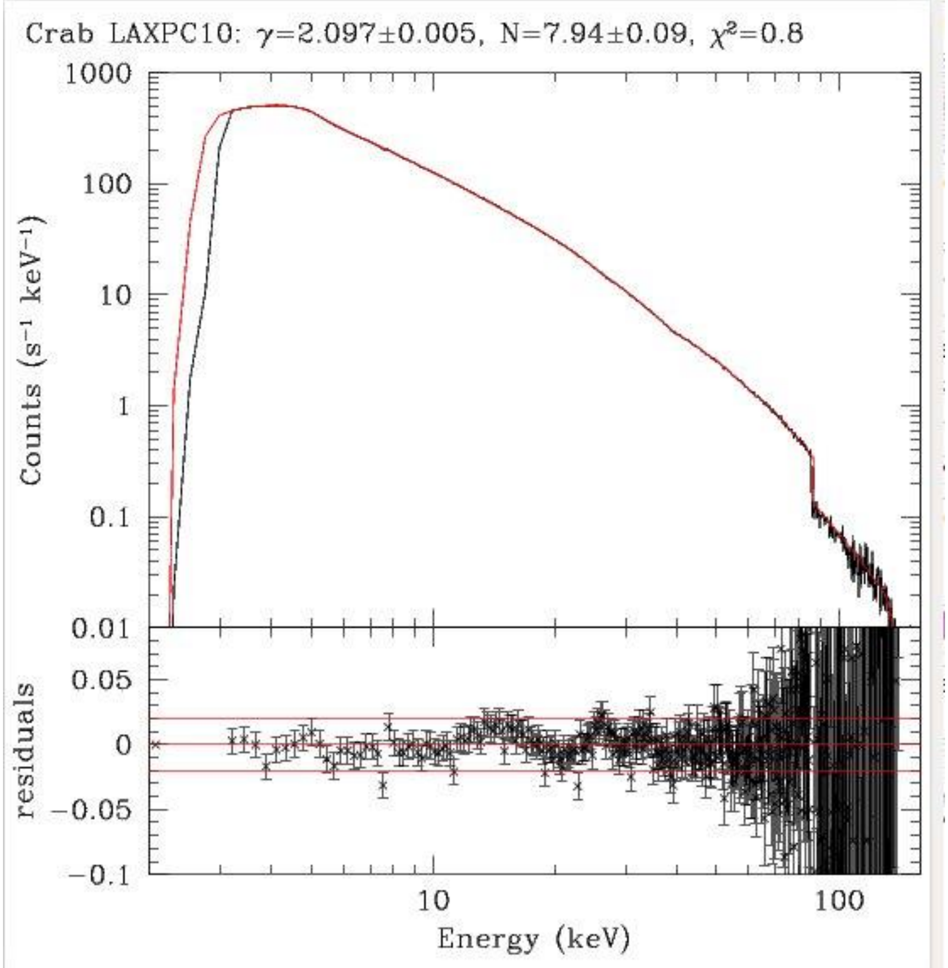

Fit to observed spectra of the Crab X-ray source in LAXPC10 using a power law model (Antia et al. (2017)http://arxiv.org/abs/1702.08624)

We observed crab during March 2016 and we have fit its energy spectrum in 3-100 keV energy range for LAXPC10 detector system with no systematics added. Results are shown in the figure above. This observation was used to fine-tune the response matrix for all three detectors.

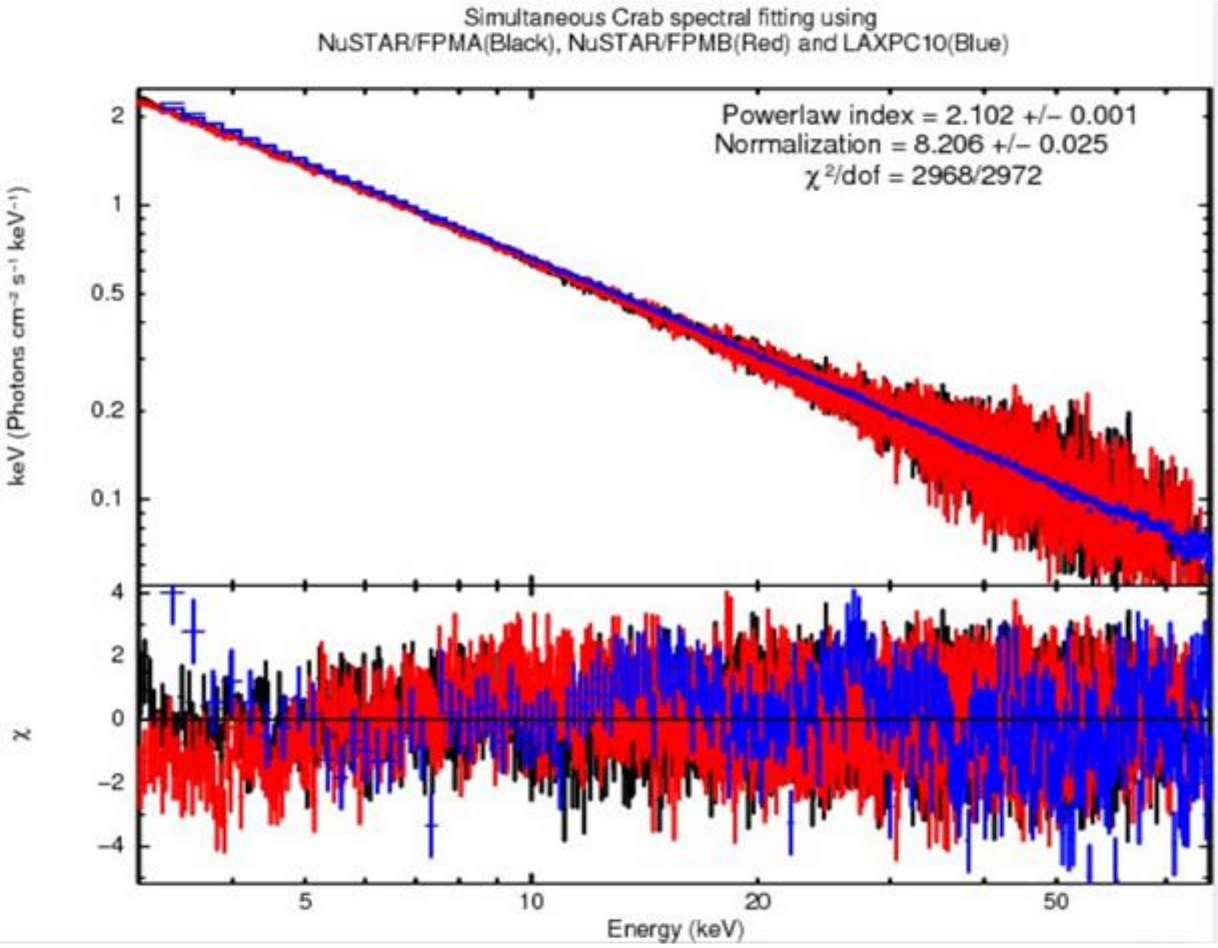

Fit to Crab data of LAXPC/AstroSat and Nustar observed simultaneously on 1st April, 2016 (Antia et al. 2017; http://arxiv.org/abs/1702.08624)

To determine the effective area we have carried out simultaneous observations of Crab with NuSTAR in April 2016 and simultaneous fits with the three LAXPC detector have been used to estimate the effective area. Simultaneous fit for LAXPC10 and Nustar for Crab data taken on 1st April, 2016 is shown in the figure above.

The reduced chi square is ~1 for a power law index ~2.102 and normalization ~*8.206*. The detection efficiency of Nustar drops fast above 30 keV which is reflected in large spread in data for energy > 30 keV. We have used these observations to correct effective area of LAXPC instrument.

Status of LAXPC instrument:

To monitor the long term stability of LAXPC detectors, the peak position and energy resolution of 30 and 60 keV peaks in the veto anode A8 from the on-board radioactive source is monitored regularly. The figure shows the peak position and energy resolution of the two peaks as a function of days after launch of AstroSat. The sharp steps in the variation are due to purification of gas and adjustment of high voltage. The gain of LAXPC30 has been constantly shifting due to a leak. As a result, the high voltage for this detector is regularly adjusted and around 22 January 2018, it is expected to reach the lowest possible value. After that it will not be possible to control the gain. The 30 keV peak had shifted by up to 85 channels (out of 1024 channels) before the high voltage was adjusted downward for the first time on 17 March 2016, after the leak was confirmed. During October to December 2015 the shift in gain of LAXPC30 was small and comparable to that in LAXPC10. This gain shift has to be accounted for in the response matrix and these have been generated for different amounts of shift and for different densities for LAXPC30.

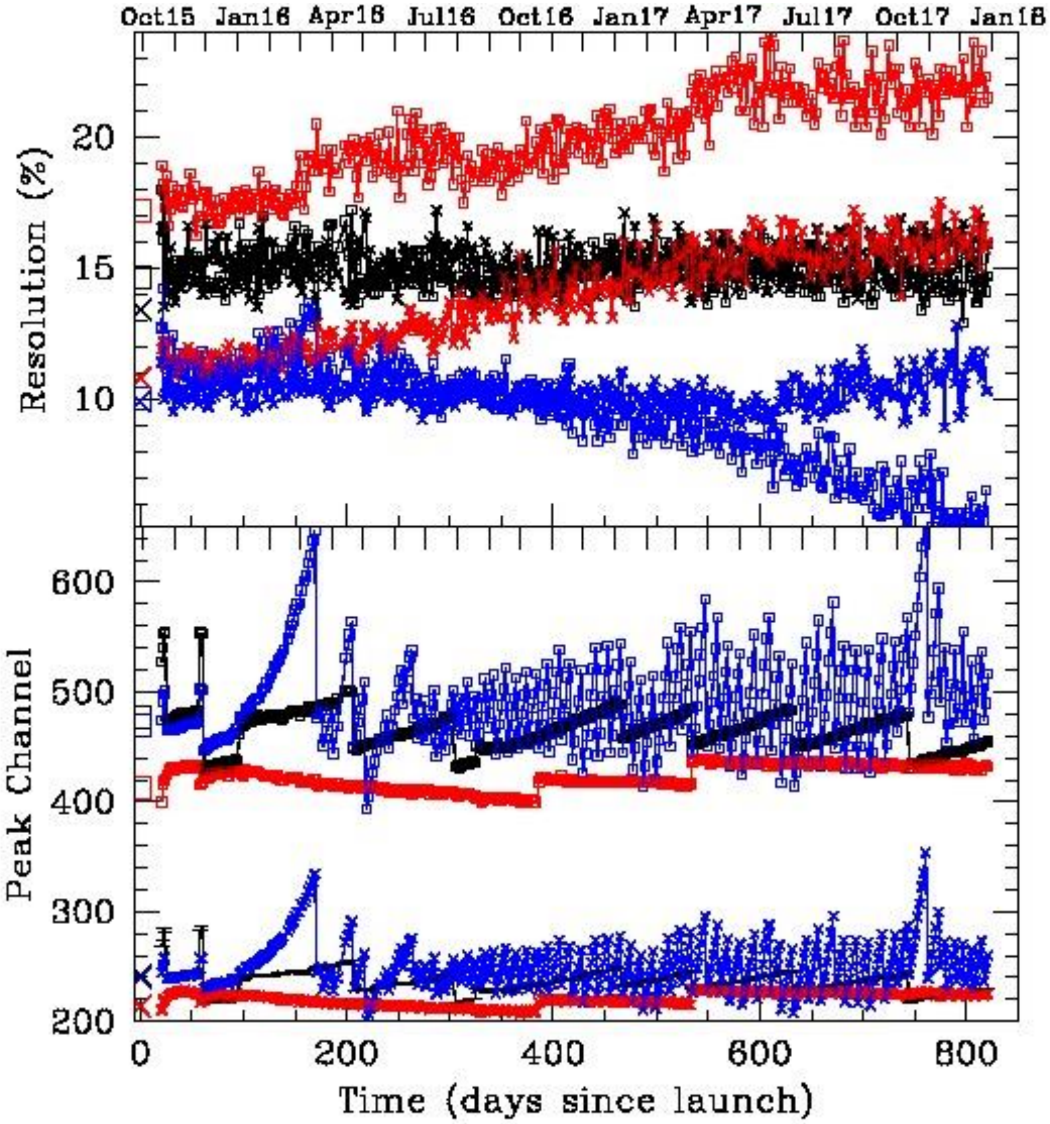

The peak position and energy resolution of 30 and 60 keV peak as a function of time for all 3 detectors as obtained from veto anode A8, which has the calibration source. The black, red and blue lines respectively, show the results for LAXPC10, LAXPC20 and LAXPC30. The crosses show the results for 30 keV peak and the open squares show those for 60 keV peak. The points at t=0 show the values during ground calibration.

We have used the on-board pressure gauge as well as observations of standard sources to estimate the density of the gas inLAXPC30 and the results are shown in the following figure. We have also used the observed counts in 60 keV peak from the calibration source in veto anode A8, which is expected to be proportional to the gas density. Similarly, the background counts near the upper energy threshold have also been used to estimate the density. Once the density reduced below about 30% of the original value the low energy photons just below the Xe L-edge are not fully absorbed in the top layer and the count rate in this layer shows a dip around 4.5 keV. To detect this dip we take the ratio of source counts (after subtracting the background) in layer 1 to the total counts for a bright source. This dip can be calibrated using responses at different densities to get the density. Till about June 2017, the density appeared to be decreasing linearly with time at a rate of about 5% of the original value per month. More recently there is some sign of reduced rate, which is most clear in the estimate using Xe L-edge, which shows an exponential profile with a e-folding time of about 200 days. It is now difficult to estimate the density reliably as various estimates give different values between 3-9% of the original density as of late December 2017.

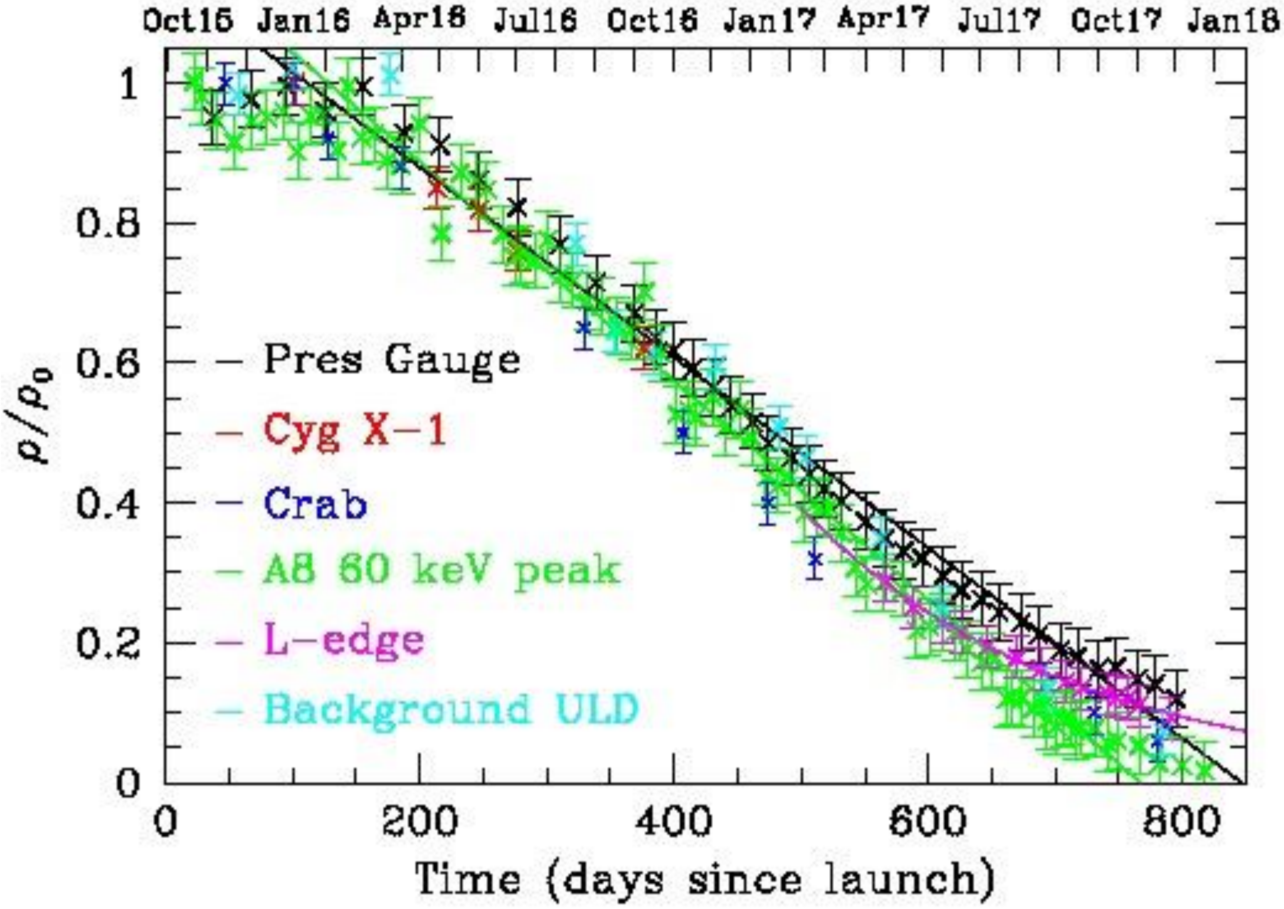

The density of gas in LAXPC30 detector as a function of time using different techniques. The lines show fits to some of these.

The reduction in density reduces the effective area of the detector and the following figure shows the effective area of the LAXPC30 detector with different densities, as estimated using a GEANT4 simulation. The reduction in effective area is most significant at high energies. It can be shown that even with a density of 4% of original value, the counts for Crab source will reduce by only about 30%. However, due to our inability to estimate the density reliability it is difficult to interpret these results and it is not advisable to use LAXPC30 data for most purposes since October 2017. This will reduce the total effective area of LAXPC detectors by a factor of 2/3. From February 2018 it will not even be possible to control the gain of this detector and it will be even more difficult to use these data, except for qualitative purposes of checking for any abnormal variation seen in other detectors.

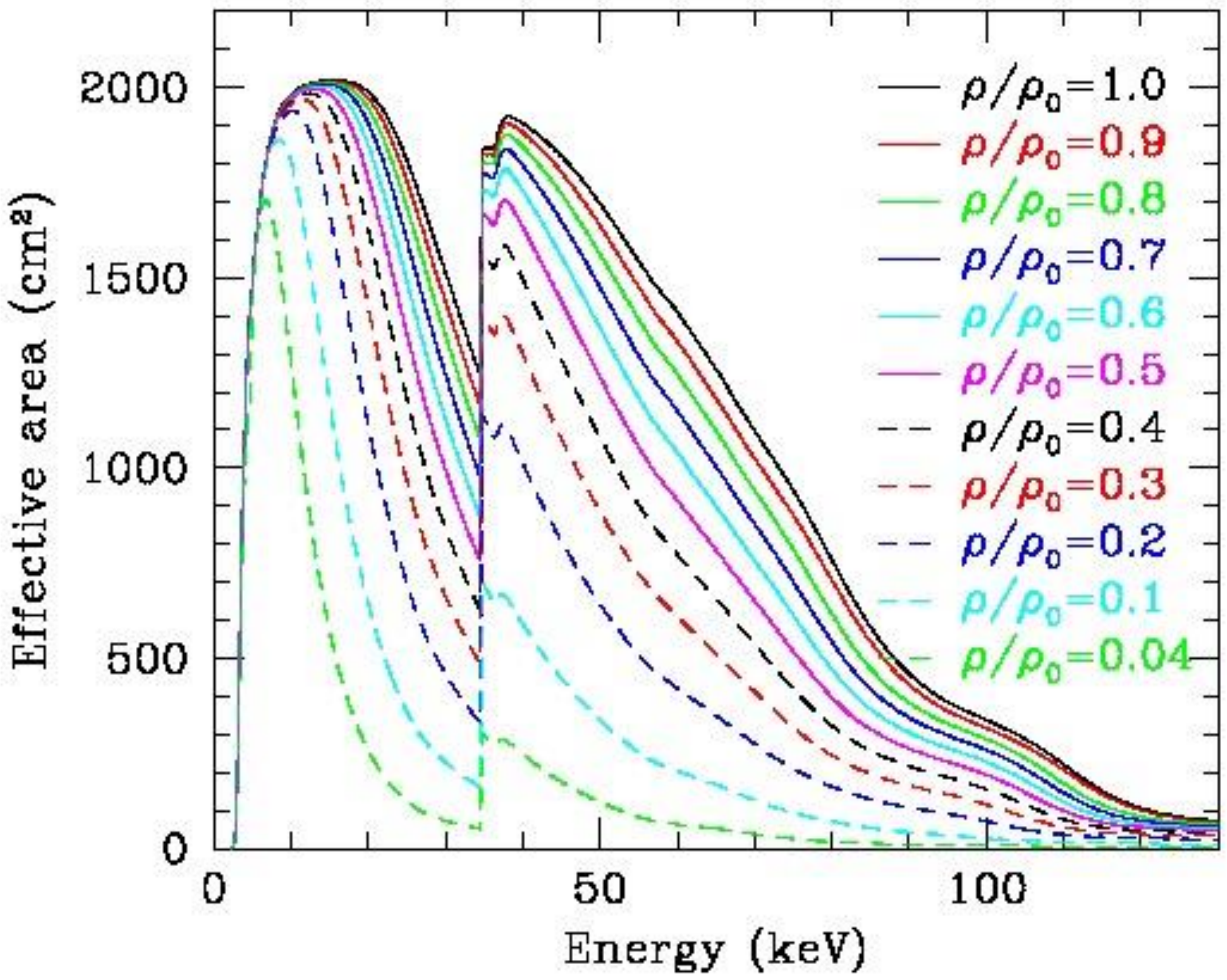

The effective area of LAXPC30 with different values of density. The values are in units of the original density.

It is not known till what density the detector can be operated. However, since August 2017 the background in LAXPC30 has increased at energies below about 10 keV and it varies with the detector gain. Further, the background has been increasing with time and as of late 2017, the increase can be by about a factor of 10. The following figure shows background in all 3 detectors at different times. The various green lines for LAXPC30 show the background during August-September 2017 while the highest curve is for 25 December 2017. It is difficult to predict how this trend will continue in future, but it is expected that after January 2018, when the gain starts drifting upward the background will start decreasing and may settle to a profile close to earlier profile at low energies. By end of March 2018 the gain may increase so much that the 30 keV peak may be beyond the current upper energy threshold.

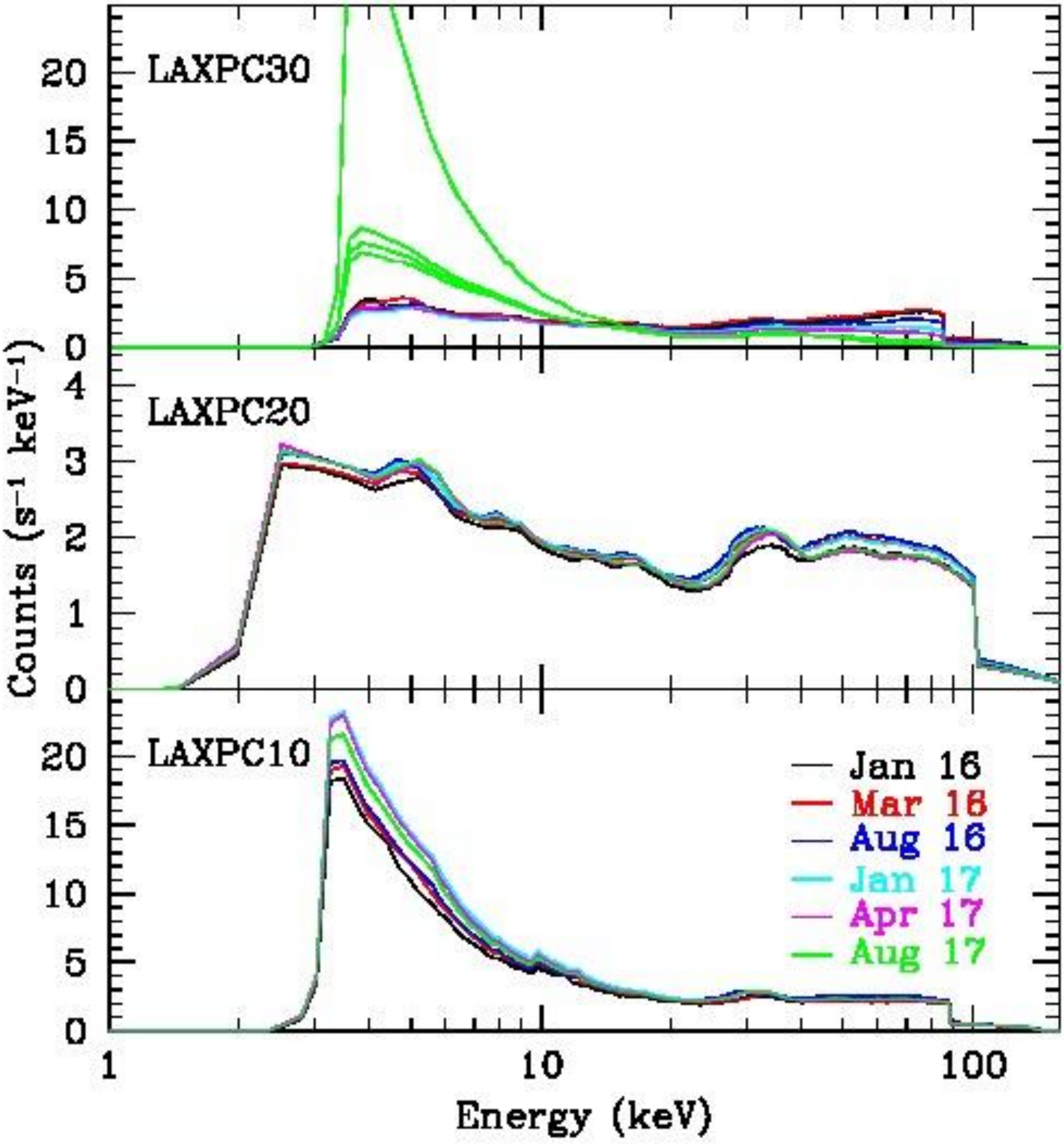

The background spectrum in different LAXPC detectors observed at different times. The green lines in the top panel show the spectrum for different observations during August-September 2017 while the highest curve is for 25 December 2017.

The gain in LAXPC10 is also shifting steadily upwards and the high voltage for this detector is also adjusted regularly. This could also be due to a fine leak which has been there, since launch. However, the rate of shift in this case is more than an order of magnitude smaller as compared to LAXPC30 and if this rate holds the detector could function for several years. No significant change in density has been detected for LAXPC10 so far. For LAXPC20 the gain has been slowly shifting downwards, which is the expected behaviour due to impurities accumulating in the detector. The energy resolution of this detector is also deteriorating with time. The gas purification was attempted three times after launch, but it has had little effect on the energy resolution. More recently, the gain as well as the resolution of LAXPC20 appears to have stabilised. For LAXPC10, last purification on 18 August 2016, shifted the gain as expected, but the energy resolution did not improve. Nevertheless, the resolution of LAXPC10 appears to be stable for the last 2 years. The resolution in LAXPC30 has improved with time, presumably due to lower pressure, but has stabilised now.

For all detectors the background has been changing with time. Some of this variation is due to shift in gain, which can be corrected to a large extent. Even after this correction the background count rate has increased with time till mid-2016. After that it has decreased a little. The variation in LAXPC10 is larger than that in LAXPC20. After accounting for this secular variation there is still a residual fluctuation at the level of five counts/sec in all detectors. This is most probably due to variation in charged particle flux with time which limits the sensitivity of LAXPC detectors. During the time of geomagnetic disturbances, even minor ones, the situation can be worse. It may not be possible to study sources fainter than about 1 mCrab, irrespective of the observing time.

The software and responses for analysing LAXPC data are available at
http://www.tifr.res.in/~astrosat_laxpc/LaxpcSoft.html

Chapter 5

Cadmium Zinc Telluride Imager

The Cadmium Zinc Telluride Imager (CZTI) is one among the four X-ray instruments on ASTROSAT. It is a hard X-ray imaging instrument covering the energy band from 10 to 100 keV, has a detector area of 976 cm^2 constructed using CZT modules and uses a Coded Aperture Mask (CAM) for imaging.

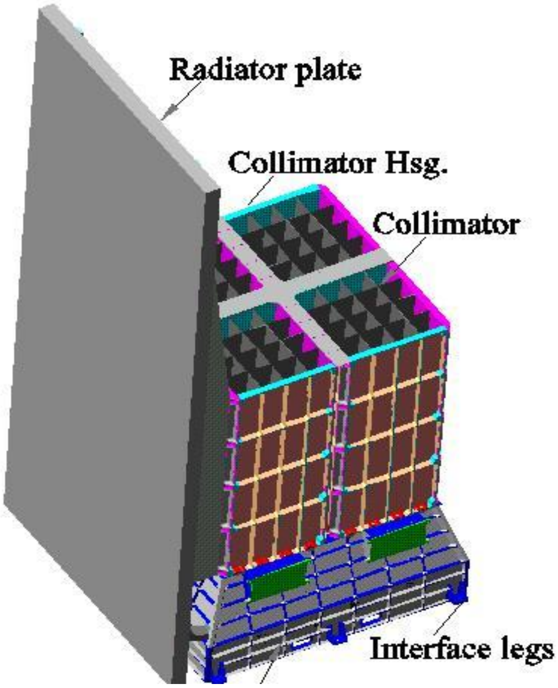

Figure 5.1: The Cadmium Zinc Telluride Imager (CZTI)

The characteristics of the CZT-Imager are given in Table 5.1 (Figure 5.1). The total detection area of 976 cm^2 is achieved by the use of 64 CZT modules of area 15.25 cm^2 each. These 64 modules are arranged in four identical and independent quadrants. The overall dimensions of the CZTI are shown in Figure 5.2 and the orientation reference is shown in Figure 5.3. The CZT detector is interfaced to a radiator platewhich maintains an operating temperature of 0 to 15deg Celsius by passive cooling. The instrument is mounted on the satellite deck with the radiator plate looking in the direction of the satellite +Yaw axis. Collimators above each detector module restrict the Field of View to 4.6° x 4.6° (Full Width at Half Maximum) at photon energies below 100 keV. At energies above that the collimator slats and the coded mask become progressively transparent. For Gamma Ray Bursts, the instrument behaves like an all-sky open detector.

The CZTI carries a Cesium Iodide (Tl) based scintillator detector operated in anti-coincidence with the main CZT detector and it is called the Veto detector. This is located just under the CZT detector modules. Further, there is a gap of about 8 cm between the base of the collimator slats and the detector plane, in order to accommodate a radioactive calibration source module in each quadrant. This source shines alpha-tagged 60 keV photons on the CZT detector in order to help calibrate the energy response.

The science objectives of the CZTI include the measurement of curvature and reflection components in the spectra of Active Galactic Nuclei and X-ray binary systems, the study of Quasi-Periodic Oscillations at hard X-ray bands in accreting neutron star and black hole systems, cyclotron line spectroscopy of high mass X-ray binaries, the characterization of hard X-ray spectra of magnetars as well as the detection of gamma ray bursts and the study of their early light curves. Polarization measurement of gamma-ray bursts and bright (> 500 mCrab) sources in 100 – 300 keV region is an additional objective of CZT Imager.

Table 5.1: Characteristics of the CZT-Imager

Area	976 cm ^{2}
Pixels	16384 (64 modules of 256 pixels each)
Pixel size	2.46 mm X 2.46 mm (5 mm thick); edge row pixels are 2.31 mm wide instead of 2.46 mm
Read-out	ASIC based (2 ASICs per module)
Imaging method	Coded Aperture Mask (CAM)
Field of View (10-100 keV)	4.6° X 4.6° FWHM (primary FOV) 11.8° X 11.8° FWZM (incl. Illuminationleakage)
Angular resolution	~ 8arcmin (18 arcmin geometric)
Energy resolution	~ 6% @ 100 keV
Energy range	10 – 100 keV Up to 1 MeV (Photometric); limited imaging above 100 keV
Sensitivity	0.5 mCrab (5 sigma; 10^4 s)
Memory	50 Mbytes per orbit

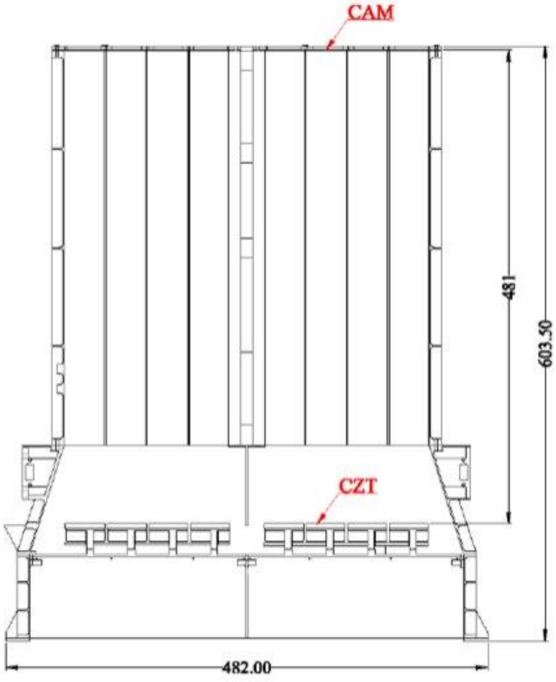

Fig 5.2: Overall Dimensions of the CZT-Imager

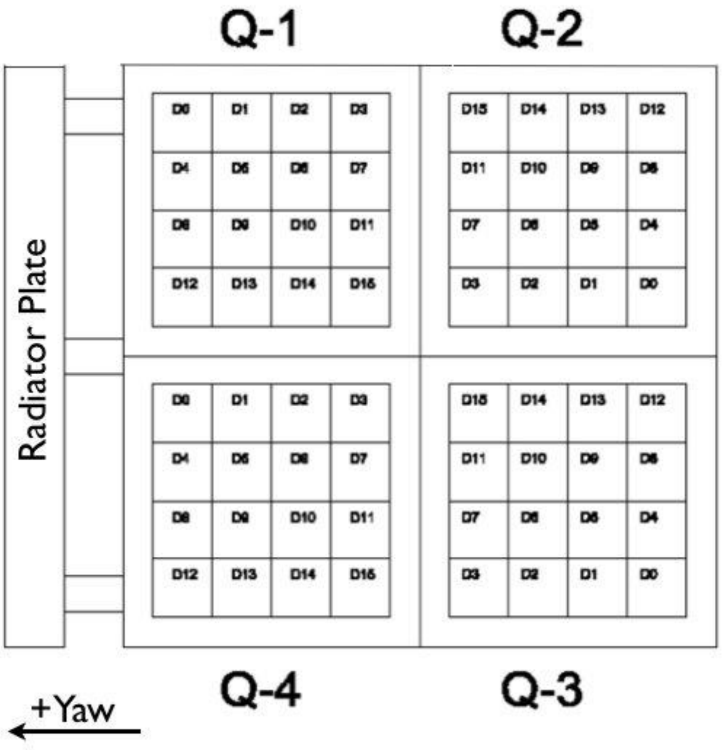

Fig 5.3: Orientation of the CZT-Imager and the reference nomenclature of the four quadrants. The x-axis of the detector plane is identified with the negative Yaw axis of the satellite.

The CZT Imager payload is divided into two packages: CZTI detector box and CZTI Processing Electronics. The detector box houses the detectors with front end electronics and all mechanical interfaces including CAM, cooling arrangement etc. The four quadrants are electrically independent and communicate, digitally, only with the Processing Electronics (PE) box. The PE handles all interfaces (including detector interface) and houses the onboard software designed for the optimum performance of the payload. The basic details of these two packages are given in Table 5.2.

Table 5.2: CZTI Package details

	CZTI Detector Box	CZTI Processing Electronics
Weight (kg)	50	3.2
Size (mm)	482X458 X603	263X256X69
Power (W)	70	3
Operating temperature	0 – 20 °C	0 – 40 °C

Detector Module Details

The CZT-Imager detector box contains Cadmium Zinc Telluride as the main X-ray detector and a CsI (Tl) crystal is used as a veto detector for background reduction. In addition to these two detectors an alpha-tagged X-ray source is also used for calibration purposes (Rao et al. 2010, NIMA, 616, 55). The Front-end electronics in the detector box handles the outputs from these detectors for further analysis while low voltage and high voltage supplies provide the necessary power and biasing voltages to the detectors. A passive collimator (FOV of 4.6° X 4.6° FWHM) helps in allowing nearly parallel X-rays to enter the detector. A Coded Aperture Mask (CAM) made of tantalum is positioned above the collimator.

a. The basic detector module is a CZT crystal of size 39.06 mm X 39.06 mm and 5 mm thick. It is pixelated by contact points on one side with a pixel size of 2.46 mm X 2.46 mm, except for edge rows which are 2.31 mm wide. The edge pixels are thus 2.31mm x 2.46 mm in size, and the corner pixels are of size 2.31 mm X 2.31 mm. One detector module thus becomes an array of 16 X 16 pixels of CZT. The overall geometric area (976 cm^2) of the instrument is achieved by using 64 detector modules divided into four quadrants, eachquadrant containing a 4 x 4 matrix of detector modules mounted on the Detector board.

   Each individual pixel is connected to a pre-amplifier, which is embedded in an Application Specific Integrated Circuit (ASIC) containing 128 channels. Two ASICs are situated just behind the detector wafer. The X-ray detector has a detection efficiency of 95% within 10 - 120keV and good energy resolution (~ 6 % at 100 keV).The ASIC is a fully data-driven charge signal acquisition chip. It provides digital output corresponding to the detected X-ray energy and digital address of the incidental pixel.

b. The veto detector is a CsI (Tl) scintillator of size 167 mm X 167 mm and 20 mm thickness viewed by two one-inch Photo-multiplier tubes (PMT) positioned on two sides of the crystal. Minimum detection sensitivity is 50 keV for incident photons. The CsI detector requires High Voltage (HV) of the order of 800 V, which is generated by the electronic circuits in the Crystal Holder.

c. Another CsI (Tl) 10 mm cube crystal viewed by a photodiode of 10 mm square area and embedded with a radioactive source Am^{241} is placed on top of the CZT detector. At every disintegration of an Am^{241} nucleus, a 60 keV photon is generated, accompanied by an alpha particle of energy of about 5 MeV. The alpha particle is absorbed in the small CsI (Tl) detector whereas the 60keV X-rays escape from this detector and in a very substantial number of cases interact in the CZT detector. The alpha particle gives a light pulse in the CsI (Tl) crystal which in turn is converted into an electrical pulse at the output of the photo-diode. Any output in the CZT detector coincident with the pulse output from the CsI (Tl) detector is deemed to be originating from a 60 keV photon. This method is used to calibrate the CZT detector for its energy response.

Mechanical and Thermal Design

The mechanical parts of the CZTI consist of the following:

CZTImager Housing

The housing is made out of blocksofAluminum alloy to increase the integrity of the payload. It has an overall dimension of 482 mm x 482 mm and 195 mm height. All peripheral walls (vertical & slant) of the housing are configured with suitable ribs and minimum wall thickness. The top half of the housing has circumferential as well as central flanges which are suitably stiffened by providing gussets and stiffeners to withstand load coming from collimator housing which will be integrated on this.

Crystal Holder

CsI crystal holder is a sub-assembly interfaced with the Detector housing and it accommodates (1) the CsI crystal (2)aPower Card with HV DC-DC, pre-amplifier and power electronics**.** The CsI crystal is mounted on top of the housing and is held by a clamp specially designed for it. The Power card is assembled on the rear side of crystal housing.

Detector Board Assembly

The Detector Board consists of a PCB to mount the 16 detector modules, Front-end Electronics Board (FEB), and a specially designed Internal Radiator Plate which acts as an interface between the detector modules and the heat pipes so that uniform temperature is maintained across all detector modules.

Functions of detector board assembly:

- Holding the CZT detector modules in a specified format.
- Providing interface to the Detector housing.
- Providing interface to the Calibration housing.
- Providing interface to the heat pipes.

Radiator Assembly

The CZT modules perform best in a temperature range of 0° C to 15° C. To achieve this temperature, the heat produced by CZT module (300 mW/module) is drained continuously by the radiator assembly, which consists of (i) Heat pipes (3 nos.) (ii) Radiator plate and (iii) Spacers & clamps. The radiator plate area required to radiate the total power of 50 W is about 7000 cm^2.

Collimator

The Collimator plates are made of 0.07 mm thick Tantalum sheet sandwiched between 0.2 mm thick precisely machined Aluminum alloy plates, providing a collimation of 4.6° X 4.6° FWHM directly under the collimator. However since a gap of 100 mm is left between the bottom of the collimator and the detector plane to accommodate the calibration housing, a certain amount of illumination leakage occurs from one collimated module to its adjacent neighbors. When this illumination overlap is taken into account, the net field of view works out to be 11.8° x 11.8° FWZM.

Collimator housing

The Collimator housing is a hollow structure, configured quadrant wise, with a single quadrant 167.5 mm x 167.5 mm x 400 mm, made up of four aluminum alloy side plates, which are integrated side-by-side using M4 fasteners.

The Coded Aperture Mask

The design of the CAM for the CZTI is such that the size of the mask plate is the same as that of the detector itself. The mask is made of a 0.5 mm thick Tantalum plate in which a pre-determined pattern of holes is cut to allow X-rays to pass through. The Coded Mask forms the topmost part of CZTI payload. It is coded by open and closed pattern of squares/rectangles matching the size of the detector pixels. Additional support bridges of thickness 0.2mm are introduced at a number of places within the pattern to improve its mechanical stability. In such a design (called a ‘box-type’ or ‘simple’ system) exposure to the full mask pattern is not possible anywhere except exactly at the middle of the coded field of view. At all other angles only a part of the shadow of the mask falls on the detector. The patterns are based on 255-element pseudo-noise Hadamard Set Uniformly Redundant Arrays. Of sixteen possible such patterns, seven were chosen on the basis of the mechanical support for individual pixels in the pattern. These seven patterns, with some repeats, were placed in the form of a 4 x 4 matrix to generate the CAM for one quadrant. This same pattern is placed on other quadrants, rotated by 90°, 180°and 270° respectively.

CZTI Detector Electronics

The CZT detector box electronics consists of

1. The front end electronics for CZT module.
2. Pre and Post amplifiers for Veto detector Cesium Iodide {CsI (Na)}.
3. Pulse height (PH) analyzer for Veto.
4. Alpha source detector CsI (Na).
5. Logic circuits to handle the data.
6. The high voltage DC/DC converters.
7. Interface circuitry for communication with CZTI Processing Electronics.

The front-end electronics is made into four identical quadrants. All analog electronics is housed in the detector box itself and it contains ASIC control, amplifiers etc. Apart from Detector Board, Alpha card and the Power Card, there will be one electronics card per quadrant called the FEB which includes ADCs, digital control and FPGA.

Basic Design

One CZT module contains 2 ASICs and hence one quadrant will have 32 ASICs daisy chained to each other.A list of major components of CZT Detector electronics is given in Table 5.3.The detector assembly consists of the array of Detector Modules which is an integrated unit of CZT detector and ASICs, procured from Orbotech Medical Solutions, Israel. The detector assembly contains a Detector Board with 16 CZT Modules with 32 ASICs daisy chained. An aluminized Mylar sheet of 50 micronthickness is kept on top of the detectors to provide thermal isolation.

Table 5.3 List of Major Components of CZT-Imager Quadrant

Name	Components	Mechanical Location
CZT Detector Assembly	Detector Modules Detector Board Internal Radiator FEB	Detector Board Assembly
HV-CZT	Pico DC/DC	Detector Board Assembly
Veto Detector	CsI(Tl) + 2 PMTs	CsI Assembly
HV-Veto	HV DC/DC (800V)	CsI Assembly
Alpha Tag	Am (241)	Alpha-Box

Veto Detector

A detector (CsI) covers the large area of 256 cm^{2}and the light collection is done using two photomultipliers (PMT), viewed from sides. On registering an event, a signal from the detector is sent to a pre-amplifier. This signal is processed and sent to the FEB for further analysis. After amplification of the signal from pre-amplifier, the signal is sent to a comparator via stretcher along with LLD level signal. If LLD is triggered the pulse is digitized to an 8-bit output by ADC through control circuit. This output is used to differentiate Compton scattered events and hence the background in main detector can bereduced.

Power Card

The Power card, positioned in the Crystal Holder, has a Pico high voltage generator for biasing the veto detector. A positive high voltage around 800 V is used to bias the Photomultiplier tubes attached to Veto detector. Similarly another negative high voltage, from another Pico DC/DC converter, is used to bias the CZT detector. The Power Card also generates appropriate regulated low voltages for the CZT modules and it also houses the amplifiers for the CsI detector.

Alpha - Tag

A calibration source of Am (241), is kept to shine over the detector. An energy of 60 keV is released from the source along with an alpha particle simultaneously. This alpha particle gets detected in the CsI (Tl) detector volume which generates the signal. The photodiode which is coupled to this CsI (Tl) detector generates an electrical pulse, which is amplified in pre-amplifier and post-amplifiers. Post-amplifier signal is fed to an analog comparator along with lower-level discriminator level. A relevant digitized signal generated with help of Monoshot is passed on to FPGA as an alpha-tag event.

Front-end Electronics Board (FEB)

The FEBcontains interface circuits required for the CZT modules. A FPGA is used to handle the signals from the three different detectors (CZT, Alpha and CsI Veto) and data is stored in a memory to be transmitted to PE, every second. The coincidence among different detectors are done digitally by ground data processing.

Processing electronics

The Processing Electronics (PE) is housed separately and it contains an FPGA with an embedded processor. The PE controls all satellite interfaces, detector interfaces and it handles onboard memory and data management.The functions of the processing electronics includes reading, analyzing, storing and/or transferring detector data to satellite via data formatter. Also it controls the FPGA in the FEB using 16-bit serial commands.

There are two types of memories, namely

a. RAM: This holds all types of data like detector data and commands, telecommands and telemetry data.
c. EEPROM: This holds the basic software and the default parameters. Initially all parameters arecopied from EEPROM and then any changes sent by telecommands are stored only in the RAM.

About FPGA: this is mainly a hardware compressor, in that it compresses the overall hardware into one single chip. This handles the following functions:

a. Timer.
b. Detector communications.
c. Telecommands.

During an event in the detector package, the same is analyzed and stored in one of its ping-pong memory, by its FPGA. The CPU interrogates the detector FPGA every 1 second. Upon receiving this signal the FPGA stops storage in the first of its ping-pong memory, resumes storage of data in the second memory and, upon command from the CPU, transfers data from the first memory to processing electronics. This FPGA based data are stored directly into a pre-determined space in the CPU memory. Data from all the 4 quadrants are read simultaneously (the entire data transfer at 500 kHz takes about 131 ms). The CPU then starts analyzing the stored data according to its operating mode.

Data Organization in Detector Package

The detector package contains a FPGA to analyze data from ASICs, store it in its RAM andsend it to the electronics package. All the ASICs are daisy chained hence the inputs and outputs of all 32 ASICs in a quadrant are controlled by a single FEB.

Modes of Operation

The CZTI can operate in 16 possible modes. Fifteen of these are primary modes, and there is one Secondary Spectral Modewhich runs in parallel with other primary modes. But, in normal course of operation data are acquired in only three of them: Normal Mode, Secondary Spectral Mode and SAA mode. The description of these modes are as follows:

Normal Mode:

This mode transmits complete raw data received from the detector box. This takes up 144 Mbytes per 100-minute orbit. This is the default mode of operation of the CZTI.

SAA Mode:
When the detector is in the South Atlantic Anomaly (SAA), or if both the CZT and the Veto High Voltage supplies have been turned off by ground command, only header data is transmitted directly from the event frame. The header data of each second is extracted and compiled into one quadrant header packet every 100 seconds.

Shadow Mode:
The Shadow Mode is selected if the Earth Shadow Entry command is sent from ground. In this mode the header data of a 100-s window is sent at the 100-s boundary. The Frame/packet format is similar to the SAA mode. Each frame contains only one packet.

Secondary Spectral Mode:
This mode runs in parallel with any other selected mode. The on-board software prepares the spectral data of each quadrant every second. The integrated spectra so prepared is packetized and sent to the Satellite Bus storage (Solid State Recorder) once every 100 seconds.

Reduced Data Modes

Reduced Data Modes can be entered either by ground command or due to limited memory availability. The following reduced modes of operation are available:

Fixed No. of Packets (FP):
The frame format here is similar to the normal mode but a fixed maximum number of packets are generated from each quadrant.

Veto Spectrum Disabled (VSD):
Packets are generated without the Veto Spectrum.

Two word event report (2WE):
The number of words representing each event is reduced from 3 (as in normal mode) to 2, by sacrificing some resolution in time and energy.

Memory Management (MM):
The behavior of Memory Managed modes depends on the level to which the payload memory is occupied due to the Satellite Bus storage allocated to the CZTI being full. At different levels, Full data, only Secondary Spectral Mode data and Header data or the Header data alone could be recorded. Beyond a certain level no data is recorded.

A number of combinations of the reduced modes are possible, e.g., SAA+Shadow, VSD+2WE, VSD+FP, FP+2WE, FP+2WE+VSD, MM+SAA, MM+Shadow and MM+Shadow+SAA.

Data Interfaces

The two main interfaces are namely:
1) Detector Interface.
2) Satellite Interface.

Detector Interfaces:

The unit's interface with the detector electronics unit involves the following:

Event Interface:
The FPGA of each quadrant reads data from the detectors, arranges it in the form of a 2 x 2 Kbytes frames. This is read periodically by the processing electronics every 1 second. This data is then further analyzed and accumulated or transmitted to the satellite via data formatter.

Command Interface:
The Command interface with the detector unit is done serially with clock & data lines.

Satellite Interfaces:

The unit's interface with the satellite involves the following:

Power Interface:
The raw power is routed through a relay, which is switched ON/OFF by command from ground followed by a series of transfers to the motherboard. There are two separate lines for main & redundant power.

Command Interface:
There are 13 Pulse commands & one 32-bit data command with the facility of sending data commands in a time-tagged mode.

Telemetry Interface:
This interface is to a Solid State Recorder (SSR) via a data formatter. Data is sent periodically, typically every 8 ms, to the formatter in the form of 2 Kbytes frame at 2MHz clock rate.

Background Estimation

The sources of background in the CZT detector are primarily cosmic diffuse gamma rays and gamma-rays originating from the satellite structure (spallation background) due to the interaction of cosmic rays.

To distinguish these background counts from the real source counts a slab of CsI is placed under each block of CZT. The high energy photons which deposit energy in CsI as well as CZT are rejected by anti coincidence techniques and hence do not contribute to the background counts in CZT. Only the photons which deposit partial energy in CZT but do not interact in the CsI block generate background counts in the (10 - 100) keV region.

Compton Induced Background

Assuming an outer space environment where the satellite is deployed, some of the background count estimates have been simulated and the values are described here. The total number of background counts in the CZT due to single Compton scattering are calculated by summing up all the contributions over the entire energy range of injected gamma rays and the typical counts are about 20 counts/sec for CsI thickness of 2 cm.

Fluorescent K-alphaBackground

Cosmic diffuse gamma ray photons in the energy range (10 - 100) keV interacts with Tantalum by photo-electric effect and produce fluorescent Kα X-rays. The fluorescent X-ray contribution to background contributions can be divided in 3 parts:

(a) Contribution from the top surface,

This surface is made up of Tantalum of thickness 0.5 mm. The total area of a module is 15.25 cm^2 but the effective area is half that due to the random holes of the CAM. It is far from the detector and subtends a small solid angle at the detector plane. The total counts from this surface are about 0.0025 counts / sec.

(b) Contribution from 4 cm x 36 cm upper side surfaces.

This side is made of Tantalum sheet of area 4 cm x 36 cm and thickness 0.1 mm. Though this surface is large compared to the detector surface, it is perpendicular to detector plane and makes a small solid angle to the detector. The total count from this surface is about 0.41 counts / sec.

(c) Contribution from 20 cm x 14 cm lower side surfaces.

This is the lower portion of the side surface and as it is closer to the detector it contributes the maximum. The numbers of counts at the detector depends very much on the height of the side surface. The total counts from this surface are about 5 counts/sec.

Data Analysis

Image Reconstruction

The standard procedure adopted for image reconstruction will consist of first binning the data to produce a detector plane image (DPI), which is then cross correlated with the mask pattern. Significant peaks from this image are picked and a least square fit is then made of the DPI with theoretically computed shadow patterns for sources these locations. This allows accurate determination of the intensities of these sources, and also helps identify and eliminate spurious peaks that might have been picked from the cross-correlated image.

Operation Sequence to generate the Data products

- Step 1: Download telemetry data for an observation period.
- Step 2: The good time interval file is generated using the house keeping information
- Step 3: Read the attitude information and generate average position of the satellite for the period of observation.
- Step 4: Extract the relevant data and generate the raw DPH or raw DPI.
- Step 5: The detector data (DPH) is processed to generate information about noisy and dead pixels for the time of observation.

- Step 6: Using information generated in steps 3 and 5, process the raw DPH/ DPI and clean them. Generate a detector mask file that records the pixels removed in the cleaning process.
- Step 7: Perform cross-correlation imaging and pick candidate sources from the image
- Step 8: Perform shadow fitting to estimate fluxes of candidate sources, reject insignificant candidates and iterate until all sources have fitted flux values above the detection threshold. (In generating shadow patterns for fitting the detector mask must be accounted for).

Ground Calibration of CZT Imager

The CZT detector modules, procured from Orbotech Medical Solutions, are meant for commercial use. To qualify these detectors for flight, a rigorous screening procedure was evolved. After the screening process, it was found that the yield was very low (about 65%). It was noticed that the number of noisy pixels increased after screening, resulting in the rejection of a large number of modules (acceptance criterion is that the number of dead+noisy+bad pixels out of the 256 pixels in a given detector should be less than 15). The CZT detector modules are primarily designed as gamma-ray devices (40 – 200 keV) to be operated at room temperatures. To extend the low energy response to 10 keV, the devices are cooled to 10°C (+/- 5°C) – but in some orbits the temperature can go up to 20°C.

The ground calibration of CZT-Imager payload was done in the following manner. Time tagging and polarization abilities are examined at individual module level. The assembled quadrants are calibrated at multiple temperatures to understand the spectral response at individual pixel level. The fully assembled payload is calibrated to understand the a) imaging behavior, b) veto tagging efficiency and c) alpha-tagging efficiency.

Characterization of individual pixels

Individual pixels are characterized as dead (D) pixels defined as pixels having no sensitivity to detect X-rays, noisy (N) pixelsdefined as pixels having counts more than 5-sigma above the mean and bad (B) pixelsdefined as pixels whose energy resolution is significantly worse as compared to the other pixels. The characteristics of the pixels are monitored regularly and each module is given a grade based on the number of dead andnoisy pixels and their degradation with time, based on the criterion given in Table 5.3.The distribution of the grades of 64 modules in the individual quadrants are given in Table 5.4 and it is found that 84% of the modules belong to Very Good or Good category. Noise is also found to be a function of temperature and energy threshold and the final energy threshold that can be achieved at various temperatures are given in Table 5.5 and the number of suppressed pixels are given in Table 5.6. It is found that a threshold of 10 – 15 keV can be achieved in a majority of modules with less than 5% of pixels being suppressed.

Table 5.3 Module grading criterion

	D+N = 0-10	D+N = 11-15	D+N = 16-20	D+N = 21+
Change <= 5	Very Good	Good	Fair	Poor
Change = 6-10	Good	Fair	Poor	Poor
Change >10	--	Poor	Poor	Poor

Table 5.4Distribution of module grades

	Very Good	Good	Fair	Poor
Quadrant 1	12	3	1	0
Quadrant 2	14	1	1	0
Quadrant 3	10	2	1	3
Quadrant 4	10	2	2	2
Total	46	8	5	5

Table 5.5Number of modules as a function of threshold for different temperatures.

Temperature (°C)	**Threshold**				
	10 keV	**11-15 keV**	**16-20 keV**	**21-30 keV**	**>30 keV**
-5	38 (59%)	20 (31%)	5 (8%)	1 (2%)	--
0	34 (53%)	19 (30%)	10 (15%)	1 (2%)	--
5	33 (52%)	17 (26%)	13 (20%)	1 (2%)	--
10	31 (48%)	16 (25%)	14 (22%)	3 (5%)	--
15	24 (38%)	8 (12%)	16 (25%)	9 (14%)	7 (10%)
20	--	--	21 (33%)	30 (47%)	13 (20%)
25	--	--	--	--	64 (100%)

Table 5.6 Number of disabled pixels

Temperature	**Number**						
	-5°C	**0°C**	**5°C**	**10°C**	**15°C**	**20°C**	**25°C**
Quadrant 1	100	100	102	111	131	139	152
Quadrant 2	76	78	81	93	110	126	142
Quadrant 3	129	136	143	162	176	185	199
Quadrant 4	148	152	158	170	183	198	224
Total	453 (3%)	466 (3%)	484 (3%)	536 (3%)	600 (4%)	648 (4%)	717 (4%)

X-ray spectroscopic calibration at various temperatures

Calibration data were obtained by shining various radioactive sources (^{241}Am, ^{57}Co and ^{109}Cd) on the quadrants at various temperatures. For automatic analysis, monochromatic lines are modeled as a Gaussian in a region around the peak ($-1\sigma'$ to $+2\sigma'$ of the channel with highest counts, where σ' is the approximate Gaussian σ). The mapping between ADC channels and energy (keV) is given by,

$$\textit{Energy} = \textit{Channels} \times \textit{Gain} + \textit{Offset}$$

Gains and offsets measured for all pixels at different temperatures. A typical energy spectrum is shown in Figure 5.4. In most detector modules, inter-pixel gain variations are small (< 10%). The typical energy resolution is shown in Figure 5.5. The energy resolution at 22 keV and 33 keV are likely to be overestimates because the line blends at these energies are not segregated. There is a marginal change in gain and energy resolution as a function of temperature in 0 – 15 keV region. For onboard response calculation, however, the measured gain and spectral response at each temperature will be used.

Figure 5.4 Spectra for different energies

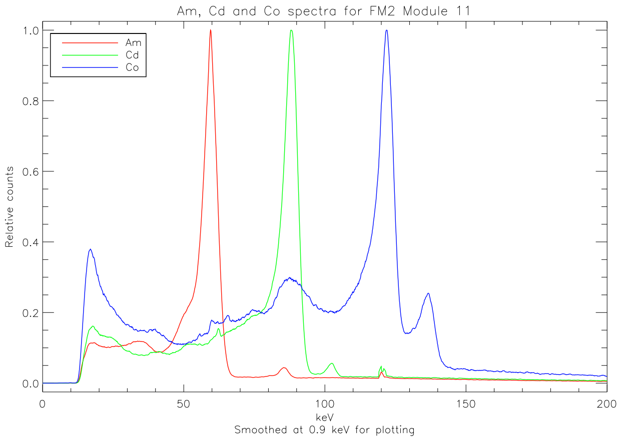

Fig 5.5 Energy resolution as a function of energy

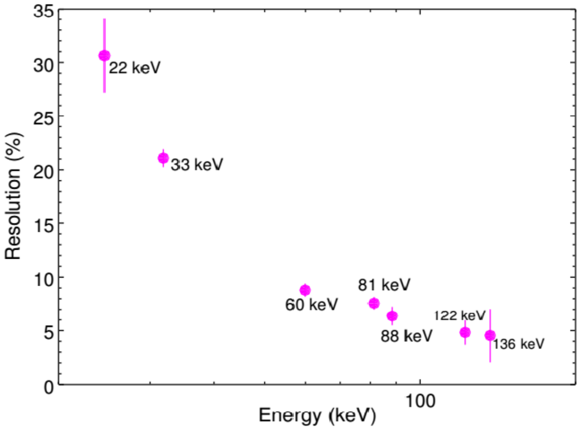

Coded Aperture Mask (CAM) Calibration

The shadow patterns of the CAM and the coding techniques are tested to check the efficiency of the coding device to the given radiation. This is done by shining strong radioactive sources at known fixed positions, typically 100 – 200 cm above the mask. The radiation from the source, on its way to the CZT detector, was intercepted by the coded mask plate situated at a height of 48 cm above the detector. The photons detected by the CZT module were accumulated into an event list, recording the position (pixel number), energy (PHA channel number) and time of each event plane. These data were then analysed using the CZTI imaging algorithm and the location of the source thus reconstructed was compared with the position at which the radioactive source was placed during the acquisition of the data. The reconstruction process began by counting the total number of events recorded in each detector pixel, resulting in a Detector Plane Histogram (DPH). Each count value in the DPH was then divided by the relative quantum efficiency of the corresponding pixel. The array resulting from this is called a Detector Plane Image (DPI). This DPI is a linear combination of shadows of the coded mask cast on the detector plane by sources in the field of view. Alibrary of shadow patterns expected from sources located at different positions on the source plane was created by a ray tracing method. Different methods like Cross correlation, chi-square shadow fitting, and Richardson-Lucy algorithm (based on Bayesian inference), were applied to get the source position. It was found that results from the three different methods agree well, to better than 2 arcmin. The test was repeated at two different energies (60 keV and 122 keV) and it was found that at 122 keV, the PSF is seen to widen slightly, by about 10%. Above 100 keV the mask plate begins to become transparent, reducing shadow contrast and worsening the imaging capability. The results, however, show that decent imaging would still be possible at energies as high as 120 keV, with a PSF of less than ~4 arcmin FWHM.

Field of View of the CZT imager

The Field of View (FoV) of the CZT imager is energy dependent due to greater transparency of the collimator material at higher photon energies. The angular response pattern contains a central core of ~6 deg radius which is common to all energies, and represents the view through the top coded mask surface. Transmission through the collimator slats and side walls contribute wings to the response pattern, the relative strength of which rises with increasing energy. The FoV may therefore be quantified as the amount of solid angle the response pattern covers at a given fraction of the peak on-axis response. It is to be noted that not all of this coverage may be contiguous. We compute the FoV by summing the solid angle of all parts of the effective area distribution that rise above a specified fraction of the on-axis value. The resulting estimates, for different photon energies, are presented in the Fig. 5.6. The FoV evaluated at 50%, 20% and 10% of the peak response at each energy is shown. The FoV increases monotonically with photon energy, apart from a bump near 67 keV due to Tantalum K escape.

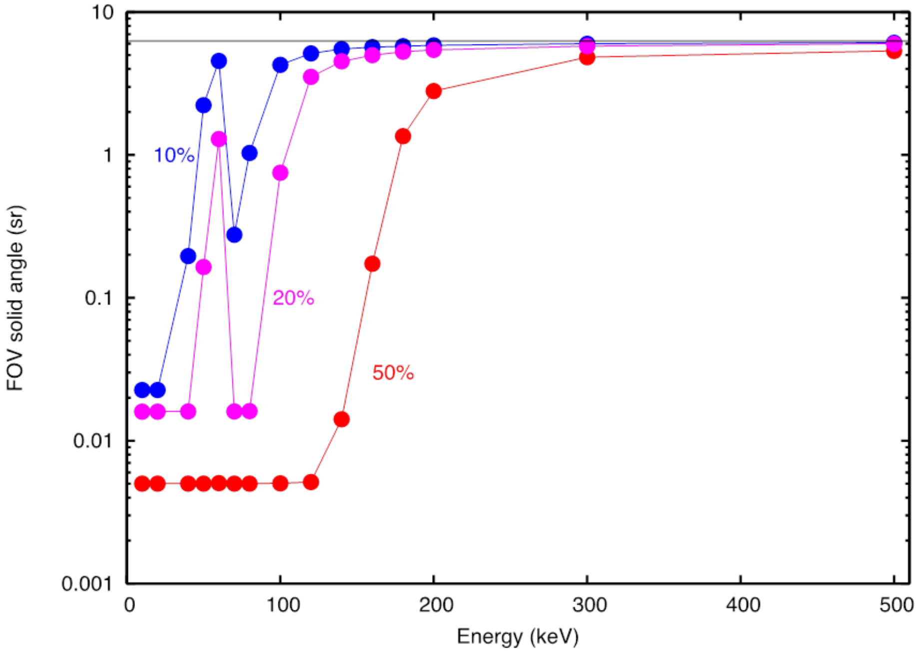

Fig. 5.6 Field of View of the CZT Imager as a function of energy

Effective Area of the CZT Imager

The effective area of the CZT Imager as a function of photon energy and illumination angle has been estimated by accounting for the energy-dependent transmission through the various surfaces making up the CZTI structure, and the energy-dependent absorption by the CZT detector, at different angles of incidence. The result is shown in Fig. 5.7 below. The local peak in effective area near 67 keV occurs due to Tantalum K escape.

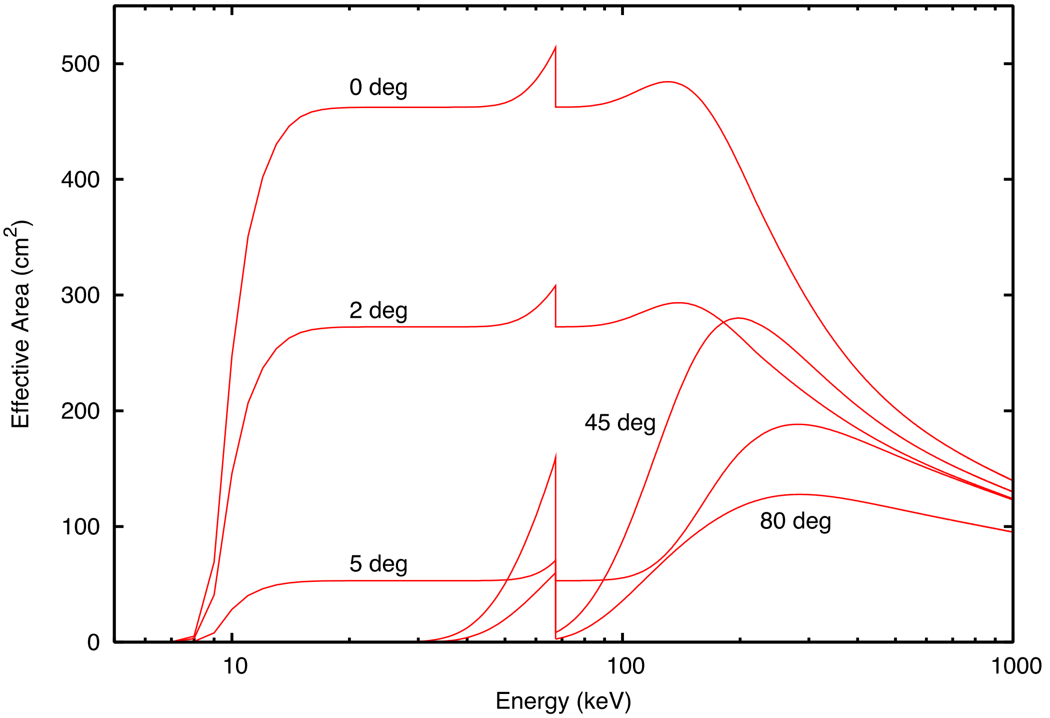

Fig. 5.7: Effective area as a function of energy of the Astrosat CZT Imager at normal incidence (0 deg) and several other off-axis angles.

Alpha-tagging in CZTI

A 10 mm^{3}CsI(Tl) crystal, embedded with a radioactive source ^{241}Am and viewed by a photodiode of 10 mm^2 area, is placed beside the CZT detector. With each disintegration of the 60 keV photon from this source, an Alpha particle (energy about 5 MeV) is also emitted. The alpha particle is absorbed in the small CsI(Tl) detector, whereas the 60 keV X-rays will escape from this detector and, in most cases, will interact with the CZT detector. The alpha particle produces a light pulse in the CsI(Tl) crystal, which in turn is converted into an electrical pulse at the output of the photo-diode. Any output in the CZT detector coincident with the pulse output from the CsI(Tl) detector is deemed to be originating from a 60 keV photon. This method is used to calibrate the energy response of the CZT detector for its energy response.The basic design principles are discussed in Rao et al. (2010, NIMPA. 616, 55) and it was estimated that, for an alpha source strength of 1000/s, about 20 – 30 60 keV X-rays should be emerging from the alpha module. The time co-incidence was done digitally and this aspect is rigorously tested in the QM and one FM detector. The tunable parameters were examined carefully, and it was found that the alpha-tagged information can indeed be extracted from the data. However, the flight configuration is such that the final alpha count rate is as low as ~1 count/s, necessitating a large integration time, grouping of pixels, and use of background lines for the onboard calibration.

Veto calibration

The veto detector is a 20 mm thick CsI(Tl) scintillation, of size 167 mm X 167 mm, viewed by two one inch Photo-multiplier tubes (PMT) positioned at two sides of the crystal. Minimum detection sensitivity is 50 keV for incident photons. The main purpose of this detector is to recognize background X-ray/ gamma-ray radiation (above 100 keV) and tag the main X-ray events (in the CZT detector) with the information that the X-rays are accompanied by a background X-ray/ gamma-ray. The energy resolution of this detector is not significant. These detectors are procured from Scionix Holland, the same suppliers who have provided the RT-2 phoswich detectors and the ACS system for Chandrayaan-I. For the CZT-Imager, it was decided to carry out a minimum screening of 10 cycles of thermo-vac cycling (passive). The temperature range was -20 to +50° C. The HV parts were potted with HV 93-500 and the screening and thermo-vac tests were done after the potting. It was found that the gain uniformity over the area is correct to 10%.After the FM assemblies, the amplifier gain was adjusted so that the upper level corresponds to about 500 – 600 keV. The LLD, however, can be changed by command. The test resultsshow that the peak position is linear with energy.

The Veto detector is designed to capture the forward scattered gamma-rays. In the laboratory, it is quite difficult to reproduce this result because any gamma-ray source, like ^{133}Ba, has a low energy line with much higher probability of interaction. It was, however, possible to capture the Compton scattered events by restricting the energy range of CZT detectors to a narrow window of 40 – 70 keV (to detect only the Compton scattered events). When plotted against the coincidence window time, at > 12 micro-seconds, the data shows the expected coincidence events (about 10% of the total events).

Time tagging and polarization

In CZT-Imager, individual photons are tagged to an accuracy of 20 micro-seconds. The onboard clock is logged every 16 seconds based on a pulse coming from the Satellite Positioning System (SPS) and ground calibrations show that the PE time can be correlated to SPS time correct to about 2 microsec. The pixilated nature of the detector can be used for measuring the polarization of the incident X-ray photons based on the principle of Compton scattering by detecting the Compton scattering event in one pixel and the scattered photon in another pixel. However this requires the capability of recording two simultaneous events in different pixels. The ability of CZT modules to detect polarization has been verified in the laboratory. Details of this experiment is given in Vadawale et al. (2015; A&A submitted) and in Fig 5.8 we show the fitted and the experimentally observed modulation patterns demonstrating that CZT-Imager is capable of measuring polarization of bright onboard sources (> 500 mCrab) in the 100 – 300 keV region.

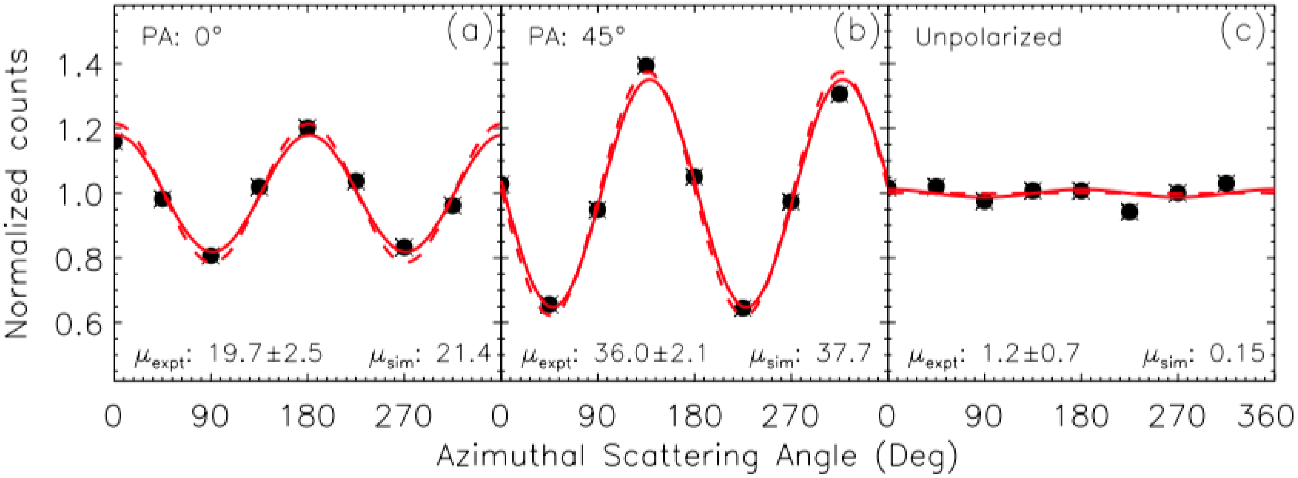

Fig 5.8: Experimentally measured modulation curves for partially polarized X-rays at two polarization angles.

Response matrix generation

Mono-energetic lines detected by CZT detectors have a long tail toward low-energiesoriginating from the partial charge collection due to 'hole-trapping'. This is modeled in terms of crystal charge transport properties. CZT detector line profile and its dependence on the basic parameter is well understood and the model is implemented in IDL, S-Lang (available in ISIS as a local model) and the 'mobility lifetime' products for charge carriers are obtained by simultaneous fit to individual pixel spectra at multiple energies. Sufficient calibration data are available to generate pixel wise parameters at multiple temperatures (gain, offset, resolution, and otherline parameters) and a flow chart is given below (fig.5.9).

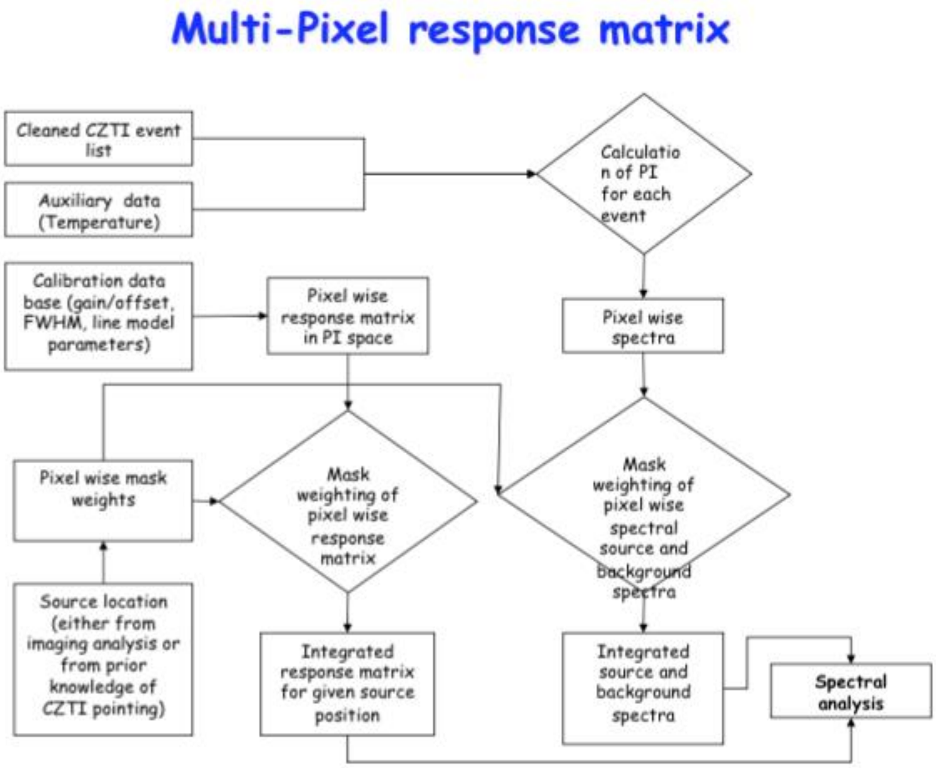

Figure 5.9: Flow-chart for multi-pixel response matrix generation

Onboard Performance of CZT Imager

Cadmium Zinc Telluride Imager was made fully operational on October 5, 2015, Day 8 of Astrosat. The structured onboard software worked in an autonomous fashion, and the general health of the instrument was found to be normal. The genaral behaviour of the alpha and Veto counts are found to be steady.

Pixels disabled:

Whenever a pixel becomes noisy and floods the data for a long duration, it is being disabled. There is a provision to enable the pixels which have been disabled. The total number of pixels disabled during ground calibration as well as onboard operation till 30-11-2017 are as shown in the following table.

	Quadrant 1	**Quadrant 2**	**Quadrant 3**	**Quadrant 4**
Ground	204	216	127	209
On-orbit	85	117	74	160
Total	289	333	201	369

The total pixels disabled are 1192 (7.27%). It is found that roughly about once in a fortnight a few pixels (less than 5) need to be disabled further. Hence it is estimated that the total number of disabled pixels during the five year life of the instrument would be within the design goal of 10%.

CZT module thresholds:

Before launch most of the CZT modules were set at 40keV for room temperature operation. The thresholds were reduced on-board when the detector temperatures got stabilized. The following are the thresholds values as on 30-03-2016. A majority of modules (49, i.e. 76.6%) are set at 15 keV threshold and 9 modules (14%) are at 20 or 25 keV threshold and a small number (6 modules) are at 40 or 50 keV threshold.

Module	Quadrant1 Thresholds (keV)	Quadrant2 Thresholds (keV)	Quadrant3 Thresholds (keV)	Quadrant4 Thresholds (keV)
0	15	50	15	15
1	15	15	15	15
2	15	15	15	40
3	15	15	20	15
4	15	25	15	15
5	15	15	15	50
6	25	15	15	15
7	15	20	15	15
8	15	15	15	15
9	15	15	20	25
10	15	15	40	25
11	15	15	50	15
12	15	15	15	15
13	40	15	15	25
14	15	15	15	15
15	20	15	15	15

SAA region:

CZTI payload enters the SAA mode based on the warning signal from CPM or through telecommand from ground. After evaluating the CPM performance on board, the CZTI SAA Entry and Exit logic has been enabled through CPM. If the number of counts detected by CPM exceeds 14 in 5 seconds, it sends a warning signal to CZTI and the high voltages are switched off, causing the payload to enter mode 9. On exiting from SAA region, the high voltages are switched ON and the payload come backs to the normal mode (mode 0).

Operational modes:

The CZTI payload is always being operated in normal mode (mode 0) post launch. During SAA passage, if the charged particle counts are greater than the set threshold, it goes to mode 9 and returns to mode 0 when the charged particle counts drop below threshold. If the on-board satellite memory is full, the satellite BDH would send a memory full signal to CZTI. However such a situation has not so far been encountered in orbit. In future if the CZTI payload receives a memory full signal from satellite BDH, it will go to mode 4(memory level =1) or mode 12(memory level > 1) or mode 13(memory level > 1 + SAA warning). In these modes the data are acquired at a reduced rate and are stored in CZTI internal RAM. After memory full is released, the data stored internally are sent to the on-board satellite memory.

Onboard software:

CZTI processing electronics can hold four versions of onboard software in its EEPROM. Before launch, all the four versions held the same software. Post launch, it has been noticed that the cosmic ray interactions with the CZT detectors is very prominent, thus creating many false events in the detectors. To reduce these events, a new software has been uploaded to page 2 of EEPROM. The number of CZT events per Quadrant per second has been reduced from a value of 1200 before the software update to a value of 400 after the software update.

Timing parameters:

The timing parameters T1 to T7 for alpha and veto event association have been calibrated on board and the following optimized values are obtained.

Parameter	**T1**	**T2**	**T3**	**T4**	**T5**	**T6**	**T7**
Time(us)	1	8	20	15	40	10	62

CZT module temperatures:

The average module temperature is being maintained at 12°C with a 3°C variation.

Background counts:

The CZT and veto detector background is varying uniformly with time with the CZT background count rate range of 80 to 120 counts/second/Quadrant and veto background count range of 300 to 450 counts/ second/ Quadrant.

Timing accuracy:

In 16 seconds, the time difference between CZTI clock and STBG clock is around 30 micro seconds and it is constant through out the operation period indicating the stable behavior of CZTI clock.

Scanning Sky Monitor

Chapter 6

The science objective of SSM is to scan a large portion of the sky every few hours to detect and locate transient X-ray sources in the outburst phase, in the energy band of 2.5 to 10 keV. Therefore, it is required that SSM has a large field of view (FOV) with a good angular resolution so that once detected the position of the sources is known to a few arcmin resolution in sky co-ordinates. This is to enable other instruments on ASTROSAT and ground based observatories to conduct detailed observations of the source. In addition to this, SSM will observe known transient X-ray sources in its subsequent scans which will be used to generate long term light curves of these binary systems. This will help study of long term behavior of the observed transient systems.

Instrument Description

SSM consists of three nearly identical one dimensional position sensitive gas-filled proportional counters with a coded-mask and associated electronics, each having a FOV of the order of ~$22^o \times 100^o$ (for edge SSMs) and ~$26.8^o \times 100^o$ (for centre SSM). The assembly is mounted on a platform which can be rotated to scan the sky. Figure below (Fig. 6.1) shows the picture of the three units of SSM mounted on a single platform. SSM is composed of the following elements: detectors, the associated electronics, imaging element (coded-mask), platform, motor and its electronics.

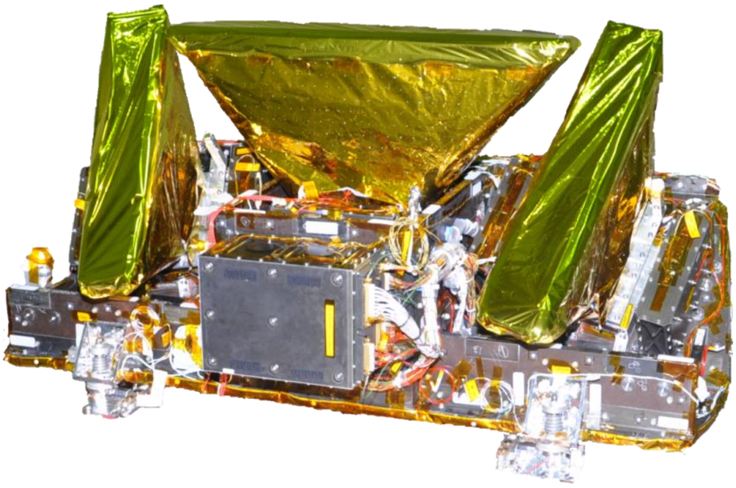

***Figure** 6.1 : Scanning Sky Monitor: Each of the three SSM cameras have their own electronics system. The Central SSM will point towards the +Yaw axis, while the two Edge SSMs will be canted away by 45^o from that axis. The entire assembly will rotate about the +Yaw axis.*

The instrumentation for SSM including the detectors and electronics is developed at Space Astronomy Group at ISRO Satellite Centre (ISAC), Bangalore. The design and fabrication of the platform is by CMSE, VSSC, the mechanism and motor is by SMG, ISAC, and the drive electronics and commanding is provided by CSG, ISAC. The assembly and integration of the complete payload was carried out at ISAC, Bangalore.

SSM instrument is sensitive in the energy range 2.5 to 10 keV. The window of SSM is aluminized Mylar of thickness 50 microns and this limits the detection efficiency at 2.5 keV. Effective area of SSM at 5 keV is 51 cm^2 and that at 2.5 keV is 11 cm^2. SSM detectors are position sensitive detectors, position resolution of SSM at 6 keV is ~1 mm. Angular resolution of SSM is ~12 arcmin in the coding direction and that across is 2.5^0. Energy resolution of SSM is ~25% at 6 keV. Sensitivity of SSM is ~28 milliCrab for 10 minutes integration at 3sigma. Figure 6.2 shows the sensitivity curve for SSM.

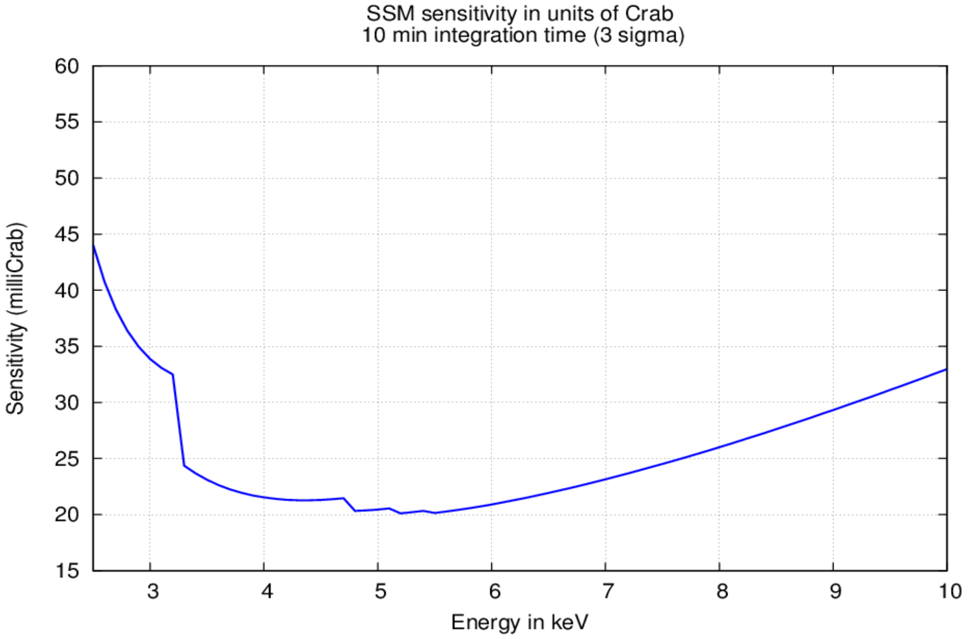

Figure 6.2: Sensitivity of SSM

Detectors for SSM:

All three units for SSM have a position-sensitive proportional counter as the detector element. The detectors are multi-wire position sensitive proportional counters. There are eight anodes in each detector and the anodes are powered with a high voltage (HV) of the order of 1500 volts as compared to that of cathodes which are at zero potential. Many such cells (as shown in figure below) constitute the geometric area of a detector. These cells are enclosed in a gas-filled chamber having an entrance window thin enough to allow the incident X-ray photons into the counter. Figure 6.3 shows the schematic view of the cells . inside an SSM detector. The top layer consists of position-sensitive anode wires surrounded by wire-walled cathode forming individual cells. Figure 6.4 shows the photo of the wire module inside the detector.

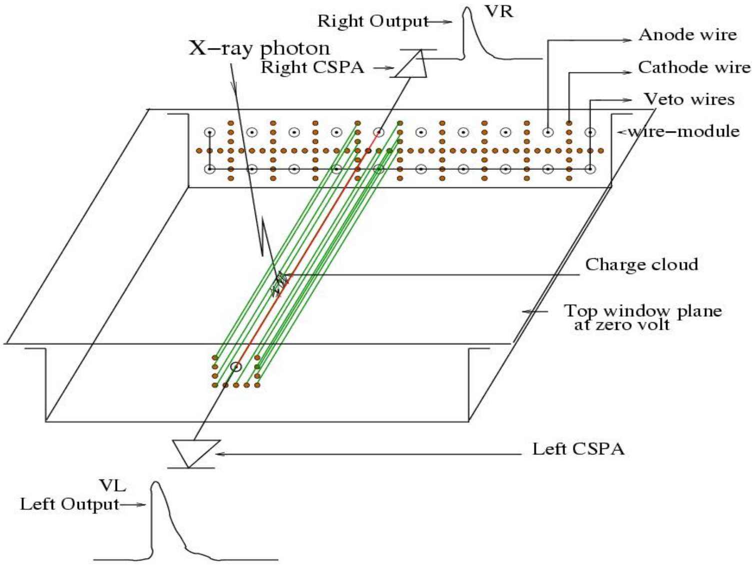

Figure 6.3 : Schematic view of SSM cells. Only one of the cells is shown lengthwise, with a photon incident on the cell producing charge cloud at the anode.

Principle of Operation

When an X-ray photon enters the gas chamber it ionizes the gas by photo-electric effect which leads to formation of several electron-ion pairs. The electrons are accelerated towards the anode resulting in further multiplication of the charge which is collected at the anode. In a position-sensitive detector the anode being resistive, the charge is proportionately divided to the two ends depending on the position where the charge cloud is collected along the anode wire. This charge is converted into voltage using a charge sensitive preamplifier (CSPA) at both the ends.

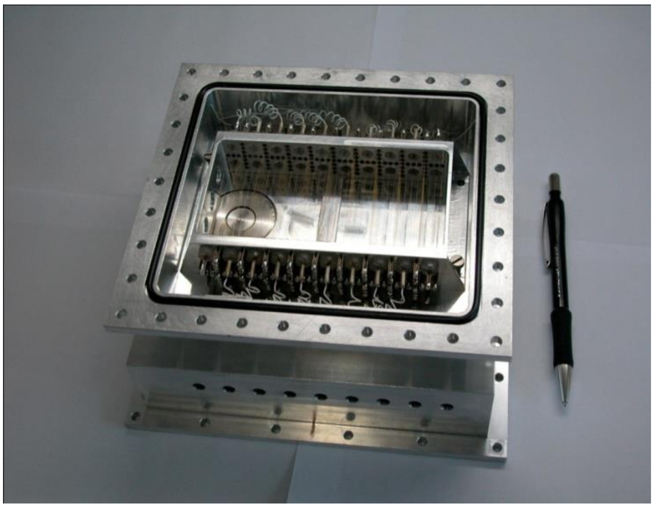

Figure 6.4 : Wire module kept inside the detector

The corresponding voltage pulses at either ends of the anode are referred to as left (V_L) and right (V_R) outputs of the anode. The total amplitude of both the outputs is proportional to the energy of the incident photon. The position (P) of the incident photon on the detector plane is given by $P=((A*R)+B)/(R+C)$, where ratio, $R = (V_L-V_R)/(V_L+V_R)$, V_L and V_R are the amplitudes of the left and right output pulses and A, B and C are the calibration constants of that particular anode on which the photon is incident.

The SSM detector plane consists of two layers of wire-cells, central eight of the top layer being active anode cells. The two edge cells of the top layer and the ten cells in the bottom layer are all connected together to form the background or veto layer. The information that we get about every photon that is incident on the detector are 1. Time of arrival, 2. Energy and 3. Position of incidence.

Design of Mask

Six different coded mask patterns with 50% transparency are joined to make the complete mask plate as shown in figure 6.5. The design of the coded mask and the deconvolution software is developed in collaboration with Prof. Dipankar Bhattacharya of IUCAA.

Figure 6.5 : The coded mask plate with six different mask pattern used in each of the three SSM cameras.

Electronics for SSM

The Electronics system for SSM is composed of three units: (a) Charge Sensitive Pre-Amplifiers (CSPA) and post amplifiers (PA), (b) Front end electronics consisting of low voltage DC-DCs, HV programmer, logic unit for LLD/ULD/event-analysis, peak detectors, ADC, etc and (c) the Processing Electronics (PE) consisting of FPGA based system for event processing, buffer memory, telecommand and telemetry interfaces and the interface circuits for data transfer to Data Handling package. The detector is powered using High Voltage distribution unit mounted behind the detector. Figure 6.6 shows the block diagram of the detector with the electronics.

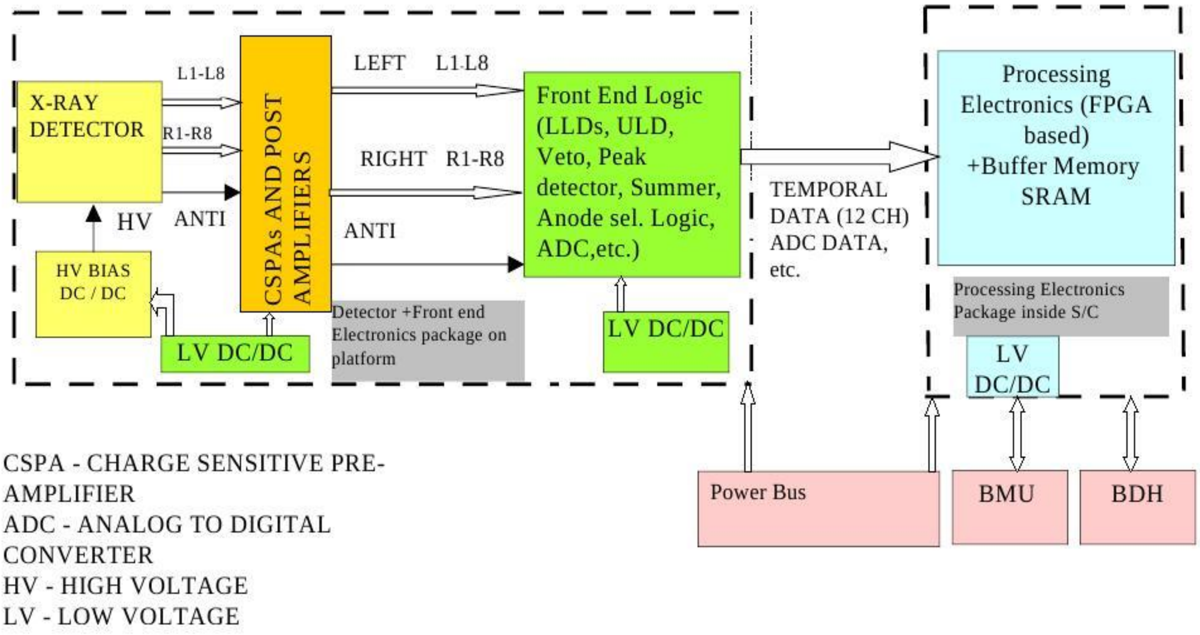

Figure 6.6 : Block diagram of the Electronics System of SSM

Processing of an event:

The charge collected at the anode for every photon incident is converted to a voltage pulse using a CSPA on either sides of the anode. The CSPA output is further shaped and amplified. There are seventeen such chains for each SSM detector unit, sixteen of them are connected to both ends of eight anodes and one of them is connected to the veto layer. The front end logic unit processes signals from each of these chains. Event outputs between Lower Level Discriminator (LLD) and Upper Level Discriminator (ULD) are accepted for processing. Charge particle rejection is done by the technique called anti-coincidence, where the event is rejected when (a) signals are present in both the top anode layer as well as the bottom veto layer simultaneously, or (b) more than one anode has an event simultaneously. The amplitude of every accepted event is measured and digitised and then the ADC output of each event, both left and right sides, are sent to the PE unit. In addition several channels regarding count rates of the anodes and veto, etc. are also sent to the PE. The PE which is a FPGA-based unit accepts these events, stores them in buffer memory and interfaces with the Data Handling system of the spacecraft. The PE also acts as both telecommand and telemetry interface for the complete SSM electronics system. The time of incidence of every photon is tagged with the event by the PE using an onboard SSM clock. This clock is periodically synchronised with the spacecraft BMU clock. In addition, the electronics system also has circuitry for sensing and reducing High Voltage during high charge particle regions based on command-set thresholds and also corona sensing with auto-shutoff. Data from the PE is sent from the buffer memory through Data Handling and stored in the main spacecraft Solid State Recorder package for readout during visibilities. The detector and front end electronics packages are mounted on a rotating platform on the anti sun side of the spacecraft whereas the processing electronics is mounted inside the S/C. A flexible cable bunch is used between the packages.

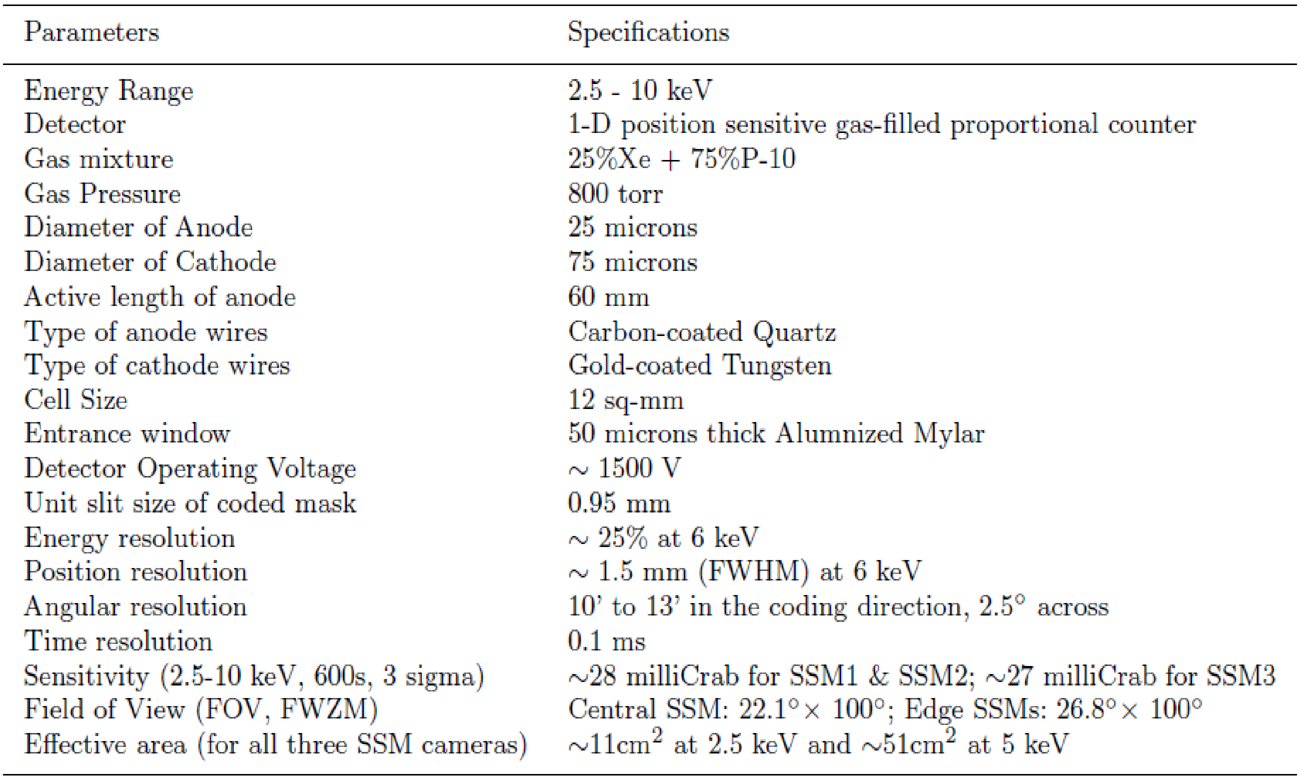

Parameters	Specifications
Energy Range	2.5 - 10 keV
Detector	1-D position sensitive gas-filled proportional counter
Gas mixture	25%Xe + 75%P-10
Gas Pressure	800 torr
Diameter of Anode	25 microns
Diameter of Cathode	75 microns
Active length of anode	60 mm
Type of anode wires	Carbon-coated Quartz
Type of cathode wires	Gold-coated Tungsten
Cell Size	12 sq-mm
Entrance window	50 microns thick Alumnized Mylar
Detector Operating Voltage	∼ 1500 V
Unit slit size of coded mask	0.95 mm
Energy resolution	∼ 25% at 6 keV
Position resolution	∼ 1.5 mm (FWHM) at 6 keV
Angular resolution	10’ to 13’ in the coding direction, 2.5° across
Time resolution	0.1 ms
Sensitivity (2.5-10 keV, 600s, 3 sigma)	∼28 milliCrab for SSM1 & SSM2; ∼27 milliCrab for SSM3
Field of View (FOV, FWZM)	Central SSM: 22.1° × 100°; Edge SSMs: 26.8° × 100°
Effective area (for all three SSM cameras)	∼11cm^2 at 2.5 keV and ∼51cm^2 at 5 keV

Table 6.1 : Technical details of SSM

Ground calibration

SSM ground calibration includes spectral and positional calibration. Spectral calibration has been done to study and keep track of the gain of the detectors for SSM. Positional calibration of SSM gives the calibration constants to derive the position of every photon incident on the detector.

Spectral calibration

SSM detector is calibrated for spectral response at different energies in the range of interest. The energy range of interest for SSM is 2.5 keV to 10 keV. The detector is calibrated at different energies to derive the Energy-vs-Channel relation and the Energy-vs-FWHM relation at different energies. These relations are required to generate the response matrix of the detector. The position resolution at different energies is also estimated for SSM.

Characteristic X-rays are used to calibrate the detector at different energies. The photon energies used to calibrate the detector are Ca K_α (3.69 keV), Ti K_α (4.51 keV), Mn K_α (5.89 keV, Fe-55 radioactive source) and Cu K_α (8.04 keV). Ca K_α , Ti Kα and Cu K_α are produced by shining the continuum spectrum of an X-ray gun onto foils of respective materials to produce the characteristic X-rays. Thus, the detector is calibrated with four different X-ray sources within the energy range of interest.

Positional calibration

The position of a photon incident on the detector is determined from the ratio of the charge collected on either sides of the anode. It has been observed that for photons incident at the geometric centre of the anode, the left and the right output amplitudes are not the same and hence the calculated position using the charge ratio from the output pulses does not match with the geometric position. Therefore, it is required to calibrate the detector for its positional response and to get the correction factor, which are called the anode calibration constants, with respect to every anode in the detector.

On-board Calibration

Calibration with Crab nebula

Calibration of SSM includes imaging aspects, sensitivity and gain of the detectors on SSM. Crab nebula has been observed for detailed calibration of SSM for all different aspects of the payload. During the PV phase, all three units of SSM have been pointed to Crab and observations were done with Crab at different locations in the FOV of each of the three cameras of SSM. Data from observations of Crab have been processed to refine the calibration database for imaging from that obtained on-ground. Any change in sensitivity of the instrument is calibrated with Crab observations.

Also any gain change in the cameras can be identified with the change in hardness ratio obtained from x-ray sky observations.

The hardness ratio (HR2) is the ratio of the flux in the energy bands 6 to 10 keV and 4 to 6 keV. Any 10% variation in the gas gain can be detected from the variations in the hardness ratio calculated from observations of Crab nebula as well as sky observations. For any variation in the gain of the detector, the operating voltage of SSM can be tuned to bring it back to the nominally operating gain value.

Crab has been observed with SSM at various stages during the PV phase for all the above calibration aspects.

SSM Data

Data from SSM detectors are of two types, temporal and time-tagged. The temporal data gives the counts detected by the detector every 100 ms and the time-tagged data gives the information of every event detected in the detector. From the time-tagged data information like energy of the incident photon, position of incidence can be calculated. Using this data the shadow pattern cast by different sources in the FOV of SSM is derived, which is later used to derive the position and flux of the sources in the FOV.

SSM2 unit, one of the edge cameras has been switched OFF since August 2016, as it developed gas leak by mid of February 2016. SSM with its two units, SSM1 (one of the edge cameras) and SSM3 (the central camera) is continuing to observe the X-ray sky with it step and stare mode of operation. However, SSM2 unit has shown a reduced efficiency and the correction factor for the flux reported for sources observed by this unit is taken care. The light curves are generated and made available at the SSM website.

SSM Deliverables

The Light curves of different sources in the FOV are made available to the public in the SSM website. SSM data has been released on ISSDC web site for public access. The URL for accessing SSM Web is

https://webapps.issdc.gov.in/SSM_Web/index.jsp

and it can also be accessed through ISSDC website

https://issdc.gov.in --> Astrosat --> SSM Web

Chapter 7

Charged Particle Monitor

Satellites in the Low Earth Orbit (LEO) pass through the trapped radiation belts of the South Atlantic Anomaly (SAA), where the particle environment can change very drastically within a few tens of seconds. Due to the high density of energetic particles (mostly protons), there could be adverse scientific and technological effects on the instruments in the satellites like, glitches in the data, aging of the scientific instruments and even permanent damage to the detectors. Hence, this region should be monitored properly and precautions should be taken to protect the scientific instruments during the satellite's passage through the SAA region. The Charge Particle Monitor (CPM) for AstroSat warns the satellite instruments about the entry and exit points of the SAA region and thus serves the purpose of a monitor. A picture of the Flight Model of CPM is given in Fig 7.1.

Figure 7.1: The Flight Model of AstroSat CPM

SAA occurs at altitudes above about 500 km spanning -50^0 to 0^0 latitude and -90^0 to +40^0 longitude. This SAA region changes slowly over time, the dominant drift being westward of approximately 0.3 degrees per year. AstroSat is in a 650 km near-equatorial (6^0 latitude) orbit and it encounters SAA in a few of its 14 orbits per day, spending 10 – 20 minutes in the SAA region, each time. CPM senses the SAA by measuring the total number of charged particles, above a certain energy threshold. Typically, the particle rate is < 1 particle per cm^2 and it can shoot upto> 1000 particle per cm^2 in the SAA region, with a rise/fall time of SAA entry/exit of about 40 s. The particle number spectrum as a function of energy is flat upto about 100 MeV and it falls down sharply above this energy. The CPM is designed keeping these factors in mind, viz., a small area particle detector giving the total number of particle counts above about an MeV in an integration time of a few seconds.

The detector used for CPM is a CsI(Tl) scintillation detector of open area 1 cm^2. The total material covering the detector like the 0.12 mm Teflon light reflector, a thin Copper box acting as a radiation shield and 50 micron aluminized Mylar as the entrance window of the CPM box, etc. have a combined equivalent proton range of about 1 MeV and hence the CPM is sensitive to all protons above about 1.5 MeV. CsI(Tl) is preferred over more common NaI(Tl), because the latter is hygroscopic in nature. Ionising radiations create photons in the scintillating crystal and they are captured by a Si-Pin diode placed at the bottom surface of the CsI(Tl) crystal. This crystal and photodiode assembly is very cost effective compared to semiconductor detectors, and lighter than scintillator photomultiplier assembly (as used in RXTE). Moreover, the photomultiplier needs high voltage biasing and the gain may vary with time. The detector and the readout used for AstroSat CPM does not require high voltage for biasing and it is designed to be rugged, compact and reliable.

Instrument details

The CPM is designed as a stand-alone instrument of AstroSat, with its own power module, tele-command and telemetry interfaces. The instrument characteristics are given in Table 1. The basic detector, as explained earlier, is a CsI(Tl) scintillator coupled to a Si-PIN photo-diode. The detector light output peaks at 580 nm and the light intensity is proportional to the energy of the incident radiation. This light is proportionally converted to an electrical signal by the photodiode. A charge sensitive preamplifier (CSPA) is used to amplify the photodiode output to milli-volt range. The detector, photodiode and CSPA are combined in a compact 1 cm^3 box made by SCIONIX, Holland to form the detector module.

The detector module is mounted on an electronics card along with other electronics like amplifiers, discriminators, and an FPGA for handling interfaces and detector logic. A Power Module, mounted below this card generates +5 V,+12 V,-12 V voltages from Satellite Raw Bus of +42 Volts and consumes about 4 W power. The +5 V supply is used to power the CPM logic circuits, +12 V and –12 V supplies are used to power detector and amplifier circuits.

The detector module generates a pulse corresponding to every incident energetic particle and this pulse is passed through a post amplifier, where milli-volt signal is converted to volt level. The total gain of amplifier is kept around 500 with sufficient bandwidth such that it generates 0.5 microsecond rise time pulses. These amplified pulses are passed through a Low Level Discriminator (LLD) circuit to cut-off noise and select the charge particle signals above a defined value of about 0.5 MeV. The LLD reference voltage value is programmable from ground station through telecommand. It is a 12-bit DAC and 4096 discrete values are possible. The pulse signal from LLD circuit output is digitized and fed to a 14-bit counter. The 14-bit counter is a free running counter gated every 5 sec (default). Gate time is also programmable from ground through telecommand. All digital processing electronics is embedded in the FPGA. The telemetry and telecommand interface with the satellite bus is also embedded in the FPGA. The general health of the instrument is monitored through the analog channels of satellite telemetry.

Ground Calibration of CPM

The calibration of CPM involves proton and gamma-ray energy calibration in the Engineering Model (EM) and gamma ray energy calibration for the Qualification Model (QM) and Flight Model (FM). Since the output from CPM contains only counts above a set threshold, successively changing the threshold and getting an integral spectrum can obtain spectrum of the incoming radiation. This integral spectrum can be converted to a conventional energy spectrum by simple differentiation. The underlining assumption is that the spectrum remains unchanged during the course of observation. During all environmental tests and satellite integration tests, the record of background counts for a threshold of 0.5 MeV are kept and the requirement is that this background counts should be stable within 50%.

Table 7.1: CPM Instrument characteristics

Detector	Type	CsI(Tl)+Si-PIN
	Area	1 cm^2
	Window	Teflon+Copper+mylar (proton range ~ 1 MeV)
	Energy Range	> 1.5 MeV (particle counts)
	Field of View	> π steradians
Package	Weight	2 kg
	Power	4 W
	Size	222 mm X 138 mm X 48 mm
Tele-Command	LLD	0.5 MeV to 10 MeV; (default: 0.5 MeV)
	Integration time	1 s to 32 s (default: 5 s)
	Count threshold for sensing SAA	0 to 16384; step 1 (default: 1000)
	Scan counts at successively increasing threshold	Variable LLD step size and number of samples at each step
Data	Particle counts	Available to other instruments and satellite telemetry
	SAA level	A signal available to other instruments indicating SAA
	Voltage and temperature monitoring.	Every few seconds in satellite telemetry

The proton sensitivity test and linearity checking was done with proton beams of energies 15 MeV, 17 MeV and 18 MeV from the 14 MV BARC-TIFR Pelletron accelerator. The response was found to be linear and it is found to be 0.47 mV/keV, which is slightly greater than the photon response (0.40 mV/keV). This is due to the fact that the light output of CsI(Tl), and hence the relative pulse height is lower for γ ray photon than protons. Also we find that the proton sensitivity of the detector is linear locally, but has some non-linearity in the lower part of the spectrum.

The gamma-ray response was found using Ba^{133}, Cs^{137} and Eu^{152} radioactive sources, with energies: 356 keV (Ba), 662 keV (Cs), 1112 keV (Eu) and 1408 keV (Eu). The spectra are obtained by differentiating the integral spectrum. A comparison of the peaks obtained form 662 keV (Cs) source by this method and the direct MCA method (during card level testing) is shown below. Since CPM generates only counts above a LLD channel, all spectral information are given in the units of LLD channel numbers.

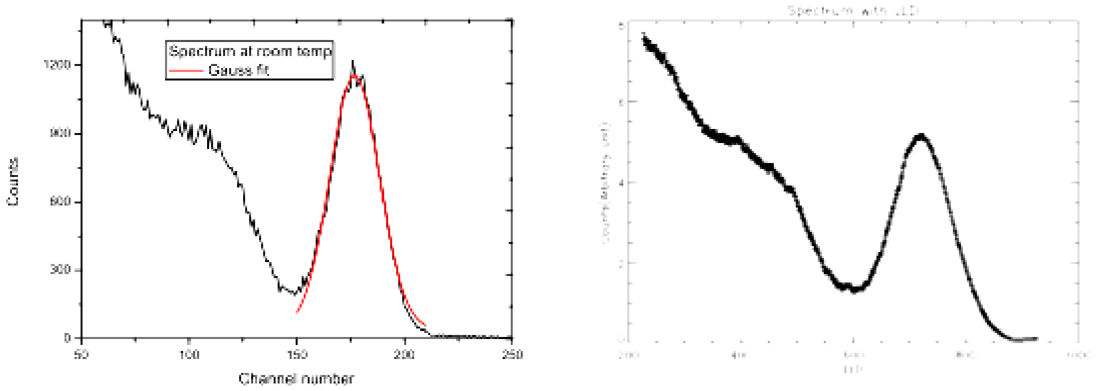

(a) Using MCA (b) Differential spectrum

Figure 7.2: A comparison of spectrum obtained directly and by differentiating the integral spectrum

The observed peak position (LLD channel numbers) for the Flight Model are given in Table 2. The response is linear with a slope of 0.45±0.05 LLD channel/keV and an intercept of -58±33 LLD channels. The peak position was found to be stable correct to 5% in the temperature range 0 – 40 °C and decreased by 10% at 50 °C. The operating temperature of CPM is 0 – 50 °C.

It is estimated that gamma-ray bursts and solar gamma-ray flares which give a measurable count (> 10 counts/s) above 0.5 MeV occur very rarely (a rate of less than once per year). The time-scale for detecting the entry and exit of SAA would be kept large enough to ignore even such rare events. During calibration, the system was also found to be stable when a large number of low energy (6 keV) photons are bombarded on the detector, demonstrating that a stable particle rate measurement is possible even in the presence of intense solar flares.

Table 7.2: Energy calibration of CPM Flight Model

Source	**Energy (keV)**	**Peak Position (LLD channels)**	**Standard error in peak position**
Ba^{133}	356	128	15
Cs^{137}	662	214	15
Eu^{152}	1112	409	27
Eu^{152}	1408	603	25

CPM data availability

The CPM count rate is transmitted through telemetry to ground station. It is also available for onboard users (or payloads) in serial format as Data, Clock and a Latch. A maximum of three users can be supported.

This count rate is compared with a preset value set from ground station through telecommand. Whenever count rate is greater than a preset value the output is activated. The output is de-activated whenever the count rate is less than the preset value. To avoid false triggering, output is activated/de-activated only after 3 successive confirmation of count rate. This SAA warning outputs are available for users. Maximum eight such users can be supported.

The energy threshold of CPM is nominally set at 0.5 MeV and this can be changed unto 10 MeV with a few keV steps. The count threshold for the automatic onboard sensing of SAA can be set from 1 to 16384 counts with a step of 1 count and the integration time can be set from 1 s to 32 s with a step of 1 s. Additionally, there is a command facility to automatically step up the energy threshold so that, at stable non-SAA regions, integral energy spectrum can be obtained.

As a back up to CPM, AstroSat uses time tagged commands to alert the entry/exit of SAA, based on a SAA model. The measured intensity of energetic charge particle rates from CPM will be used to refine this model periodically.

Onboard testing

The operation of CPM started from 2015 September 29, a day after the launch of AstroSat. The threshold for registering protons is kept at 1 MeV. The integration time for the device is kept at 5 s and the count threshold for SAA trigger is kept at 14 counts (corresponding to a rate of 2.8 counts/s). The duration of the time spent in SAA region varies with orbit which causes the variation in observed the peak count rate. The maximum observed peak rate is around 400 counts/s. It is also observed for some orbits the satellite does not pass through SAA. Currently only CZTI is using the SAA trigger signal. The rest of the payloads are using the backup model.

Stability issues in the detector can occur due to continuous bombardment with high energy particles. To evaluate the stability, flight range was divided into bins of 1° by 1°. Mean and standard deviation of count rate was evaluated for each bin. For non-SAA region the mean count rates is found to be less than 1. For SAA region, higher counts and thus higher mean is expected. This was also observed in the data from CPM. Monthly contour maps of the SAA region were also generated which show similar shape, indicating the stability of the detector.

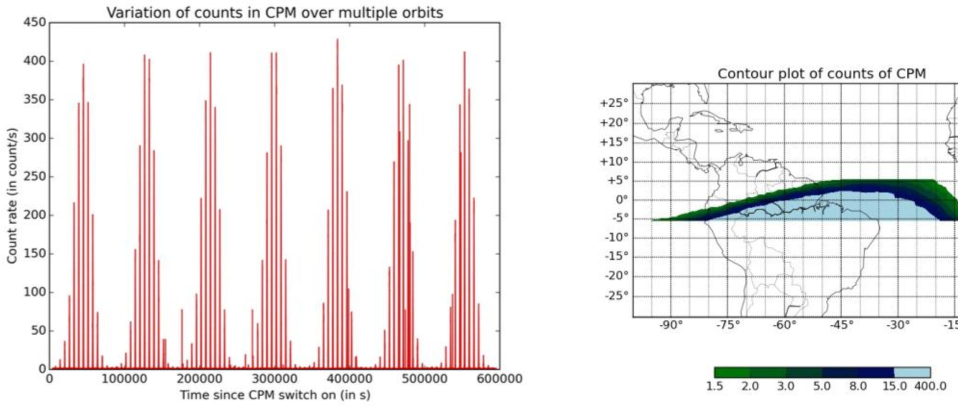

Figure 7.3 Left*:** A Light curve of particle rates as observed by CPM. The recurring peaks denote the section of SAA region traversed in an orbit. The highest peak denotes when the satellite ventured deepest into the SAA region. ***Right: Contour maps of SAA region. Count rate data for a month was spatially binned and contour maps were generated. The sharp transition to SAA can be seen and accordingly the threshold was kept at 2.8 counts/s. Counts greater than 15 counts/s are shown in light blue for a better depiction of the transition region.

Chapter 8

Observing with AstroSat

AstroSat orbit

Based on the requirements of the useful lifetime, low background of charged particles and considering the PSLV capability, a 650-Km, 6-deg inclined orbit is selected for the AstroSat. No orbit maintenance is envisaged for the AstroSat. The altitude of the spacecraft is not important for the scientific payloads, and the only criterion is that the orbit should be sustainable for more than 5 years without re-entry due to aerodynamic drag. The osculating nominal elements of the AstroSat Spacecraft are provided in Table given below:

Osculating nominal elements of AstroSat

Epoch(U.T)	2013 328 4 9 5 4400
Semi-major axis (km)	7028.29697 km
Eccentricity	0.00184
Inclination (deg)	6.002890 deg
Argument of Perigee (deg)	176.99319 deg
Longitude of Ascending node (deg)	218.32340 deg
Mean Anomaly (deg)	31.33291 deg

Observing Constraints

- **South Atlantic Anomaly (SAA)**

  The extent of SAA spread for 650 km orbit has been provided in Fig.8.1 as given below :

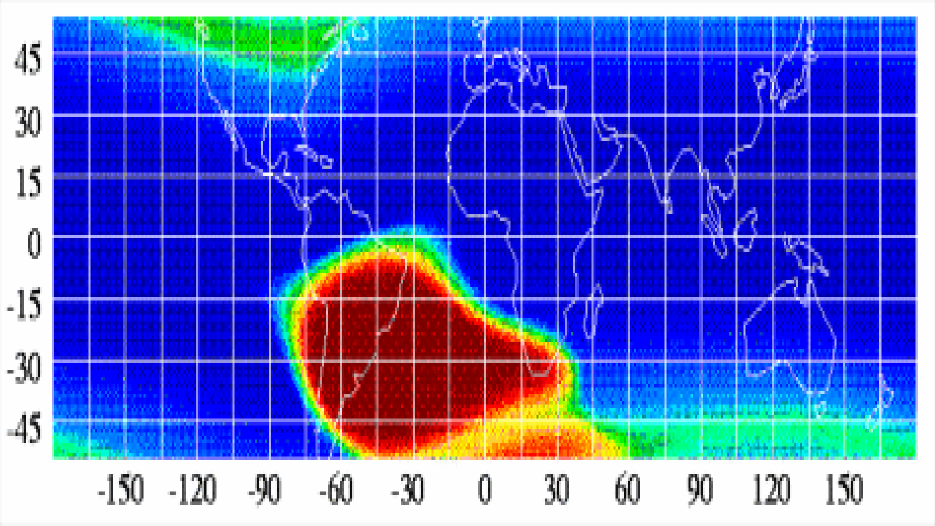

Fig.8.1: Extent of SAA region

It can be seen that the SAA covers -5° S to -50° S in latitude. In order to reduce the effect of SAA, the satellite is to be placed in low inclination orbit. SAA cannot be completely avoided. Keeping some safety margins, it is decided to keep an inclination of 6° with an orbital height of 650 km for ASTROSAT satellite. But from the comfortable elevation for the primary station Bangalore for ASTROSAT, 8 degree inclination orbit would have been preferred. Further, the SAA region depends on the sensitivity of the instruments onboard and the size of the covered region of SAA varies depending upon the required intensity of the particles. Therefore, 6 degree inclination orbit has been retained.

- **Celestial constraints**

  All the payloads are sensitive to Sun & Moon
    - Included angle between camera Axis to Sun greater than 45 degrees.
    - Included Angle between bright Earth limb to the payload axis greater than 12 degrees
    - Included angle between camera Axis to Moon greater than 20 degrees.
    - Included angle between camera Axis to Velocity vector (ram angle) greater than 12 degrees.
    - Star sensor bore axes meeting 50 degrees wrt Sun

- **Sky Visibility and Bright Source Avoidance**

  Attitude definition and constraints to meet the payload visibility and bright source avoidance is planned with the following definitions of the spacecraft axes:

Attitude Definition

Roll = S, Unit position vector of source
Pitch = Roll X Sun (YAW.SUN>90deg)
Pitch = -Roll X Sun (YAW.SUN<90deg)
Yaw = Roll X Pitch

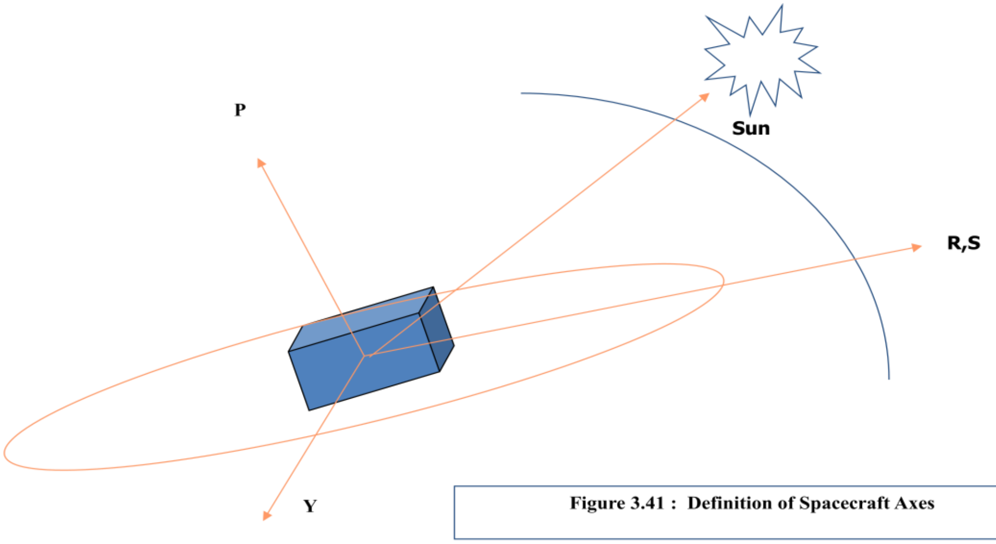

Figure 3.41 : Definition of Spacecraft Axes

Attitude Constraints

Angle between Yaw and sun > 90 deg

Angle between Roll and Sun > 45deg

Angle between Roll and Velocity vector > 12deg

Angle between Roll and Albedo > 12 deg

Using AstroSat as a broad-band Observatory

So far we have discussed the details of individual payloads on AstroSat and its capabilities. However, since all these experiment are co-aligned (except SSM) and mostly operate in unison, AstroSat can effectively conduct broad-band multiwavelength observation from Optical to hard X-rays for select sources in the sky. Here we explore briefly the nature of such potential investigations.

For correlated variability in soft and hard X-rays use time tagged photons data from SXT and LAXPC.

- Correlated variability in X-ray and UV bands require time tagged data from X-ray instruments and fastest possible photometric data from UVIT.

- To study simultaneous broad-band X-ray spectrum from 0.3-150 keV, combine data from SXT, LAXPC and CZT and perform simultaneous spectral fits in XSPEC (X-ray analysis package).

- Search of Cyclotron absorption feature (usually in ~10 keV to 60 keV) needs well calibrated spectral data with high statistics from LAXPC and CZT instruments.

- For constructing multi-frequency spectra (Spectral Energy Distribution) of AGNs, CVs, SNRs etc, simultaneous observations with all 4 instruments over a time scale less than the variability time of a source is needed.

ASTROSAT Time sharing plan

Most of the AstroSat observations will be devoted to pointed mode studies of specific cosmic sources. These objects will be selected based on either proposals of the Instrument Teams (during the first 2 years) or the Principal Investigator proposals that have been selected by AstroSat Time Allocation Committee (ATAC). Proposed allocation of observing time of Astrosat during first 3 years of regular observation, to different instrument groups and open time to Indian and international scientists is given in table below.

Table: 8.1

Allocation of Observing Time on AstroSat.

Instruments	*PV Phase (6 months from launch)*	*Guaranteed Time (6 months after PV)*	*Second Year (after launch)*	*Third year (after launch)*	*Fourth year (after launch)*
X-ray Inst. Teams	67%	4 months	32.5%	20%	-
UVIT Team	33%	2 months	17.5%	10%	-
Indian Proposals	-	-	35%	45%	65%
International Proposals	-	-	-	10%	20%
Canadian Proposals	-	-	5%	5%	5%
LU (UK) Proposals	-	-	3%	3%	3%
Targets of Opportunity Proposals (ToO)	-	-	5%	5%	5%
Calibration time	-	-	2%	2%	2%

Observing Cycles

The following proposal cycles will be available for the AstroSat mission.

AO (Announcement of Opportunity) cycle

ISRO will periodically issue calls for proposals to the astronomy community. Each of these calls will be for a defined Announcement of Opportunity (AO) cycle. Submitted proposals will be reviewed by the AstroSat Time Allocation Committee (ATAC) and external referees.

ToO (Target of Opportunity) cycle

The ToO cycle will allow submission of proposals requiring the immediate observation of a sudden and unexpected astronomical event. The proposal in this cycle will be subjected to fast-track review process different from normal procedure for AO proposals. The ToO cycle will be open throughout the AstroSat mission life.

CAL (Calibration) cycle

In this cycle, only proposals aimed at calibration of the space craft / payloads and diagnosis of their health can be submitted by Payload Operation Centre (POC) team which includes the instrument PI. The proposals in this cycle would be subject to verification by the Calibration Scientist. This cycle will be open throughout the mission life.

Proposal Types

- Regular pointing proposals with or without time constraints – Consisting of one or more targets and single observation of each target.
- Monitoring proposals - Repeated observations of a single target
- Anticipated ToO proposals - Target of opportunity which is foreseen.

Proposal review process and time allocation

The submitted proposals in each cycle will be subjected to an evaluation process by the ATAC. If a cycle is set to have a two level hierarchy, then members of the ATAC may chair subcommittees. The ATAC chairperson is the final authority. (S)he is assisted in the evaluation process by the members of the ATAC or external experts, depending on the level of hierarchy (one or two). Note that only the AO cycle has the choice of operating in a single or a two level hierarchy. The following are the steps envisaged in the review process:

A) For a cycle having one level hierarchy:

1. ATAC chair will nominate external referees to review the proposals. Comments and ratings given by the referees are taken into account by the ATAC for the selection of proposals to which observation time is to be allotted.
2. ATAC Chair with other ATAC members collects the feedback from external referees and technical comments from the ATC and takes the final call on which of the proposals are to be allotted time. Each proposal in the final set of selected proposals is given A, B or C priority. (Normally, A is considered the highest priority and C the lowest.)

B) For a cycle having two level hierarchy:

1. ATAC Chairperson categorizes proposals submitted (say based on the science category they fall in) and distributes them to different Sub-TACs.
2. Sub-TAC chair will nominate external referees to review the proposals. (S)he along with other Sub-TAC members selects proposals from the lot allotted to them as candidates for allotting observing time. Comments and ratings given by the referees are taken into account by the Sub-TAC for this selection. Sub-TAC decides a rating and comments for each proposal.
3. ATAC Chair with other ATAC members collects the feedback from Sub-TACs as well as technical comments from the ATC and makes the final decision on which of the Sub-TAC suggested proposals are to be allotted time. Each proposal in the final set of selected proposals is given A, B or C priority.

   When the observations are scheduled for observations, `A' priority proposals are given preference followed by `B' priority proposals. If any `A' or `B' priority proposals cannot be scheduled in the ongoing cycle, they will be scheduled in the next cycle. `C' priority proposals which cannot be scheduled in the current cycle will be discarded.

Proposal submission for AstroSat observing time

Proposers/ guest observers will have to submit proposals to ISRO by the deadline given in the Indian Space Science Data Centre (ISSDC) website using AstroSat Proposal Processing System (APPS) software. APPS can be accessed through the AstroSat Support Cell (http://astrosat-ssc.iucaa.in) website or through http://www.issdc.gov.in. APPS is not downloadable and cannot be used off-line.

An APPS proposer's guide is made available at ASC and IUCAA websites which elaborates on the proposal submission procedure. *****

Acronyms

APPS - ASTROSAT Proposal Processing System
AGN -Active Galactic Nuclei
AOCS- Attitude and Orbit Control System
ACT – Active
BMU - Bus Management Unit
BOD - Bright Object Detected
BM - Bias Map
BB - Broad Band
CZTI – Cadmium Zinc Telluride Imager
CMOS – Complementary Metal Oxide Semiconductor
CFRP - Composite Fibre Reinforcement Plastic
CTI - Charge Transfer Inefficiency
CCD – Charge Coupled Device
Cal – Calibration
CPU – Camera Proximity Unit
CVs - Cataclysmic Variables
CSPAs - Charge Sensitive Preamplifiers
CPM - charge particle monitor
DIR - Deck Interface Ring
DHU - Data Handling Unit
EU - Electronics Unit
ES – Earth Shine
EM – Engineering Model
FWHM – Full Width at Half Maximum
FUV – Far Ultraviolet
FWMA – Filter-Wheel-Motor Assembly
FWDE – Filter- Wheel Drive Electronics
FS – Fail Safe
FPCA - Focal Plane Camera Assembly
FW - Fast Windowed photon counting
FPGA - Field Programmable Gate Array
FOVC - Field Of View Collimator
FOV - Field Of View
FEB - Front-end Electronics Board
GT - Guaranteed Time
GC - Geocoronal emission
HK - House Keeping
HVU - High Voltage Unit
LAXPC - Large Area X-ray Proportional Counters
LLD - Lower Level Discriminator
LEO - Low Earth Orbit
LBT - Low Bit-rate Telemetry
LP – Low Power
MM - Memory Management
MGKML – M.G.K Menon Laboratory

MCPs – Micro Channel Plates
NUV – Near Ultraviolet
OC – Over Current
PMT - Photo-multiplier tubes
PE - Processing Electronics
PA - Post Amplifiers
PV – Performance Verification
PSF – Point Spread Function
REA - Readout Electronic Assembly
SXT - Soft X-ray imaging Telescope
SSM - Scanning Sky Monitor
SB – Stand By
SEL - Single Event Latchup
SXT – Soft X-ray Telescope
SNRs - Supernova remnants
SAA - South Atlantic Anomaly
SSR - Solid State Recorder
TEC - Thermo-Electric Cooler
ULD - Upper Level Discriminator
UVIT - Ultra Violet Imaging Telescope
VIS – Visible
WSC - Window Support Collimator
ZL – Zodiacal Light